INAUGURAL – DISSERTATION
zur
Erlangung der Doktorwürde
der
Naturwissenschaftlich-Mathematischen
Gesamtfakultät
der
Ruprecht-Karls-Universität
Heidelberg

Vorgelegt von
Master of Chemical Science Vitaliy Yurkiv
aus: Dolyna, Ukraine

Tag der mündlichen Prüfung: 17.12.2010

Modeling and experimental validation of CO heterogeneous chemistry and electrochemistry in solid oxide fuel cells

Gutachter: apl. Prof. Dr. Hans-Robert Volpp, PCI, Heidelberg

Priv.-Doz. Dr. Wolfgang G. Bessler, DLR, Stuttgart

Zusammenfassung

In der vorliegenden Arbeit wurden experimentelle und numerische Untersuchungen zur heterogen katalysierten und elektrochemischen Oxidation von CO an Anodensystemen (bestehend aus Nickel und yttriumdotiertem Zirkoniumdioxid, YSZ) von Festoxidbrennstoffzellen (engl. Solid Oxide Fuel Cells, SOFCs) ausgeführt, um den mikroskopischen Mechanismus der an der CO/CO_2–Gasphase/Ni-Elektrode/YSZ-Elektrolyt-Dreiphasen-Grenzfläche ablaufenden Ladungsübertragungsreaktion aufzuklären. Temperatur-programmierte Desorptionsmessungen (TPD) und Temperaturprogrammierte Reaktionsmessungen (TPR) sowie Dichtefunktionaltheorierechnungen wurden ausgeführt, um adsorptions-, desorptions- und reaktionskinetische sowie thermodynamische Daten für die CO/CO_2/Ni- und CO/CO_2/YSZ-Reaktionssysteme zu erhalten. Unter Verwendung dieser Daten wurden auf Elementarreaktionen basierende mikrokinetische Modelle, die vier verschiedene Ladungstransfermechanismen enthielten, für die elektrochemische CO-Oxidation entwickelt und zur numerischen Simulation experimenteller elektrochemischer Literaturdaten wie Polarisationskurven und Impedanzspektren herangezogen. Durch Vergleich zwischen Simulation und Experiment konnte gezeigt werden, dass nur einer der vier Ladungstransfermechanismen die vorhandenen elektrochemischen Daten über einen weiten Temperatur- und CO/CO_2–Gaszusammensetzungsbereich konsistent reproduzieren kann.

Abstract

In the present work experimental and numerical modeling studies of the heterogeneously catalyzed and electrochemical oxidation of CO at Nickel/yttria-stabilized zirconia (YSZ) solid oxide fuel cell (SOFC) anode systems were performed to evaluate elementary charge-transfer reaction mechanisms taking place at the three-phase boundary of CO/CO_2 gas-phase, Ni electrode, and YSZ electrolyte. Temperature-programmed desorption and reaction experiments along with density functional theory calculations were performed to determine adsorption/desorption and surface diffusion kinetics as well as thermodynamic data for the CO/CO_2/Ni and CO/CO_2/YSZ systems. Based on these data elementary reaction based models with four different charge transfer mechanisms for the electrochemical CO oxidation were developed and applied in numerical simulations of literature experimental electrochemical data such as polarization curves and impedance spectra. Comparison between simulation and experiment demonstrated that only one of the four charge transfer mechanisms can consistently reproduce the electrochemical data over a wide range of operating temperatures and CO/CO_2 gas compositions.

Acknowledgements

There are many people who deserve credit and thanks for their part in this thesis. Without their contributions and support, this work would not have been possible.

I wish to express my sincere gratitude to all my research advisors. First and foremost, I am most thankful to Priv.-Doz. Dr. Wolfgang Bessler for being an outstanding supervisor and mentor. Prof. Dr. Hans-Robert Volpp, my supervisor at PCI, for his indulgence and staying in the institute to the late night helping me in my work.

I would like to thank the International Graduate College (IGK 710) “Complex Processes: Modeling, Simulation and Optimization” at the University of Heidelberg for fellowships.

I have had the great pleasure of working with many talented and friendly people Marcel Vogler, Dzmitry Starukhin, Alexandr Gorski, Christian Hellwig, Nicolas Bayer-Botero, Stefan Gewies whose support and faithful discussion played irreplaceable role in my work. The individual thanks are due to Dr. Marcel Vogler who has been a tremendous help in working with calculation programs, Dzimitry Starukhin who has helped me with technical problems and made all the tools available to me that I needed to fix or construct equipments in lab, Dr. Alexandr Gorski for his extreme help with DFT calculations.

I would like to thank my parents, Volodymyr and Galyna who have inspired me throughout my entire life to work hard, invest in myself through education, and to strive to be a good person.

Finally, I would like to thank my wife, Viktoriya for her unending love, encouragement, and understanding.

Table of Contents

Acknowledgements i
List of Symbols ii

1. Introduction and Background 1

1.1 Motivation 1

1.2 Background 1

1.2.1 Fuel Cells 1

1.2.2 Types of Fuel Cells 2

1.2.3 Fuel for Fuel Cells 4

1.3 Solid Oxide Fuel Cells 5

1.3.1 SOFC electrolyte 7

1.3.2 SOFC anode material 9

1.3.3 SOFC cathode material 9

1.4 Literature Overview of CO Oxidation at SOFC Anodes 9

2. Quantum Chemical Calculations 13

2.1 Schrödinger Equation and the Born-Oppenheimer Approximation 13

2.2 Density Functional Theory 14

2.3 Pseudopotentials 16

3. Experimental Setup, Sample Preparation and Characterizations 18

3.1 Experimental apparatus 18

3.2 Sample preparation 20

3.3 Characterization of the samples 22

3.3.1 Auger Electron Spectroscopy 22

3.3.2 Low Energy Electron Diffraction Spectroscopy 22

3.3.3 Sum Frequency Generation Spectroscopy 23

3.4 TPD/TPR spectroscopy 24

3.4.1 The Basic Principles of TPD/TPR Technique 24
3.4.2 The Analysis of TPD/TPR Spectra 25
4. Electrochemical Modeling and Simulation 28
4.1 Electrochemistry 28
4.2 Elementary Kinetics 30
4.2.1 Gas Phase Chemistry 31
4.2.2 Surface Chemistry 31
4.2.3 Charge Transfer 32
4.2.4 Charge transfer of oxygen anion in Ni/YSZ model anode 34
4.3 Modeling and Simulations of Ni/YSZ Model Anodes 36
4.3.1 SOFC Model Anodes 37
4.3.2 Surface Diffusion 38
4.3.3 Reaction Mechanism 38
4.4 Numerical simulations 40
5. Results of DFT Calculation on YSZ Surface 42
5.1 Computational details 42
5.2 DFT calculation of CO oxidation over YSZ 44
5.3 DFT calculation of H_2 oxidation over YSZ 47
5.4 Conclusions 49
6. Results of Experimental and Simulated TPD/TPR Spectra 50
6.1 Methodology of TPD/TPR simulation 50
6.2 TPD/TPR on Ni(111) sample 51
6.2.1 CO adsorbate structure on Ni(111) surface. 51
6.2.2 Experimental and simulated CO TPD/TPR spectra on Ni(111) surface. 53
6.2.3 CO oxidation on Ni(111) surface. 54
6.3 TPD/TPR on YSZ sample 55
6.3.1 TPD/TPR investigation of CO adsorption/desorption and oxidation on YSZ surface. 55

6.3.2 TPD/TPR investigation of H_2O interaction with YSZ. 56
6.4 Conclusions 63
7. Results of Electrochemical Simulations 64
7.1 Ni, CO-CO_2|YSZ point anode 64
7.1.1 Simulation targets for model validation 64
7.1.2 Elementary kinetic reaction mechanism 65
7.2 Ni, CO-CO_2|YSZ pattern anode 74
7.3 Recommendations for further studies 84
7.4 Conclusions 84
8. Summary 85
Appendix 87
A brief introduction to Kröger-Vink Defect Notation 87
List of Publications 88
Bibliography 89

List of Symbols

Symbol	Unit	Meaning
A^{cell}	m^2	Cell surface area
A_σ	K/Ω·m	Pre-exponential factor of ionic conductivity
a_i		Activity of species *i*
a_0^{elyt}	K/(Ω·m·$Pa^{1/4}$)	Pre-exponential factor of electrolyte electronic conductivity
b_0^{elyt}	1/K	Temperature coefficient of electrolyte electronic conductivity
c_i	mol/cm^2	Surface concentration of species *i*
d	m	Pattern width
D_i	m^2/s	Diffusion coefficient of species *i*
d_{elyt}	m	Thickness of the electrolyte layer
$E_{\text{f,r}}^{\text{act}}$	J/mol	Activation energy of chemical reaction (f – forward, r – reverse)
E	V	Cell voltage
E_σ	J/mol	Activation energy for ionic conductivity
F	C/mol	Faraday's constant
$\Delta_R G_m$	J/mol	Gibbs free energy of reaction
h_i	J/mol	Molar enthalpy of species *i*
$\Delta_R H_m$	J/mol	Enthalpy of reaction
h_{Ni}	m	Height of Ni pattern
i_0	A/m^2	Exchange current density
i_F^A	A/m^2	Area specific Faradaic current density
J_i^{diff}	mol/(m^2·s)	Molar diffusion flux of species *i*
k_{ct}^0	mol/(m·s)	Pre-exponential factor of charge transfer reaction

k^0	mol/(m^n·s)	Pre-exponential factor of chemical reaction (n depends on reaction)
$l_{\mathrm{TPB}}^{\mathrm{A}}$	m/m^2	Area-specific three phase boundary length
M_i	kg/mol	Molar mass of species *i*
P_{cell}	W/m^2	Power density
p	Pa	Pressure
p_i	Pa	Partial pressure of species *i*
R	J/(mol·K)	Ideal gas constant
R	Ω	Resistance
R_{pol}	Ω·cm^2	Polarisation resistance
$\Delta_{\mathrm{R}}S_{\mathrm{m}}$	J/(mol·K)	Entropy of reaction
$\dot{s}_{\mathrm{i}}^{\mathrm{A}}$	mol/(m^2·s)	Surface area specific production rate
$\dot{s}_{\mathrm{i}}^{\mathrm{V}}$	mol/(m^3·s)	Gas phase volume specific production rate
T	K	Temperature
t	s	Time
X_i		Mole fraction of species *i*
Y_i		Mass fraction of species *i*
y	m	Spatial position perpendicular to cell surface
z	m	Spatial position parallel to surface
z		Number of electrons in charge transfer reaction
α		Charge transfer coefficient
β		Symmetry factor
η	V	Overpotential
θ_i		Surface coverage
ν_i		Stoichiometric factor of species *i*

σ_i		Surface sites occupied by species *i*
σ_{elyt}	1/(Ω·m)	Ionic conductivity of electrolyte
ϕ	V	Electric potential
$\Delta\phi$	V	Potential difference between phases
$V_{O,YSZ}^{\bullet\bullet}$		Oxygen vacancy in YSZ lattice
□		Free surface site
$O_{O,YSZ}^{X}$		Oxygen in the YSZ lattice

1. Introduction and Background

1.1 Motivation

Solid oxide fuel cells (SOFC) are a promising alternative energy source, because of their wide application potential ranging from mobile technology to stationary power plants, due to their high energy efficiency and their low pollutant emission. However, the microscopic details of the electrochemical reaction mechanism, occurring at the three-phase boundary of gas-phase, electrode, and electrolyte, are not yet fully resolved even for simple systems such as the electrochemical carbon monoxide (CO) oxidation reactions.

This thesis is focused on experimental and numerical modeling studies of CO heterogeneous chemical and electrochemical oxidation at Ni/YSZ SOFC anode systems. Experimental temperature-programmed desorption (TPD) and reaction (TPR) investigations along with density functional theory (DFT) calculations were performed in order to determine adsorption/desorption and surface diffusion kinetics data as well as reliable thermodynamic parameters for the $CO/CO_2/Ni$ and $CO/CO_2/YSZ$ systems. The kinetic and thermodynamic data of heterogeneous surface adsorption/desorption and reaction processes as well as the surface diffusion data were included into elementary kinetic models of the electrochemical CO oxidation at Ni/YSZ SOFC anodes. In order to shed more light on the actual anodic charge transfer (CT) kinetics, different CT reaction mechanisms, were employed. In particular, different charge-transfer reactions of oxygen ions at the three-phase boundary were spillover pathways and pathways were the discharged oxygen atom remains on the YSZ surface.

1.2 Background

1.2.1 Fuel Cells

The fuel cell is an electrochemical device that converts the chemical energy of reaction directly and continuously into electricity. Fuels, such as carbon monoxide, hydrogen etc., come into contact with electrode and electrolyte where they are oxidized, and released electrons go to the outside circuit. In XXI century, fuel cells are becoming more affordable and practical; they are considered higher quality than the internal combustion engine and electric generator. A fuel cell system potentially offers the advantage of incorporating several balance-of-plant functions in the cell and stack. In addition, fuel cells can be stable against transient conditions occurring in real systems. Therefore, simplicity, lower investment and operating costs, which are relevant for target applications of fuel cells in both stationary power as well as mobile power, are successfully combined. The principle of fuel cells has existed over a hundred years and during this time it played an important role in energy conversion processes. Nowadays, when

technology moves forward tremendously, fuel cells have, due to their high efficiency and low pollutant emission, an irreplaceable role.

There are five features which make fuel cells unique in the energy conversion processes: *high efficiency, reliability, low emission, low noise and fuel flexibility*.

High Efficiency – since fuel cells convert the fuel to energy in one stage without the need for multiple steps, they achieve much higher conversion efficiencies. For example, SOFCs have electrical efficiencies up to 60% and MCFC can achieve combined electrical and thermal efficiencies of about 90% when used for CHP.

Reliability – the parts of fuel cells are mainly stationary the only moving parts are secondary devices (pumps, blowers, compressors). In comparison with internal combustion engines, there are considerably less moving parts that therefore require less maintenance.

Low Emissions – the main fuels for fuel cells are hydrogen, carbon monoxide, methane and they all give mainly water and carbon dioxide as the products. It means that the products of fuel cells operation are safe because there is no combustion and no particulate emissions.

Very Low Noise and Vibrations – as was mentioned above the only movable parts of fuel cells are compressor, blower and pump that make practically neglecting noise. This also means that the fuel cell does not vibrate at any noticeable rate (an order of magnitude less than a combustion engine).

Fuel Flexibility – fuel cells can operate using practically all types of fuels such as hydrogen, carbon monoxide, hydrocarbons etc. This is one of the main advantages of fuel cells which give the possibility of their application everywhere from home usage to big factory and in space craft.

1.2.2 Types of Fuel Cells

Different branches of industry and science may use various types of fuel cells as their need requires. To solve this problem many types of fuel cells have been developed. Generally, fuel cells are distinguished by the electrolyte that causes difference in operating temperature and applications. In Table 1.1, the overview of fuel cell types is described.

Table 1.1: Types of fuel cells

Fuel cell type	Operating temperature [K]	Electrolyte material	Fuel and mobile ion	Electric efficiency	Typical applications
Alkaline (AFC)	353	Potassium hydroxide	H_2, OH^-	60 % (Pure H_2)	Space (transport)
Proton exchange membrane (PEMFC)	313-353	Conducting polymer	H_2, H^+	45 %	Transport and CHP[1]
Direct Methanol	353	Conducting	Methanol, H^+	50 %	Mobile

(DMFC)		polymer			Phones and laptop PC's
Phosphoric acid (PAFC)	473	Phosphoric acid	H_2, H^+	45 %	CHP[1]
Molten carbonate (MCFC)	923	Molten carbonate	H_2, CO, CO_3^{2-}	50 %	CHP[1]
Solid oxide (SOFC)	1000-1200	Solid oxide	H_2, CO, CH_4, O^{2-}	60 %	CHP[1]

[1] Combined Heat and Power production

Alkaline FC was used in Appollo and Shuttle Orbiter crafts. The main problems are that in this type of fuel cell air and fuel supplies must be free from CO_2 and extremely pure oxygen and hydrogen must be used. Highly porous electrodes have to be used to omit a problem with slow reaction rate. *Proton Exchange Membrane FC*. As alkaline FC, PEMFC was used on first spacecraft. Using a solid and immobile electrolyte, this type of fuel cell is very simple and works at quite low temperatures. However, there is a big problem with impurities, consequently quite pure hydrogen must be used. *Direct Methanol FC*. In DMFC, the problem with hydrogen was solved by using methanol as a fuel instead. Using a liquid methanol, DMFC's have very low power; however, they were be used in portable electronic equipment. *Phosphoric Acid Fuel Cells*. Phosphoric acid fuel cells have been field tested as early as the 1970s. These systems operate at temperatures between 400 K and 500 K. The principal use of these systems has been for mid-sized (200 kW) stationary power generation applications. The problem of fuelling with hydrogen was resolved by reforming methane but it led to increase of the cost, complexity and size. *Molten Carbonate Fuel Cells*. Molten carbonate fuel cells operate at high temperatures (~900 K) that allow them to use fuel directly with a simplified fuel processor. It needs the carbon dioxide in the air to work and they require significant time to reach operating temperature. However, they are very good with keeping power constant in large utility applications. *Solid Oxide Fuel Cells*. Despite a high operating temperature, SOFC have a lot of advantages. They use cheap catalysts and gases such as natural gas, hydrogen and carbon monoxide without additional cleaning. In addition, the heat produced during their operation can be further reused. All the advantages listed above in combination with their simple design make SOFC suitable for large to very large stationary power applications.

The first global application of fuel cells was in the middle of XX century during the outer space exploration. The great outcome from that time was used to implement the development of different applications of all fuel cells types. The found applications of fuel cells are in three global areas: transportation, stationary power and portable power. The overview of fuel cells application and their costs are given in Fig. 1.1.

Transportation. Low emission with high power is the main aim of engine in car production where fuel cells are the most furious competitor with internal combustion engine. First electric

modern fuel cells applications in mobile branch came from 60's of last century, when General Motors demonstrated the Electrovan, a drivable fuel cells vehicle. The Electrovan worked on liquid hydrogen and oxygen and had a range of 240 km and top speed of 110 km/h. Nowadays, automotive companies have a higher success, and their cars can operate up to few thousand kilometers. DaimlerChrysler, for example, uses the pure fuel cells driven concept without using buffer or backup batteries and it requires the highest control of the balance-of-plant (electronics, pump, compressors). Other companies combine fuel cells with electric power storage in batteries or supercapacitors.

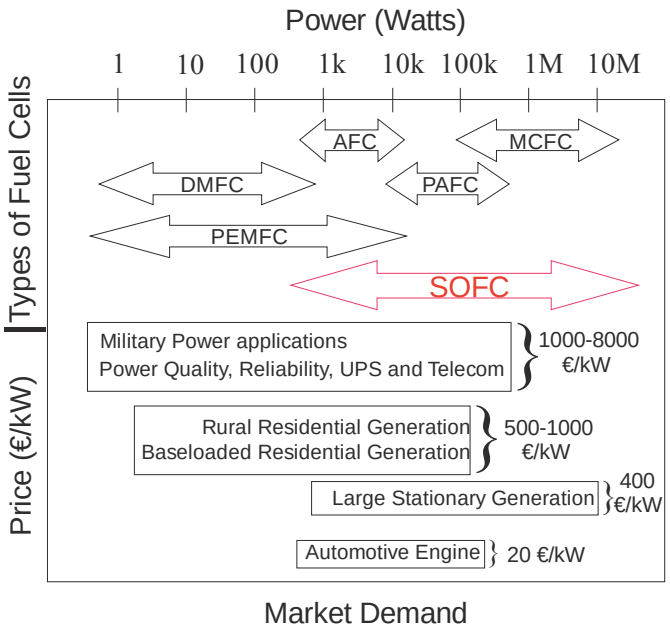

Figure 1.1: Types of fuel cells and their applications

Stationary power. Stationary power based on fuel cells becomes even more successful than automotive applications. The greatest usage was found to be the combination of heat and power generation (CHP). In fact, fuel cells are practical engines for micro CHP system in domestic environment (10-20 kW). In this area, significant results have been reached by UTC Power Company, where fuel cells have been installed worldwide with the power range from 400 kW to 2 MW.

Portable power. A portable fuel cell usually is used in camping, yachting and traffic monitoring and has minor application in comparison with transportation and stationary power plants. However, their usages are increased especially as ancillary supply in cars, so called auxiliary power units (APUs).

1.2.3 Fuel for Fuel Cells

There is no unique fuel for all types of fuel cells. If one kind of fuel is appropriate for certain fuel cells for others it is poisonous. Hydrogen, for example, is a good fuel for all fuel cells, but even the smallest amount of carbon monoxide can destroy PEMFC. Conversely, the presence of

carbon dioxide (CO_2) in fuel gas with the concentration up to 25% does not change the efficiency of PEMFC. Nonetheless, carbon monoxide in combination with hydrogen increases the efficiency of solid oxide fuel cells. Opposite situation occurs in AFCs, if the trace amount of CO_2 is present in fuel, it drastically influences the work of the system by forming a carbonate in the alkaline electrolyte. SOFC can run on hydrogen/carbon monoxide mixture (synthesis gas) which is produced via hydrocarbons steam reforming. Also this type of fuel cells can tolerate certain quantities of CO_2, and importantly, they accept hydrocarbons such as methane and propane. This fuel-flexibility makes SOFC suitable in use everywhere from home to industry.
There are certain compounds such as sulfides, halogens and silicon derivatives which are present in most fossil fuels which can significantly damage fuel cell performance. However, the temperature can "allow" using a small amount of such impurities, meaning that the requirements for pure fuel at high temperature fuel cells are not very high.

1.3 Solid Oxide Fuel Cells

The solid oxide fuel cells is a complete solid state device which usually consist of nickel anode, a non-stoichiometric compound such as doped $LaMnO_3$ as a cathode, and yttria-stabilized zirconia (YSZ) Y_2O_3:ZrO_2, as an electrolyte. One of the first studies on SOFCs was performed by Emil Baur and Hans Preis at ETH Zürich in 1937 [1]. Baur and Preis studied a number of ceramic materials as electrolytes, including porcelain and clay, and they observed the highest performance for zirconia- and ceria-based electrolytes. Nowadays, these materials are widely used in SOFC technology and they are one of the most successful electrodes. Schematic illustration of SOFC operation is shown in Fig 1.2. Fuels, such as carbon monoxide, come into contact with the electrodes. Air flows along the cathode where oxygen ionized, diffuses into the electrolyte and migrates to the other part of the cell where its encounter the anode. The oxygen ions meet the fuel at the anode/electrolyte interface and react catalytically, giving off carbon dioxide, heat, and most importantly electrons.

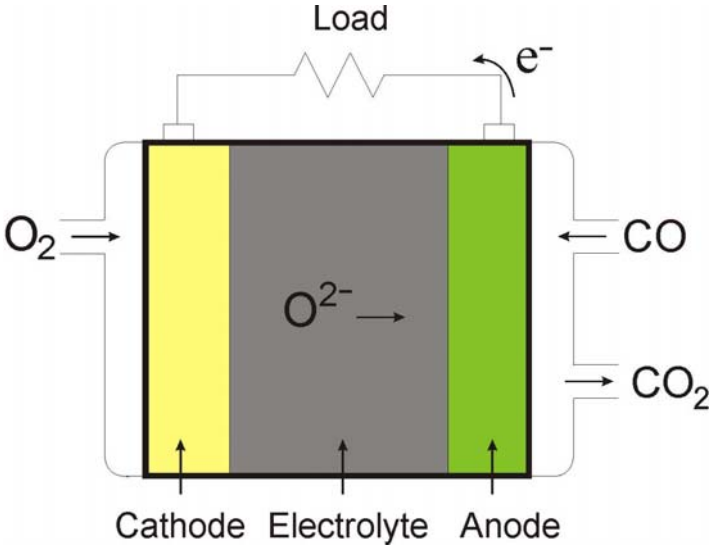

Figure 1.2: Schematic representation of fuel cell setup

Analysis of work performed by SOFC. One of the possible fuels for solid oxide fuel cells is carbon monoxide. Using the first law of thermodynamics by means of the steady flow energy equation and applying the second law in the form of maximum work, it is possible to determine the maximum work performed by fuel cell.
Carbon monoxide from the anode and oxygen from the cathode site are set in fuel cell where carbon dioxide is produced. Globally the following reaction takes place

$$CO + ½\ O_2 \rightarrow CO_2. \tag{1.1}$$

Molar flux (per mol CO) must be

$$n_{CO} = 1 \text{ mol}, n_{O_2} = 1/2 \text{ mol}, n_{CO_2} = 1 \text{ mol},$$

applying the steady flow energy equation energy balance can be expressed as

$$Q - W = h_{CO_2} - h_{CO} - 1/2\, h_{O_2}, \tag{1.2}$$

where Q and W are the heat transferred into cell and the work transferred out of the cell respectively; and h is the specific (molar) enthalpy of the reactants and products.
According to the second law and if the process is reversible ($W = W_{max}$)

$$Q = T(s_{CO_2} - s_{CO} - 1/2\, s_{O_2}), \tag{1.3}$$

where T is the temperature at which heat is transferred to the system and s is the specific (molar) entropy of the reactant and products. Combining equations (1.2) and (1.3) gives

$$W_{max} = (h_{CO} + 1/2\, h_{O_2} - h_{CO_2}) - T(s_{CO} + 1/2\, s_{O_2} - s_{CO_2}). \tag{1.4}$$

Since all gasses are not perfect, the maximum electrochemical work per mol CO is given by equation (1.5)

$$W_{max} = [h_{CO}(T) + 1/2\, h_{O_2}(T) - h_{CO_2}(T)] - T[s_{CO}(T, p_{CO}) + 1/2\, s_{O_2}(T, p_{O_2}) - s_{CO_2}(T, p_{CO_2})]. \tag{1.5}$$

This equation describes the maximum work output. Appling the equation for the change of entropy in ideal gas the expression for maximum work can be rewrite as

$$W_{max} = -\Delta G_T^0 + RT \ln\left[\left(\frac{p_{CO}}{p_{CO_2}}\right)\left(\frac{p_{O_2}}{p_0}\right)^{1/2}\right]. \tag{1.6}$$

From the last equation, the maximum work depends on temperature, partial pressure of reactants and products and total pressure.
SOFC science and technology has been discussed in detail in various textbooks. For example, the book "High-temperature Solid Oxide Fuel Cells: Fundamentals, Design and Applications" by Singhal and Kendall [2] provides comprehensive and practical information on specific types of fuel cell and their application. Another book by Minh and Takahashi [3] gives the overview about the parts of SOFC. Also, there are many review papers (Kee et al. [4-6], Minh [7], Ormerod [8]) which described different aspects of SOFC operation. The history of SOFCs has been reviewed by Möbius [9].

1.3.1 SOFC electrolyte

The electrolyte for solid oxide fuel cells must be a good oxygen ion conductor but poor electronic conductor. Also it must be stable from anode side for reducing and from the cathode side for oxidizing environments. As stated before, yttria-stabilized-zirconia is widely used as an electrolyte for SOFC. YSZ with the fluorite structure contains O^{2-} which conduction is provided by oxide vacancies and interstitial oxide ions. This material is also called the "Nernst mass" because it has already been identified by Walther Nernst as solid electrolyte [9].

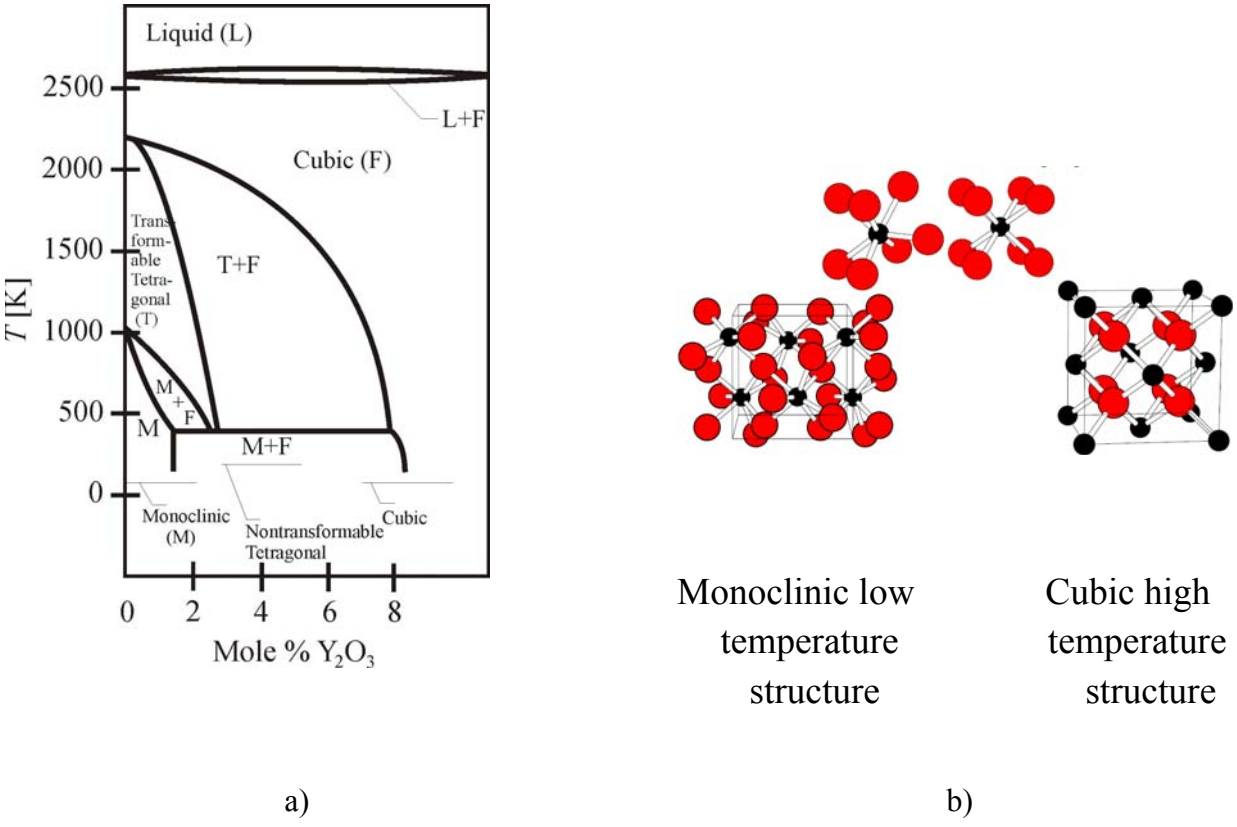

Figure 1.3: Phase diagram of partially stabilized zirconia
a) Phase diagram of partially stabilized zirconia, b) the most stable structures of ZrO_2

Yttria-stabilized-Zirconia is a mixture of ZrO_2 and Y_2O_3 which is present in the zirconia fluorite structure as the dopant. Also this structure is called tetragonal zirconia polycrystal. YSZ is a transformation-toughened material and can form different structures depending on amount of dopant (Y_2O_3) and temperature. The phase diagram of ZrO_2, which is doped by Y_2O_3, is shown in Fig. 1.3 a) and b) [10]. Also, on the right side of the figure, the most stable structures (monoclinic and cubic) are drawn. To form a fully stabilized structure, it is enough to add 8 mol% Y_2O_3 to ZrO_2 and this structure becomes cubic solid solution which has no phase transformation when heating up to 2500 K. The additional increase of dopant concentration does not lead to the increase of conductivity because at higher concentration the first and the second electron coordination shells of the dopant start interacting with the oxygen vacancies and the conductivity decreases. As mentioned before, oxygen anion conductivity provided by oxide vacancies, which are in balance with defects and can be represented in Kröger-Vink notation [11] as

$$YO_{1.5} \rightarrow Y'_{Zr} + 1/2\ V_O^{\bullet\bullet} + 3/2\ O_O^X, \tag{1.7}$$

and the reaction of the oxygen formation is

$$O_2 + 4\ Zr'_{Zr} + 2\ V_O^{\bullet\bullet} = 4\ Zr_{Zr}^X + 2\ O_O^X, \tag{1.8}$$

where Y'_{Zr} indicates yttrium on the zirconium site with the formal charge of -1, $V_O^{\bullet\bullet}$ is oxygen vacancy, O_O^X is normal oxygen on an oxygen site, Zr'_{Zr} is localized electron on a zirconium site. The O^{2-} conductivity according to Ref. [12] can be estimated by equation (1.9)

$$\sigma_{O^{2-}} = \frac{36000}{T}\exp\left(-\frac{83910}{RT}\right). \tag{1.9}$$

However, the space charge density of YSZ at the interface with electrode has more complicated behavior and depends on potential and temperature. The fraction of oxygen vacancies in the near-surface layer is described by the following equation [13]

$$x_V = \frac{x_V^{max}(T)x_V^{bulk}\exp(-z_V e\varphi / k_B T)}{x_V^{max}(T) + x_V^{bulk}(\exp(-z_V e\varphi / k_B T) - 1)}, \tag{1.10}$$

where x_V is the oxygen vacancy fraction in the oxygen sub-lattice, x_V^{max} maximum possible value of oxygen vacancy fraction, x_V^{bulk} concentration of oxygen vacancy in bulk electrolyte, z_V the formal charge of an oxygen vacancy, k_B the Boltzmann constant.

Also, except YSZ many other different compounds have been tried as an electrolyte in SOFC, such as doped ceria which has the same cubic fluorite crystal structure as YSZ. However, its

conductivity of 0.1 S/cm at 1200 K is too low for wide use in SOFC. The Bismuth oxides mixture has also appropriate structures and same characteristics like YSZ. However, significant electronic conductivity and high cost make it not suitable to practical use as an electrolyte in SOFC.

1.3.2 SOFC anode material

The anode of SOFC is a porous composite structure, consisting of an ionic conductor (the electrolyte material such as doped zirconia or ceria) and an electronic conductor (typically a metal such as nickel). The traditional materials system is nickel/yttria-stabilized zirconia (Ni/YSZ), introduced by Westinghouse in 1970 [14]. This material is suitable due to its low cost, excellent electronic conductivity and ability to catalyze breaking of the carbon-oxygen and carbon-hydrogen bonds at high temperatures. The anode material has to be porous of about 30 % which is needed for transportation of fuel from gas phase to the triple phase boundary where reactions occur.

1.3.3 SOFC cathode material

Strontium-doped lanthanum manganate, $La_{1-x}Sr_xMnO_{3-\delta}$ (LSM), is a commonly used perovskite material for SOFC cathode. LSM is chemically stable under oxidizing conditions at high temperature as well as a good electronic conductor (80 S/cm at 1100 K [15]). Usually LSM is mixed with YSZ to provide appropriate O^{2-} conductivity due to a limitation of LSM bulk phase O^{2-} conductivity. Also, LSM mechanically has a similar coefficient of thermal expansion to YSZ and low levels of chemical reactivity with YSZ.

1.4 Literature Overview of CO Oxidation at SOFC Anodes

The first significant studies on CO oxidation in related research for Pt-based SOFC were performed in the 60's of the last century [16-19]. However, there was considerable disagreement among the available results, especially concerning involved reaction species and their influence on fuel cell performance. In 1971 Etsell et al. [20] summarized these studies and concluded that during the CO oxidation in porous Pt anodes either gaseous or adsorbed CO and gaseous CO_2 are involved in the electrochemical step of the reaction. Also, they showed that limiting current densities are directly proportional to oxygen pressure. It causes the appearance of marked transition overpotential at 900-1300 K which is opposite to H_2-H_2O mixture where overpotential is essentially absent. In their study, the transition factor is about 0.5 and exchange current density varies from 0.05 to 3 mA/cm^2 and strongly depends on temperature. Finally, they concluded that the maximum exchange current density is expected for a gas mixture containing about 50 % of CO. In addition, Etsell et al. give the explanation for the lower exchange current density in CO-CO_2 mixture than in H_2-H_2O mixture. This is because exchange current density is inversely proportional to the number of free surface sites and high activation energy hinders the CO electrochemical oxidation. Later on, Holtappels et al. [21] showed that rates of CO electrochemical oxidation on Ni/YSZ anode is also lower than rates of H_2 oxidation by about 3

times to an order of magnitude. In 1992, Mizusaki et al. [22] supplied the earlier study on CO oxidation on Pt-based anodes by measurements of polarization curves for wide temperature range from 900 to 1300 K and CO/CO_2 ratio between 1 to 0.0001. They showed that reaction rate is controlled by simple charge transfer step at the TPB and charge-transfer coefficient is 0.5.
In the opposite to CO oxidation on Pt-based anodes, the investigations on Ni/YSZ based SOFC anode are very limited and do not afford the origin and detail description of all elementary reactions step of CO oxidation. Eguchi et al. [23] have compared $CO\text{-}CO_2$ and $H_2\text{-}H_2O$ systems with application for solid oxide fuel cells. They concluded that anodic reaction on Ni is strongly affected by $p(O_2)$ but not on the type of fuel; and the reaction mechanism is similar in both atmospheres. The same conclusion was made by Mizusaki et al. [22]. It means that CO oxidation is limited by the activation of oxygen ion. Also, Eguchi et el. infered that polarization conductivity significantly deteriorates by $CO\text{-}CO_2$ mixture than $H_2\text{-}H_2O$. As mentioned before, Holtappels et al. [21] have proved the fact that rates of CO electrochemical oxidation is slower than the one for H_2. However, Holtappels et al. give more detailed description of CO electrochemical oxidation than in Ref. [23]. The difference in oxidation rates they connected with: a) disparity in gas phase mass transfer resistance of the fuels at 1023 K and b) distinction in both the mass transfer and charge transfer resistances at 1273 K. They studied the electrochemical oxidation of CO on Ni/YSZ cermet as a function of $p(CO)$ and $p(CO_2)$ at 1273 K. In order to avoid carbon formation, CO/CO_2 ratio was kept at less than 20 due to Bouduard reaction but higher than 2 to avert formation of NiO. However, certain coverage of NiO or carbon on pronounced sites on the electrode surface cannot be excluded. Also, Holtappels et al. observed, in opposite to H_2 oxidation, that CO reaction rate is strongly time dependent. The same conclusion was made by Aaberg et al. [24] who investigated the CO oxidation on Ni/YSZ cermet electrodes as a function of the ratio CO/CO_2 and overpotential. Aaberg et al. reported that CO oxidation is time dependent and has lower reaction rates compared to the hydrogen oxidation. The different reaction rates and the time dependence may suggest a fundamental difference in the reaction mechanisms for the hydrogen reaction and the carbon monoxide reaction on Ni/YSZ cermet electrodes.
Matsuzaki et al. [25] have performed the investigation of CO and H_2 oxidation on porous Ni/YSZ anodes with various combination of CO, CO_2, H_2 and H_2O mixture at different temperature. The conclusion of this study is not in good agreement with the one made by Holtappels et al. [21], because Matsuzaki et al. stated that the rate of CO oxidation is only about 2 times at 1023 K and about 3 times at 1273 K slower than for H_2. Due to significant diffusion resistance in the experiments by Matsuzaki et al. there is much indecision in interpretation of their fitting results. Other comprehensive studies of CO electrochemical oxidation on the Ni grid electrode was done by Boulenouar et al. [26]. They performed electrochemical impedance measurements at 1123 K at open circuit potential. In their study, the influences of CO and CO_2 partial pressures on the electrochemical oxidation of CO, when one of the partial pressures of two gaseous reactants is kept constant, was investigated. Boulenouar et al. showed that at high $p(CO_2)/p(CO)$ ratio the impedance diagram demonstrates at least two relaxation times but, when $p(CO_2)/p(CO)$ ratio become low, a simple impedance shape was observed. Also, they concluded that CO, O and CO_2 participate in the reaction mechanism where CO and O are adsorbed.

Boulenouar et al. were one of the first who determined the parameter dependencies of $p(CO)$, $p(CO_2)$ and temperature. In their case a coefficient of 0.5 for both $p(CO)$ and $p(CO_2)$ variation was observed.

Weber et al. [27] performed electrochemical oxidation for H_2, CO and methane in SOFCs with Ni/YSZ-cermet anodes. In this study, the dc technique and impedance spectroscopy were applied under realistic working conditions. They did not observe long term stability for pure CO and in short period of time carbon deposition and micro-structural changes were observed within the anode. Also, they reported that stable operation is possible as long as the oxygen potential within the anode layer is kept at a sufficient level and/or appropriate steam to carbon ratio is used.

In comparison to previous studies the most comprehensive studies were made by Lauvstad et al. [28, 29]. Lauvstad et al. performed electrochemical steady-state polarization and impedance measurements employing well-defined point-shaped Ni electrodes in contact with YSZ electrolyte exposed to various CO/CO_2 mixtures. In the first theoretical part Ref. [28], they presented three models for CO oxidation. In the model 1, gaseous CO reacts with adsorbed oxygen atom producing gaseous CO_2; in opposite to model 1 the second model predicts adsorbed CO which reacts with adsorbed oxygen atom to produce gaseous CO_2. The third model includes adsorbed CO_2 which is produced by association of adsorbed CO and O. In the second paper by Lauvstad et al. [29], they analyzed their impedance measurements and concluded that the second mechanism is the best to interpret experimental data. This conclusion was made based on low frequency inductive behavior of impedance. The fact that the loop is associated with NiO formation could not be accounted while inductive effects were observed at potentials well negative of the thermodynamic limit for NiO formation. Also, their explanation that the inductive behavior is not accompanied by an increased bulk resistance, meaning an insufficient supply/removal rates by adsorption/desorption processes at triple phase boundary, is not convincing.

The performance of Cu-CeO_2-YSZ and Ni-YSZ composite SOFC anodes with H_2, CO and syngas were investigated by Costa-Nunes et al. [30]. The first cell (Cu-CeO_2-YSZ based) showed similar performance when operating on H_2 and CO fuels, while cells with Ni-YSZ anodes exhibit substantially lower performance when operating on CO compared with H_2. The big difference in charge-transfer reaction during H_2 and CO electrochemical oxidation causes a thorough design of Ni-based anode in application to gases obtained from coal gasification or reformers.

A series of electrochemical measurements for H_2, CO and CO/H_2 mixtures on Ni/YSZ pattern anodes were made by Sukeshini et al. [31]. The experiments were done for Ni patterned line width of 10, 20, 50, 100 μm and temperature range from 1000 K to 1123 K. They showed that anode overpotential and polarization resistance greatly correlated with the original Ni pattern area for the various patterned geometries. It was noted that observed polarization resistance and activation overpotential is higher for CO than for H_2 but not for CO/H_2 mixtures which is down to 25 % of H_2. For dry CO oxidation, the authors observed that the slope of the cell potential vs. current density is not a strong function of temperature, but when overpotential increases to more than 400 mV, the effective polarization resistance for CO does become a function of cell temperature. However, post-test scanning electron microscopy imaging showed a significant

sintering of nickel particles causes an undefined TPB length that proved the importance of structural changes during the experiment.

Recently, Leonide et al. [32] presented the electrochemical oxidation of CO in anode supported SOFC single cells along with a zero dimensional stationary model. In their experiments, the cells were characterized by electrochemical impedance spectroscopy in a wide range of operating conditions (varying temperature and CO/CO_2 gaseous composition). The Butler-Volmer equation was applied to determine polarization losses, whereas the contribution from the gas diffusion was calculated from Fick's law. The partial pressure and temperature dependency of the cathodic and anodic exchange current density was determined by a fit of semi-empirical power law model equation. Also, the exponents for the H_2, H_2O, CO and CO_2 partial pressure dependency of the anodic exchange current density were determined independently of each other.

A comprehensive experimental investigation of CO electrochemical oxidation was made by Utz et al. [33]. The Ni/YSZ patterned anodes were characterized by electrochemical impedance spectroscopy with large parameters variation range, $p(CO)$, $p(CO_2)$ and temperature under avoidance of NiO and coke formation. Parallel nickel stripes with the width of 25 µm were fabricated on 8.5 mol% polycrystalline Y_2O_3-stabilited ZrO_2 substrate with corresponding triple phase boundary length of about 1 m. The stability of the Ni patterned anodes was controlled by pre- and post-test SEM analysis. For the first time, the degradation rate for the CO electrochemical oxidation was determined and reached a value of 0.18%/h. Also, parameter dependencies were determined for variation of CO and CO_2 pressure and temperature. It was found that the line specific resistance depends inversely on $p(CO_2)$ with exponential value changing from 0.61 to 0.79. The same observation was found for the dependency of line specific resistance on $p(CO)$ for CO pressure less than $2 \cdot 10^4$ Pa but direct proportionality for higher $p(CO)$ value. Based on these observations and the fact that activation energy of CO oxidation vary from 0.85 to 1.42 eV, they concluded a changing of reaction mechanism of CO oxidation.

2. Quantum Chemical Calculations

At the beginning of 20th century, scientists carried out experiments whose results could not be explained by classical physics. The explanation of particles behavior at very high speed (close to the speed of light), as well as in very small systems (atomistic level), was the ground problems for Newton's physics. Deviations for very fast systems can be explained and brought into a coherent picture by Einstein's theory of relativity [34] while deviations for very small systems can be accounted for by quantum theory developed by Planck [35]. Here, the moving laws acquire the probability character and the system is described by wave function depending on coordinates and time $\Psi(x, y, z, t)$. The square of the wave function $|\Psi|^2 = \Psi^*\Psi$ describes the probability distribution (probability density).

The discreteness of energy, the wave-particle dualism of matter and light, Heisenberg's uncertainty principle, spin of a particle and quantum tunneling were the crucial phenomena which classical physics failed to describe and where quantum mechanics succeeded.

Electronically excited atoms emit the spectrum of light which compose of individual discrete lines but are not distributed over the complete spectrum. The photons of discrete energies emitted correspond to discrete electronic transitions in the energetic atom, and hence, the electrons must be restricted to discrete energy levels. This phenomenon is called quantization of energy. Another effect explained by quantum mechanics is dualism of matter and light proposed by the French physicist Louis de Broglie in 1923. Based on this theory, it was explained wave-like behavior of light (diffraction, interference), as well as particle (photoelectric effect). Indeed, light can be described as matter, while the probability density of a light particle behaves wave-like and this is the reason why light is diffracted.

2.1 Schrödinger Equation and the Born-Oppenheimer Approximation

Since probability density of micro-particles behaves wave-like it needs a differential equation which describes it, such as a wave function. This equation was developed by Erwin Schrödinger in 20's last century [35]

$$i\hbar\frac{\partial}{\partial t}\psi(r,t) = -\frac{\hbar^2}{2m}\nabla^2\psi(r,t) + V(r,t)\psi(r,t) \equiv \hat{H}\psi(r,t) \tag{2.1}$$

The total energy of the system can be calculated by solving the energy eigenvalue equation. Hence, the energy of electron system can be determined by means of solving Schrödinger's equation. The simplification of equation 3.1 to a time-independent function by separation of variables, gives the possibility to obtain the solution relatively easy

$$-\frac{\hbar^2}{2m}\nabla^2\psi(r)+V(r)\psi(r)\equiv\hat{H}\psi(r)=E\psi(r)\,. \tag{2.2}$$

The exact solution of Schrödinger equation can only be obtained for very simple system, such as H atom. In order to find an approximate solution, different approaches to calculate the energy of a system of electrons were proposed. Born and Oppenheimer in 1927 introduced an approximation [36] which resolves the problem of calculating the energy of an interacting multi-electron system. Such a system has multiple degrees of freedom, and thus computations are much more complex. The Born-Oppenheimer approximation assumes that the electrons will adjust their position instantaneously to any nucleic movement, since nuclei are much heavier than electrons are.

2.2 Density Functional Theory

Density functional theory (DFT) is an approach for the description of ground state properties of metals, semiconductors, and insulators. DFT is not just another way to solve the Schrödinger equation, but it is a method of parametrizing empirical results. Density functional theory is a precise way of interacting problem approach, by mapping it exactly to make it easier to solve non interacting problem. The most positive feature of DFT is that there is no need to compute the many body wavefunction. Instead the energy is written in terms of the electron density [37]

$$E=E[\rho(r)]=\int \mathrm{d}r V_{\mathrm{ext}}(r)\rho(r)+F[\rho(r)]\,, \tag{2.3}$$

Where, the both right-handed terms are functional, and as a function gives a number from a variable, a functional gives a number from a function.

The central assumption in DFT, which shows that the ground state properties of a system are unique functionals of the ground state electron density, was proved by Hohenberg and Kohn in 1964 [38]. The description of an interacting system of fermions via its density and not via its many-body wave function is the main idea of DFT. For electrons in a solid, which obey the Pauli principle and repulse each other via the Coulomb potential, it means that the basic variable of the system depends only on three spatial coordinates *x*, *y*, and *z*. Hohenberg-Kohn theory consist of 2 theorems:

1) Every observable of a stationary quantum-mechanical system can be calculated exactly from the ground-state electron density, *i.e.*, all observables can be written as functional of the ground-state electron density. The actual position of the nuclei determines the external potential $\hat{V}_{\mathrm{ext}}$. Since the kinetic energy of the electrons $\hat{T}_{\mathrm{e}}$ as well as the electron-electron interaction $\hat{U}_{\mathrm{ee}}$ adjust to the external potential $\hat{V}_{\mathrm{ext}}$ originating from the nuclei, the external potential $\hat{V}_{\mathrm{ext}}$ is the only variable of the system

$$\hat{H}_{\mathrm{el}}=\hat{T}_{\mathrm{e}}+\hat{V}_{\mathrm{ext}}+\hat{U}_{\mathrm{ee}}\,, \tag{2.4}$$

The ground-state electron density $\rho(r)$ determines the number of electrons N according to the conservation relation

$$N=\int \rho(r)\mathrm{dr}\,. \tag{2.5}$$

Hohenberg and Kohn, based their findings on the 1st theorem, proved that electron density contains the same information as the wave function Ψ that describes the electronic system.
2) The ground-state electron density can be calculated exactly using the variational method for minimization of the Hohenberg-Kohn functional (2nd Hohenberg-Kohn theorem). In this theorem, the variation method is applied to determine the electron density $\rho(r)\geq 0$ which is the subject of conservation equation 2.4 and the trial energy $E[\rho(r)]$ has to be equal to real ground state energy E_0.
These were the first theoretical footings of DFT calculations and they are known as Hohenberg-Kohn theorems. Other framework, in which intractable many-body problem of interacting electrons is reduced to a tractable problem of non-interacting electrons moving in an effective potential, is known as Kohn-Sham DFT [39]. In this theory, the effective potential includes the external potential and the Coulomb interactions between electrons are taken into account. They rewrite the total energy functional in the following way

$$E[\rho]=T_{\mathrm{e}}[\rho]+\int\left[V_{\mathrm{ext}}[r]+U_{\mathrm{el}}[r]\right]\rho(r)dr+E_{\mathrm{xc}}[\rho]\,, \tag{2.6}$$

where $T_{\mathrm{e}}[\rho]$ denotes the kinetic energy of the electrons without electron-electron interaction, U_{el} describes the Coulomb interaction between the electrons and V_{ext} takes into account the potential from the nuclei. The last term $E_{\mathrm{xc}}[\rho]$ includes all other energy contributions that have not been taken into account by the previous terms. However, the modeling of exchange and correlation interactions is very difficult within the Kohn-Sham method. In order to solve this problem, the local-density approximation (LDA) was introduce by Kohn and Sham along with their equations. The LDA states that the exchange-correlation energy can be given by assuming for each infinitesimal element of density, the energy is that of a uniform electron gas of density. In LDA the exchange correlation functional is based on the exchange correlation energy $\varepsilon_{\mathrm{xc}}(\rho(r))$ of a homogeneous electron gas with the electron density $\rho(r)$ and the functional is described as

$$E_{\mathrm{xc}}^{\mathrm{LDA}}[\rho(r)]=\int \varepsilon_{\mathrm{xc}}(\rho(r))\rho(r)\mathrm{dr}\,, \tag{2.7}$$

in which the exchange correlation energy solely depends on the local electron density [40]. Despite a great success of LDA, this theory is not satisfying all the details of charge distribution, because charge density is highly non-uniform around atoms. This problem was solved by introducing the generalized-gradient approximation (GGA) [41] where the spatial variation in the

density is taken into account. The GGA significantly improved predicted binding and dissociation energies and here the functional depends on the local electron density as well as on its first derivative

$$E_{\mathrm{xc}}^{\mathrm{GGA}}[\rho(r)] = \int f(\rho(r), \nabla\rho(r))\mathrm{d}^3\mathrm{r}\,, \tag{2.8}$$

Despite of the big achievement of GGA, it is still far from ideal and finding the accurate and commonly applicable exchange correlation energy remains the great challenge in DFT [42].
In this work, DFT is applied as implemented in the Cambridge Sequential Total Energy Package (CASTEP) developed by group of Mike Payne [37]. In CASTEP, the structures to be calculated are based on a supercell approach and where they have to be periodic in 3 dimensions. This approach essentially has a big advantage, because, upon expansion from a small metal cluster into three dimensions, a real solid surface is built. Here, a very important role plays an additional factor called symmetry of periodicity, since systems that are periodic in 3 dimensions have this additional symmetry. This means that the charge density must be constant under translation by the lattice vector *G* in reciprocal space according to

$$|\psi(r)|^2 = |\psi(r+G)|^2\,. \tag{2.9}$$

This is the basis for Bloch's theorem which can be formulated as electronic wave function in every three dimensional periodic system can be written as a product of a part representing the periodicity *u,* as well as a plane wave function $e^{ik\cdot r}$, with a wave vector *k*

$$\psi_{\mathrm{i}}(r) = u_{\mathrm{i}}(r)e^{ik\cdot r}\,. \tag{2.10}$$

Bloch's theorem reduces the problem of calculating an infinite number of plane waves to calculating a finite number of plane waves but still over the complete Brillouin zone characterized by the wave vector *k*.

2.3 Pseudopotentials

Millions of plane waves would be required to represent the electronic wavefunctions accurately. A combination of pseudopotentials and fast-Fourier transforms (FFT) are used to overcome this problem. FFT gives an efficient means of transforming the wavefunctions and charge density between real and reciprocal space. The advantage to this is that parts of the calculation scale differently in the two spaces, and therefore they are done in the 'cheaper' space. The concept of pseudopotentials is crucial for plane-wave total energy methods since the alternative full Coulomb potential of the electron-ion interaction decays too slowly to be accurately represented by a small number of Fourier components. The pseudopotential is a fictional potential that is constructed from the nucleus and the core electrons. The nuclear potential is singular and the

electron potential energy decreases proportionally to the atomic radius. Due to the high nuclear potential in the centre of the atom, the curvatures of electrons in this region are large. The strongly curved wave functions require a large plane wave basis sets; therefore, the representation of electrons in core-close regions is gordian. Moreover, since chemical effects are considered here, only valence electrons are important. Hence, a sustainable simplification for these systems is to replace the core potential as well as the electronic potential of the tightly bound electrons with a softer and finite pseudopotential. The resulting combination of the core and the electronic wavefunctions of the core electrons give pseudopotentials and are, therefore, softer and spatially finite. This potential, of course, changes the behavior of the wavefunction, but this effect can be met by matching the newly generated Coulomb potential to the old Coulomb potential beyond a certain pseudopotential radius.

3. Experimental Setup, Sample Preparation and Characterizations

In this chapter, the basic principles of the experimental procedure used in the present work are described. The experimental apparatus, which consist of by Auger electron spectroscopy, low energy electron diffraction, sum frequency generation and temperature programmed desorption and reaction, is described firstly (3.1). The details of sample preparation are specified in the second section (3.2). In the third subchapter, the overview of the methods, used to characterize the sample, are given (3.3). Finally, temperature programmed desorption and reaction technique, which was used to obtained kinetic and thermodynamic data, are described in detail in the last subchapter (3.4).

3.1 Experimental apparatus

The scheme of the experimental apparatus used in this work is illustrated in Fig. 3.1. The experimental apparatus was well described previously in our group [43, 44] and here only an overview is given.

The experimental apparatus consists of three parts: vacuum generation system, ultrahigh vacuum chamber (UHV) and sum frequency generation (SFG) spectrometer. The UHV chamber is depicted on the right-hand site of Fig. 3.1 and consists of the following parts: a) quadruple mass spectrometer, used for temperature programmed desorption and reaction (TPD/TPR) measurements, b) Auger electron (AES) and low energy electron diffraction (LEED) spectrometer, c) the feed and gas handling system, d) an ion gun, used for cleaning the surface of the sample by bombardment ("sputtering"). The principle of SFG technique is depicted on the left in Fig. 3.1.

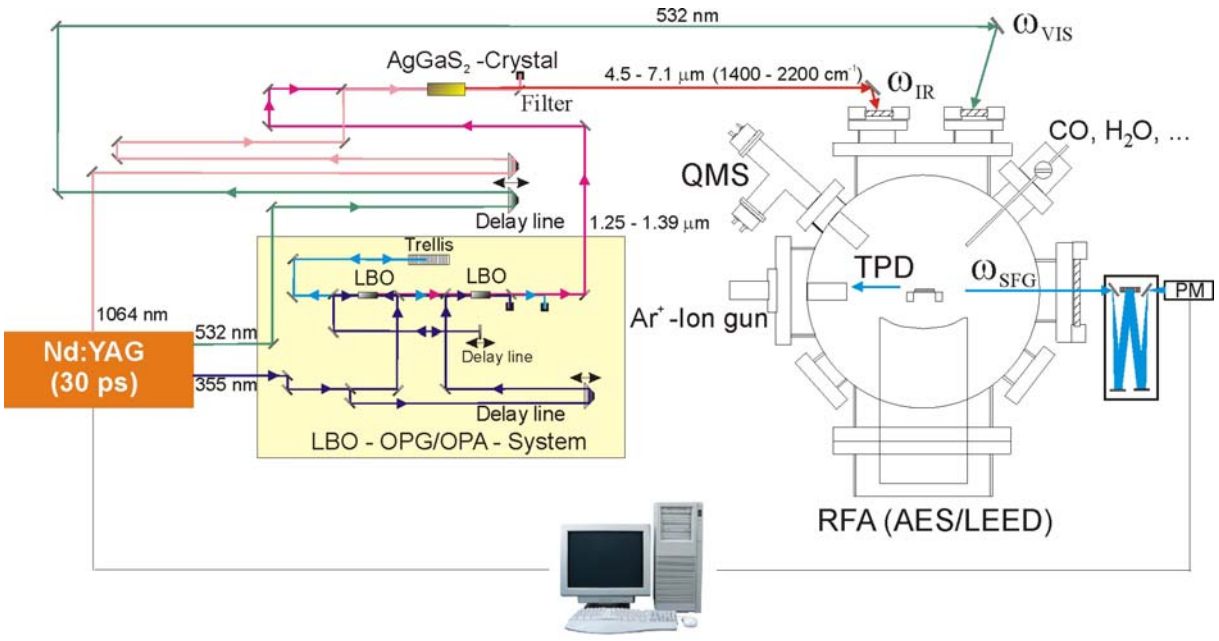

Figure 3.1: Experimental apparatus used in this study.
Nd:YAG – neodymium-doped yttrium aluminium laser,
LBO – Lithium Triborate (LiB_3O_5),
OPG/OPA – optical parametric generator/amplifier,
QMS – quadruple mass spectrometer,
TPD – temperature programmed desorption,
SFG – sum frequency generation,
RFA – retarding field analyser,

Vacuum generation system. A pressure of about 0.001 mbar is obtained by using rotary oil pump; to achieve a high vacuum a turbomolecular pump is used. A turbomolecular pump works at very high speed (about 50000 rotations/min) and consists of a cylindrical case with stator blades and rotor blades. In the ultra-high and high vacuum ranges (up to approximately 0.001 mbar), the pressure is measured by means of a Bayard-Alpert ionization gauge. If pressures are exceeding 0.001 mbar, the other types of pressure gauges must be used: most of these are based on the measurement of the resistance of a thin wire (Pirani gauges), which depends on the heat conductivity of the medium in its environment. Argon is used to stop a turbomolecular pump.
Quadrupole mass spectrometer. The QMS consists of three components, a) the ion source with electron impact ionizer and ion extraction optics, b) quadrupole analyzer, consisting of four cylindrical rods, and c) the ion detector (electron multiplier). Free electrons are formed by thermal emission from an electrically heated tungsten filament. The emitted electrons are accelerated by a potential difference of 70 V and the ionization takes place in the area between grid and aperture which are at approximately equal potential. The ions are detected via detection of their charges; that means the ions hit a metallic collector cone (Faraday cup) and the charge transfer is recorded using an electrometer preamplifier.
AES and LEED spectrometer. An Auger system includes a) an electron source and optical column, to create the incident electron probe for specimen excitation, b) an electron energy

analyzer and detector, for measurements and collection of emitted electron. The electron source is a LaB_6 cathode, which provides a total electron current up to 10 μA, and the electron energy analyzer is a Cylindrical Mirror Analyzer (CMA). The electron column is mounted coaxially within the CMA, which minimizes shadowing of the energy analyzer for a rough surface. The electron detector is a channeltron electron multiplier.

The feed and gas handling system. High quality (99.999%) gases were used for all the experiments. The gas flow rates were controlled by Brooks series mass flow controllers.

Sum frequency generation. A 40 ps mode-locked Nd:YAG-Laser for the optical IR-VIS SFG measurements was used. As the visible input frequency for the SFG process, a part of Nd:YAG-Laser was doubled by frequency to a wavelength of 532 nm. In order to generate IR radiation tunable in the frequency range of 1400-2200 cm^{-1} with pulse duration of 25 ps, the other part was used.

3.2 Sample preparation

In this work, the ion gun and thermal desorption vacuum cleaning methods were used to prepare investigated samples. The thermal desorption vacuum cleaning method is based on heating up a sample in vacuum to a certain temperature, at which physically and chemically adsorbed species on the surface are desorbed. The minimal temperature which is necessary for full desorption of molecules from the surface is described by following equation

$$T_D = 83.8Q, \tag{3.1}$$

where Q is heat of adsorption or chemisorption (kJ/mol), T_D desorption temperature. Thermal desorption method is used mainly for metallic surfaces because, in this case, heating is realized by applying current. In Table 3.2, data for cleaning a nickel surface are shown.

Table 3.2: Thermal desorption data of Ni surface

Species	Q [kJ/mol]	T_D [K]
Ni+O	545	2600
Ni+CO	147	700
Ni+H	130	620
Ni+CH_4	250	1150

The second cleaning method, which is called sputtering, is performed by using an ion gun. The ion gun is located in the same vacuum volume as the sample (gas for example Ar) is ionized, accelerated by electric field and used to clean the surface. In order to calculate the sputtering rate, the sputtering coefficient is used. This coefficient depends on ion mass, surface atom mass, ion energy, and the angle of incidence. The sputtering coefficient can be calculated using the applied current and the sputter time by equation 3.2

$$S = 26.6\frac{\Delta m}{A \cdot I \cdot t}, \tag{3.2}$$

where Δm is sample mass loss, *g*; *I* - applied current, *Amps*; *t* - time, hours; *A* - molecular mass, kg/mol. Since, sputter ions can penetrate the surface significantly (Ar^+ with energy of 1000 eV penetrate in nickel up to few nm), usually after sputtering, annealing is necessary to do.

In the present work, Ni(111) crystal and polycrystalline yttria-stabilized zirconia (YSZ) are used. The Ni(111) crystal (Mateck, purity ~ 99,99%) was mounted on Ni heating foil and allowed to work in the temperature range of 300-1200 K using direct heating with a PID (proportional-integral-derivative) control unit. The substrate temperature was measured by an Ni-NiCr thermocouple spot-welded to the Ni(111) crystal. The Ni sample was cleaned by reduction of H_2 in atmosphere (10^{-6} mbar) at 1000 K for 30 min, and repeating Ar^+ sputtering (1 keV) for 30 min at room temperature with annealing for 10 min at 1000 K.

A polycrystalline YSZ sample (8.25 mol% Y_2O_3, Itochu Company, Tokyo, Japan), with a thickness of 2 mm, was employed for the investigation of H_2 adsorption/desorption and oxidation studies. As stated by the manufacturer, only trace amounts of impurities, such as Al and Si, exist in the samples. In order to estimate the amount of impurities and their influence on YSZ surface reactions, X-ray photoelectron spectroscopy (XPS) measurements were performed. As can be seen from the XPS spectrum shown in Fig. 3.2, the impurities, such as silica, are present in YSZ sample with the ratios of about 2-3 %. Aluminum was detected also; however, its amount is negligible.

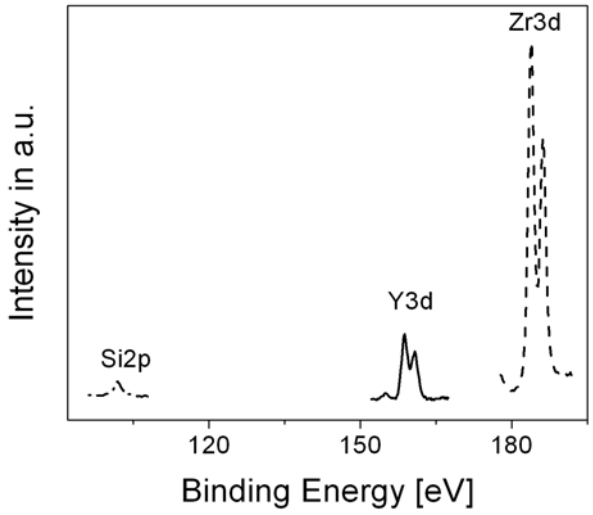

Figure 3.2: XPS spectra of YSZ sample.

The YSZ sample was mounted on a Pt foil on a quartz sample-support, and inserted into the UHV recipient. Prior to the measurements, YSZ sample was heated up to 700 K in vacuum in order to remove adsorbed impurities and physisorbed water. The procedure was recorded using the QMS, to ensure that no water is left in the sample. After cooling down to 300 K, the actual desorption spectrum was obtained by recording the H_2O mass spectrometer (MS) signal while the sample was heated from 300 K to ca. 1200 K with a linear heating rate of 1 K/s.

3.3 Characterization of the samples

The samples (Ni(111) and YSZ) were characterized using Auger electron spectroscopy, low energy electron diffraction and sum frequency generation. A brief overview of the methods used to investigate the samples is described below.

3.3.1 Auger Electron Spectroscopy

The basic principle of AES is depicted in Fig. 3.3 (left). The sample is bombarded by a beam of electrons, consequently, core state electrons can be removed leaving behind a hole. Outer electrons falling into the vacancies may lead either to X-ray emission or the energy may be given to another electron of the atom; this phenomenon is called Auger effect. Such electrons are monoenergetic and an Auger spectrum is a specific characteristic of the atom. The energy of an Auger electron is determined by the binding energies of the electrons involved.

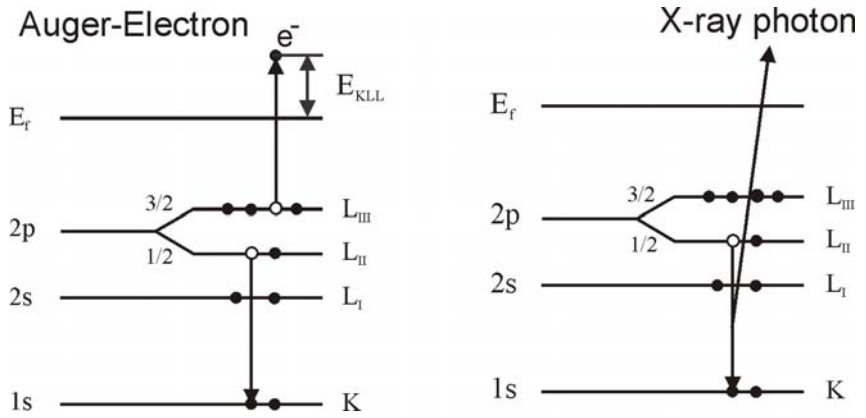

Figure 3.3: Schematic picture of Auger electron (left) and X-ray photon (right) emission.

In the AES experiment, the sample is irradiated with electrons from an electron gun and the emitted electrons are analyzed by an electron spectrometer. For Auger measurements, a grazing angle of incident electrons is needed, to maximize the contribution of surface atoms. In order to detect the electrons with certain energy, the voltage on the retarding grid may be modulated to detect just that energy. A more detailed description of AES method is given in Ref. [45].

3.3.2 Low Energy Electron Diffraction Spectroscopy

LEED spectroscopy is surface sensitive technique, in which a beam of electrons of a well defined low energy (usually about 10 to 200 eV) incidents normally to the surface. The sample itself must be a single crystal with a well ordered surface structure in order to generate a back-scattered electron diffraction pattern. The basic principle of LEED is shown on the left hand side in Fig. 3.4. The hot filament inside the electron gun produces electrons which accelerate and go through several grids. The first grid is at potential of the crystal, and the second is a repelling grid which allows only electrons of original energy to pass and, hence, electrons of lower energy

are stopped. The third grid is positively charged in order to accelerate the accepted electrons on the fluorescent screen.

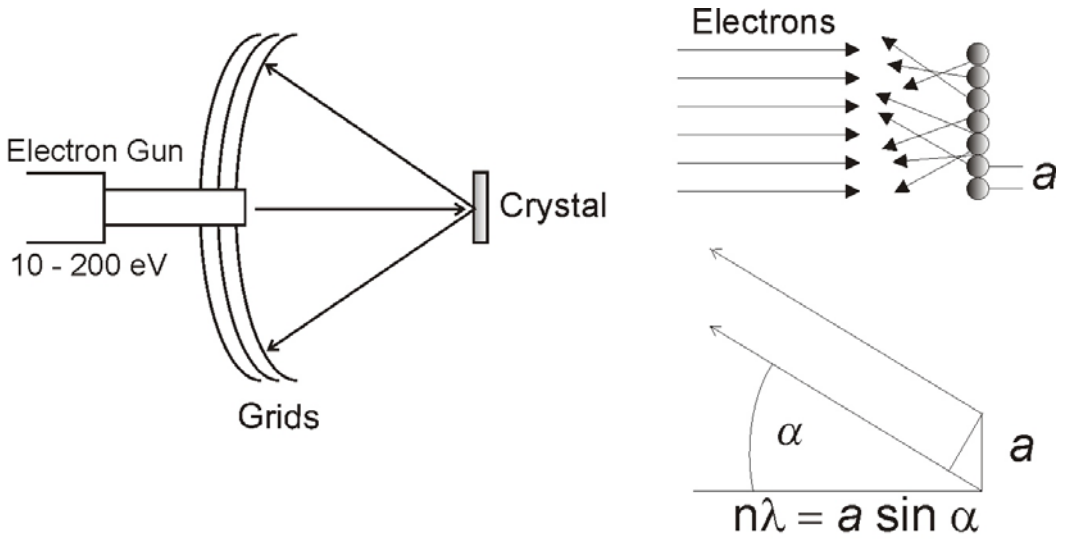

Figure 3.4: The principle of LEED spectroscopy

On the right hand side of Fig. 3.4, the conditions of LEED picture appearing are shown. The Laue condition for incidence normal to the surface is

$$n\lambda = a\cos\alpha\,, \tag{3.3}$$

where n is a integer, a is the repeating distance in one direction, and λ is the wavelength of the electrons. The diffraction pattern consists of a small number of spots whose symmetry of arrangement is that of the surface grid of atoms.

The main objective of a LEED study is the determination of the surface structure and adsorbate structure on the surface. However, sometimes the interpretation of LEED pattern is very difficult. Since LEED pattern is not just a picture of the surface, but rather one of the reciprocal lattice and in the case of an adsorbate structure on the surface, the difficulties appeared when the structure becomes diffuse. Also, there are more than one possible surface structured giving the same LEED pattern. In order to decide between the possibilities, it is necessary to make calculations for each of the intensity, as well as the position of the spots in the pattern.

3.3.3 Sum Frequency Generation Spectroscopy

Visible-infrared sum frequency generation is a nonlinear optical technique capable of generating vibrational spectra. Chemical species can be identified; molecular orientation and molecular surface density can also be measured with this technique. This process is allowed (in the electric dipole approximation) only in a medium without a center of centrosymmetry [46]. The principle schema of SFG signal generation is shown in Fig. 3.5. The tunable infrared (ω_{IR}) is mixed with a

visible (ω_{vis}) laser beam to generate a sum frequency output ($\omega_{SFG} = \omega_{IR} + \omega_{vis}$). The VIS beam is held at a fixed frequency while the IR beam is tuned over the vibrational frequency range of interest.

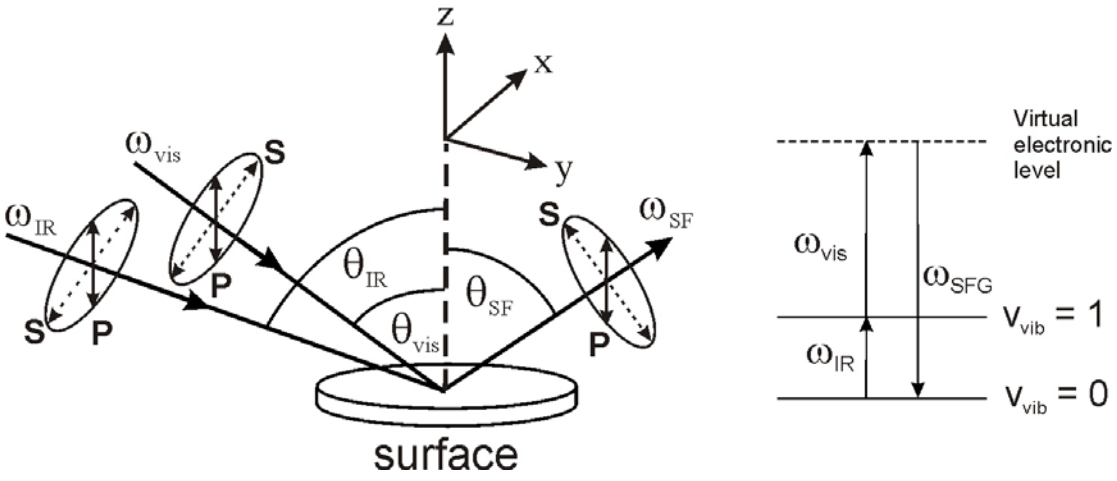

Figure 3.5: Schematic description of the optical arrangement and the possible excitation/detection polarization configuration of the SFG surface vibration spectroscopy studies on the metal surface.

When the IR beam is tuned across a surface species vibrational resonance, the effective surface non-linear susceptibility $\chi_s^{(2)}$ is resonantly enhanced. Since the SFG intensity $I_{SFG}(\omega_{IR})$ is proportional to the absolute square of the effective surface nonlinear susceptibility [47]

$$I_{SFG}(\omega_{IR}) \propto \left|\chi_s^{(2)}\right|^2 = \left|\chi_R^{(2)} + \chi_{NR}^{(2)}\right|^2, \tag{3.4}$$

a vibrational spectrum of the adsorbed molecules can be measured. In (3.4) $\chi_s^{(2)}$ is a third-order tensor which is modeled in lower order as the sum of a non-resonant $\chi_{NR}^{(2)}$ and resonant $\chi_R^{(2)}$ terms. The resonant term is associated with a vibrational mode of the adsorbate [48], but non-resonant contributions originate from the adsorbate, the surface, or from cross terms resulting from adsorbate-surface interaction. Sometimes non-resonant contributions from the surface can be of the same order as the magnitude of the resonant contribution [49, 50].

3.4 TPD/TPR spectroscopy

3.4.1 The Basic Principles of TPD/TPR Technique

Temperature programmed desorption and reaction is a well-established experimental method for the determination of kinetic and thermodynamic parameters of desorption processes and decomposition reactions on the surface. The TPD/TPR technique was firstly described by Apker [51] and it has been widely used since the 1950's to obtained the energetics and surface

stoichiometry for adsorbates on polycrystalline wires and ribbons [52, 53]. Later on, TPD/TPR method was successfully applied to single crystal planes [54, 55].

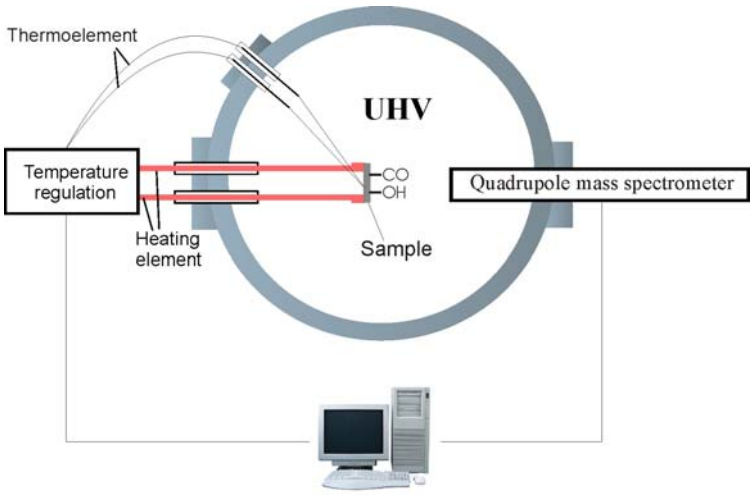

Figure 3.6: The schema of TPD/TPR experimental apparatus

The principle scheme of the TPD/TPR experimental set up is shown in Fig. 3.6. The TPD/TPR experiment is based on two principles a) adsorption of one or more molecular species onto the sample surface at low temperature (usually at 300 K) and b) heating of the sample with a controlled speed (the temperature usually being a linear function of the time) and monitoring the evolution of species from the surface into the gas phase. Adsorption takes place when an interaction between a particle and a surface is strong enough to overcome the disordering effect of thermal motion. If the interaction is the results of van-der-Waals forces, physisorption takes place (energy below 50 kJ/mol). Chemisorptions occur when the overlap between molecular orbital of the adsorbed particle and the surface allow the formation of chemical bonds with the energy input exceeding 50 kJ/mol.

In TPD/TPR spectra, the most important features are the area under a peak, the peak profile and the peak position. The area under a peak is proportional to the amount of originally adsorbed molecules, which is proportional to the surface coverage. The position of the peak (the peak temperature) is related to the enthalpy of adsorption, i.e., to the strength of binding to the surface.

3.4.2 The Analysis of TPD/TPR Spectra

The analysis of TPD/TPR spectra is based on several models: a) Wigner-Polanyi model, b) Redhead desorption peak temperature method, c) peak-area analysis, d) peak-width analysis and e) peak-shape analysis.

In the Wigner-Polanyi model, it is assumed that the rate of desorption from a species on a surface may be written as

$$\frac{\mathrm{d}N(T)}{\mathrm{d}T} = -\frac{k_0}{\mu}[N(T)]^n \exp(-E_\mathrm{d} / k_\mathrm{B}T)\,. \qquad (3.5)$$

In this equation, k_0 is the rate constant (1/s), μ is the heating rate (K/s), E_d is the activation energy of desorption, T is the temperature of the sample, n is the order of the reaction, k_B is the Boltzmann constant, $N(T)$ is the number of adsorbed species in sample (molecules/cm^2). If the pumping speed and heating rate are such that the desorption rate is proportional to the pressure, Redhead [53] showed that for first order desorption (n = 1) the activation energy for desorption is related to the peak temperature according to

$$E_d = RT\left[\ln(\nu_i T_p / \beta) - 3.46\right], \tag{3.6}$$

where β is the heating rate, $\nu_i = 10^{13}$ (1/s) is attempt frequency, T_p peak temperature.
The activation energy of desorption can be obtained using peak-area analysis. If the desorption spectrum obeys Eq. (3.5), the desorption rate can be expressed as

$$R(T) = -\frac{dN}{dT} = \nu_0[N(T)]^n \exp(-E_d / k_B T). \tag{3.7}$$

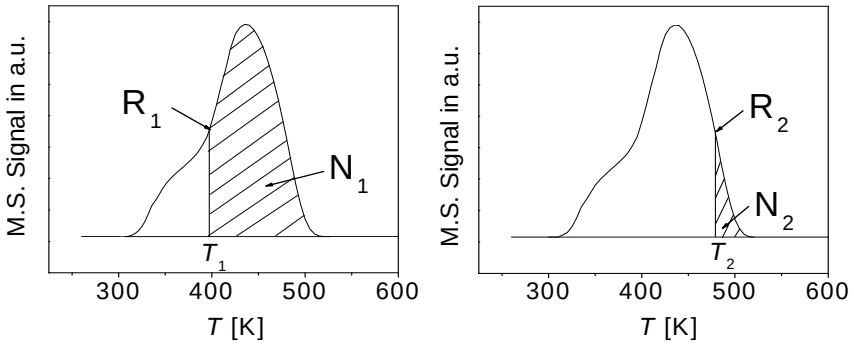

Figure 3.7: Determination of the number of desorbing particles for two different temperatures.

The two temperatures, T_1 and T_2, are chosen on the same TPD curve, such that $T_1 < T_p < T_2$, where the rates of desorption are equal ($R_1 = R_2$), see Fig. 3.7. In this assumption, one can write

$$\nu_0 N_1^n \exp(-E_d / k_B T_1) = \nu_0 N_2^n \exp(-E_d / k_B T_2), \tag{3.8}$$

where N_1 and N_2 are absolute numbers of particles remaining in the sample at given temperatures. Solving equation (3.8) for E_d, the following expression is obtained

$$E_d = \frac{n k_B T_1 T_2}{T_1 - T_2} \ln\left(\frac{N_2}{N_1}\right), \tag{3.9}$$

This method gives relatively good results; however, some difficulties may arise when eliminating the background which usually differs from zero.
The other method for TPD spectra analysis was developed by Chan et al. [56] and is called peak-width analysis. In this method, maximum peak temperature and half-width are combined. The expressions for first-order desorption become as following,

$$E_{\mathrm{d}} = RT_{\max}\left[-1+\sqrt{\left(\frac{W}{T_{\max}}\right)^2+5.832\frac{T_{\max}}{W}}\right], \tag{3.10}$$

in which, W is half-width. The peak width analysis is a complicated method because the determination of the half-width of an experimental desorption curve is often difficult. However, this method gives a reasonable approximation for the activation energy, or reference results when the analysis is based on the peak shift with different temperatures.
The basic aspects of TPD spectra analysis using peak-shape analysis is given by Habenschaden and Küppers [57]. It is based on solution of the Wigner-Polanyi equation (3.5)

$$R_{\mathrm{n}} = \frac{\mathrm{d}N(T)}{\mathrm{d}T} = \frac{\nu}{\mu}\exp\left[-\frac{\nu}{\mu}\int_{T_0}^{T}\exp(E_{\mathrm{d}}/k_{\mathrm{B}}T)dT\right]\exp(-E_{\mathrm{d}}/k_{\mathrm{B}}T), \tag{3.11}$$

where, T_0 is the temperature at which the peak begins to increase, $N(T)$ is the number of trapped atoms remaining in the sample at temperature T.
The peak-shape method is quite satisfying, and it also can be used when peaks are partially overlapped. However, this method is very sensitive to noise and cannot be used at the peak maximum point.
The most common method for finding the pre-exponential factor A experimentally is to perform the TPD/TPR experiment at more than one heating rate [58-60]. The pre-exponential factor is constant near the maximum of a peak and can be described by equation (3.8),

$$\ln\left(\frac{\beta}{T_{\mathrm{p}}^2}\right) = \ln\left(\frac{AR}{E}\right) - \frac{E}{R}\left(\frac{1}{T_{\mathrm{p}}}\right). \tag{3.12}$$

The graph of $\ln\left(\beta/T_p^2\right)$ against $1/T_{\mathrm{p}}$ will be linear and the intercept point gives A factor. Here, the main difficulty is the determination of the peak temperature accurately for broad distribution in the presence of experimental noise. Also, the method requires a long extrapolation of the data to find the intercept; and the heating rate needs to be varied by at least an order of magnitude. However, this method gives the possibility to get a relatively fast and accurate estimation of pre-exponential factor.

4. Electrochemical Modeling and Simulation

The basic principles of electrochemistry, elementary kinetics and electrochemical modeling and simulation of Ni/YSZ SOFC anode are described in this chapter. The kinetic and thermodynamic descriptions of electrochemical systems are given in first subchapter (4.1). In the second subchapter (4.2), the elementary kinetics approach of gas and surface phase along with charge transfer processes is described. Paragraph 4.3 describes the elementary kinetic modeling of Ni/YSZ SOFC anode electrochemistry. The numerical simulation technique used in this study is given in last, subchapter (4.4).

4.1 Electrochemistry

The connection between chemistry and electricity is a very old one. It goes back to Alessandro Volta's discovery, in 1793, that electricity could be produced by placing two different metals on opposite sides of a moistened paper. Later on, in 1800, Nicholson and Carlisle, using Volta's battery, showed that an electric current could decompose water into oxygen and hydrogen. Based on lateral experiments, Humphrey Davey prepared the first elemental sodium by electrolysis of a sodium hydroxide melt. Davey's assistant, Michael Faraday, showed that there is a direct relation between the amount of electric charge passed through the solution and the quantity of electrolysis products. In 1905, Julius Tafel found that electric currents passing across metal–solution interfaces could be increased exponentially by changing the electric potential of the electrode across the surface through which they pass. That was the basis of modern electrochemistry.

In an electrochemical system such as the SOFC, the gradient in the electrochemical potential is the driving force for reactions occurring inside the system. If the system has reached the equilibrium, this gradient has vanished and an electrical voltage, *E,* has formed between the electrodes. At equilibrium, the relation [61, 62]

$$\Delta_R G = -zFE\,, \tag{4.1}$$

follows from thermodynamic considerations, relating the free reaction Enthalpy ΔG of the global reaction to the product of Faraday's constant, F, the number of transferred electrons, z, and the cell voltage, E. Globally, the carbon monoxide oxidation reaction can be written as

$$CO + 1/2\ O_2 \rightarrow CO_2\,, \tag{4.2}$$

The change of Gibbs energy is

$$\Delta_{\mathrm{R}} G_{\mathrm{m}} = \sum_{i=1}^{i} \mu_{\mathrm{i}}^{0} + RT \ln\left(\frac{a(\mathrm{CO}_2)}{a(\mathrm{CO}) \cdot a(\mathrm{O}_2)^{1/2}} \right). \tag{4.3}$$

In the equilibrium, $\Delta_{\mathrm{R}} G = 0$, the chemical potential μ_{i}^{0} is proportional to logarithm of equilibrium constant

$$-\sum_{i=1}^{n} \mu_{\mathrm{i}}^{0} = RT \ln K\,, \tag{4.4}$$

since $\Delta_R G^0 = -RT \ln K$ the change of Gibbs free energy for the reaction (4.2) follows the equation (4.5)

$$\Delta_{\mathrm{R}} G_{\mathrm{m}} = \Delta G^0 + RT \ln\left(\frac{a(\mathrm{CO}_2)}{a(\mathrm{CO}) \cdot a(\mathrm{O}_2)^{1/2}} \right). \tag{4.5}$$

Substitution of the Gibbs energy expression for electrochemical system (4.1) in the last equation gives the Nernst equation [63, 64]

$$E = E^0 - RT \ln\left(\frac{a(\mathrm{CO}_2)}{a(\mathrm{CO}) \cdot a(\mathrm{O}_2)^{1/2}} \right). \tag{4.6}$$

In Eq. (4.6), E^0 is a constant that depends on the nature of the electrode reaction; it is equal to the electrode potential if activities are unity. Generally, the electrode potential E depends mainly on the value of this constant, since the second term of this equation, which is the correction term for concentrations, is relatively small, although in certain cases it becomes the major term. The components that are involved in the electrode reaction, and therefore influence the value of the electrode potential, are called potential-determining substances. From the last equation it follows that the potential will shift in the positive direction when the concentration of the oxidizing agent, or of components entering the reaction together with it, is raised. However, the potential will shift in the negative direction when the concentration of the reducing agent, or of components entering the reaction together with it, is raised [62].
The cell voltage at equilibrium is given by the difference in the electrical potential of the anode $\Delta\phi_{elde,an}$ $\Delta\phi_{\mathrm{elde,an}}$ and the cathode $\Delta\phi_{elde,ca}$

$$E = \Delta\phi_{elde,ca} - \Delta\phi_{elde,an}\,, \tag{4.7}$$

and if current is drawn from the cell, the cell voltage and the potential steps become dependent on the cell current i:

$$E(i) = \phi_{\text{elde,ca}} - \phi_{\text{elde,an}}(i) \,. \tag{4.8}$$

4.2 Elementary Kinetics

One of the goals of elementary kinetic models is the prediction of the macroscopically observable electrochemical performance, such as steady polarization behavior or electrochemical impedance. For this reason, an electrode-level modeling framework is required that describes the quantitative relationship between mean-field reaction kinetics, transport processes, voltage and potential [65].

The reaction that takes place causes the transformation of reactants A' into products A'' with stoichiometric coefficients ν' and ν'', respectively, via next equation

$$\sum_{i \in R_{\text{f}}} \nu_i' A_i' + z e^- \quad \sum_{j \in R_{\text{r}}} \nu_j'' A_j'' \,, \tag{4.9}$$

where, z denotes the number of electrons transferred. In this thesis, the reactions are formulated in the direction of reduction and assumed to proceed at the interface of a solid electrolyte and a solid electrode, until thermodynamic equilibrium is reached.

An electrical potential difference between the electrolyte and electrode appears when charge is transported and described by the following equation

$$\Delta\phi = \phi_{\text{elde}} - \phi_{\text{elyt}} \,, \tag{4.10}$$

where ϕ_{elde} is the electrical potential of the electrode and ϕ_{elyt} represents the electrical potential of the electrolyte just beyond the space-charge region.

The kinetics of reaction (4.9) are characterized by the forward and reverse reaction rates $k_{\text{r/f}}$ derived from transition state theory [63]

$$k_{\text{f,ct}} = k_{\text{f,ct}}^{0} \exp\left(-\frac{E_{\text{f,ct}}^{\text{act}}}{RT}\right) \exp\left(\beta_{\text{a}} \frac{zF}{RT} \Delta\phi\right), \tag{4.11}$$

$$k_{\text{r,ct}} = k_{\text{r,ct}}^{0} \exp\left(-\frac{\Delta_{\text{R}} G_{\text{m}}}{RT}\right) \exp\left(\beta_{\text{c}} \frac{zF}{RT} \Delta\phi\right), \tag{4.12}$$

where $E_{\text{f,ct}}^{\text{act}}$ is the activation energy for forward charge transfer reaction, β is the symmetry factor. According to the mass action law, the net change of species i due to an electrochemical reactions is given by the rate $\dot{s}_{\text{i}}$ [64]

$$\dot{s}_\mathrm{i} = \nu_{\mathrm{i,m}} (k_{\mathrm{f,m}} \prod_{j \in R_\mathrm{f}} A_j^{\nu_j'} - k_{\mathrm{r,m}} \prod_{j \in R_\mathrm{r}} A_j^{\nu_j''}) , \tag{4.13}$$

where $\dot{s}_\mathrm{i}$ and A can be given as volumetric or area specific quantities. If a charge species participates in the reaction, the rate $\dot{s}_\mathrm{i}$ causes an electric current density

$$j_\mathrm{i} = zF\dot{s}_\mathrm{i} . \tag{4.14}$$

4.2.1 Gas Phase Chemistry

Usually, in the modeling of SOFC operation the gas phase chemistry itself is assumed nonreactive and the gas phase composition is supposed to be constant at every point. However, as has been shown by Walters et al. and Sheng et al. [66, 67], the gas phase reactions can occur on the anode side particularly in the case of direct feed with higher hydrocarbons.

The gas phase reaction rate is described by Eq. (4.11) and (4.12) along with net changing of species *i* using Eq. (4.13). Pre-exponential factors and activation energies are connected via an equilibrium relation $\Delta_\mathrm{R} G_\mathrm{m} = \Delta_\mathrm{R} H - T\Delta_\mathrm{R} S$ [68]

$$E_\mathrm{f}^\mathrm{act} - E_\mathrm{r}^\mathrm{act} = \Delta_\mathrm{R} H , \tag{4.15}$$

$$\frac{k_\mathrm{f}^0}{k_\mathrm{r}^0} = \exp\left(\frac{\Delta_\mathrm{R} S}{R} \right). \tag{4.16}$$

The gas mixture is described in terms of the mass density ρ, the total concentration $c_\mathrm{tot} = \sum c_\mathrm{i}$ and the mean molar mass $\overline{M} = 1/c_\mathrm{tot} \sum c_\mathrm{i} M_\mathrm{i}$. In this thesis, it is assumed that all gasses are ideal

$$\rho = \frac{p\overline{M}}{RT} , \tag{4.17}$$

where p is the pressure.

The volumetric source terms of the gas-phase species $\dot{s}_\mathrm{i}^\mathrm{V}$ are calculated applying mass action law (Eq. 4.13) using the software package DETCHEM [69].

4.2.2 Surface Chemistry

In order to describe processes which take place on the surface, we use analogous equations as in gas phase chemistry. For the description of species surface coverages, the so called mean-field approach is used [70, 71]. It is assumed that the state of adsorbed surface species can be described using averaged quantities, such as surface coverages, thermodynamic and kinetic adsorbate properties. The defects on surface (steps, kinks, crystal disorders) occurring on an

atomic scale are not further resolved and are assumed to be included into the mean-field quantities. The coverage (θ_i) of species *i* is dimensionless

$$\theta_i = \frac{c_i \cdot \sigma_i}{\Gamma_k}, \tag{4.18}$$

where, σ_i is number of surface sites occupied by species *i*, c_i concentration of species *i* which is normalized to the total available surface sites (Γ_k).The species production rates follow, again, from mass action kinetics, yielding the so-called rate equations

$$\frac{\partial}{\partial t}\theta_i = \frac{\sigma_i}{\Gamma_k}\dot{s}_i^A, \tag{4.19}$$

The coverages of surface species are coupled to the concentration of gas-phase species by heterogeneous chemistry. The heterogeneous reaction mechanisms of fuels oxidation take place via Langmuir-Hinshelwood and Eley-Rideal reaction pathways.

4.2.3 Charge Transfer

The charge transfer happens when a charged species is transferred from one phase to another. The driving force of charge transfer is the voltage difference between two phases established by a double layer of charge at the solid interface. Knowledge of the variation of charge transfer rate with electrode potential is important for the understanding of electrochemical reactions.

Different approaches are used to calculate the current resulting from the charge transfer via electrochemical reactions. The first method was introduced in 1924 by John Alfred Valentine Butler (1899–1966) and completed in 1930 by Max Volmer (1885–1965) and Tibor Erdey-Gruz (1902–1976) who developed the concept of a finite rate of charge transfer and of the influence of the electrode potential on this rate. J. Butler developed the idea that Nernst equilibrium potential for an electrochemical process is the potential at which the forward and back reactions proceed at the same rate [72]. Later on, based on this approach, Bowden and Rideal [73] introduced the term j_0 as the value of forward and back current density at the reversible Nernst potential and wrote the Tafel equation in the following way

$$\eta = b(\log j - \log j_0), \tag{4.20}$$

The charge transfer coefficient α was introduced by Erdey-Gruz and Volmer in 1930, replacing Tafel's constant *b* by expression $RT/\alpha F$

$$\log j = \log j_0 - \frac{\alpha \eta F}{RT}, \tag{4.21}$$

$$j = -zFk^0 C \exp\left(-\frac{\alpha\eta F}{RT}\right). \tag{4.22}$$

For the general electrochemical reaction $\mathrm{Ox} + ne^- \rightleftharpoons \mathrm{Red}$, the current density j is related to the activation overpotential of the electrode η_{act} by the following equation

$$j = j_0\left[\exp\left(\alpha_{\mathrm{a}}\frac{F}{RT}\eta_{\mathrm{act}}\right) - \exp\left(-\alpha_{\mathrm{c}}\frac{F}{RT}\eta_{\mathrm{act}}\right)\right], \tag{4.23}$$

where α is the charge transfer coefficient, for anodic and cathodic reactions, respectively.
Charge transfer coefficient α and symmetry factor β in electrode reactions have fundamentally different meanings. The exponential term which relates current density to overpotential, factor β, will appear when the rate determining charge transfer step is written exclusively, or it will appear for the simple reaction consisting of one such step alone. On the other hand, the transfer coefficient α will appear for the overall current density potential expression of multistep reactions. It means that α is a multistep version of β. The charge transfer coefficient includes parameters relating to the mechanism of the overall reaction, in particular, the number of electrons which precede the rate determining step. The symmetry factor is connected with the relative potential distance variation of the bonding in the initial and the final states of the reaction [74].
Other approach for calculating current, resulting from the charge transfer via electrochemical reactions, was proposed by Goodwin, Kee and co-workers [75, 76]. They used the mass action formulation instead of Butler-Volmer expression. For the hydrogen oxidation within SOFC anode, they obtained the following analytical equation for the exchange current density

$$i_0 = i^*_{\mathrm{H_2}}\frac{\left(p_{\mathrm{H_2}} / p^*_{H_2}\right)^{1/4}\left(p_{\mathrm{H_2O}}\right)^{3/4}}{1+\left(p_{\mathrm{H_2}} / p^*_{H_2}\right)^{1/2}}, \tag{4.24}$$

In the derivation of latter equation, the authors [76] assumed that only charge transfer process can determine the rate of electrochemical fuels oxidation that means fast heterogeneous chemistry and fast transport on the surface. Following this approach, the surface is always in equilibrium with the gas phase.
In contrast to the electrochemical approaches described above, in this thesis, a physically based modeling framework [77] is used. In this model, the charge transfer reaction is described based on elementary reaction kinetics and takes place over the interface between electrolyte and electrode. It is assumed that charge transfer reaction occurs as “line reaction” and is associated with mass transport over the three phase boundary (TPB). The length of TPB, l_{TPB}, is given as an area-specific quantity ($l^{\mathrm{A}}_{\mathrm{TPB}}$). The Faradaic current density ($i^{\mathrm{A}}_{\mathrm{F,ct}}$), obtained from the charge

transfer process with respect to the surface area of the whole cell, is described by following equation

$$i_{\mathrm{F,ct}}^{\mathrm{A}} = zFl_{\mathrm{TPD}}^{\mathrm{A}}(k_{\mathrm{f,ct}} \prod_{j \in R_{\mathrm{f,ct}}} \theta_j^{\nu_j^{'}} - k_{\mathrm{r,ct}} \prod_{j \in R_{\mathrm{f,ct}}} \theta_j^{\nu_j^{''}}), \tag{4.25}$$

The forward $k_{\mathrm{f,ct}}$ and reverse $k_{\mathrm{r,ct}}$ rate constants in Eq. (4.25) are calculated using equations (4.11) and (4.12). If more than one electrochemical reaction takes place, the overall current density ($i_{\mathrm{F}}^{\mathrm{A}}$) is the sum over all charge transfer reactions

$$i_{\mathrm{F}}^{\mathrm{A}} = \sum_{\text{all CTRs}} i_{\mathrm{F,ct}}^{\mathrm{A}}, \tag{4.26}$$

The set of Eq. (4.11), (4.12), (4.25), (4.26) represents an elementary kinetic view of charge transfer. It entirely describes the relationship between the physical quantities $i_{\mathrm{F,ct}}^{\mathrm{A}}$, $\Delta\phi$ and surface coverage θ. Also, these equations are valid if the system is in electrochemical equilibrium while it allows to predict equilibrium half-cell electric potentials by setting $i_{\mathrm{F,ct}}^{\mathrm{A}} = 0$ and solving for $\Delta\phi$.

The advantages of detailed elementary kinetic approach for modeling the charge transfer in SOFC over the Butler-Volmer type kinetics are:

- The potential difference entering the rate equations are “real” physical potential steps due to the formation of electrical double layers at the interfaces of the electrodes with the electrolyte.
- The description of charge transfer, using elementary kinetics, allows resolving the full kinetic coupling of all processes governing fuel cell performance.
- There is no need for an a priori assumption of a rate-determining step. In contrast, this approach allows identifying the relevance of individual processes.
- The model is applicable to non-equilibrium conditions.
- The open-circuit voltage is not an input into the model but a model prediction.

4.2.4 Charge transfer of oxygen anion in Ni/YSZ model anode

At a fundamental level, the processes responsible for generating current at the electrodes are electron-transfer reactions, in which an electron transfers between a delocalized conduction-band state within the metal electrode and a localized molecular orbital. The electron transfer to or from the conduction band of the electronic conductor is generally accompanied by the transfer of a charged species from the electrolyte surface to the electrode surface across the TPB or vice versa. An understanding of this process is achieved in the Marcus theory of electron transfer kinetics [78-80]. The potential difference between electrolyte (YSZ) and electrode (Ni) provokes the change in potential energy of the oxygen anion on the YSZ surface and discharges oxygen on Ni surface. Marcus theory assumes that reactant and product vibrate harmonically and with identical frequency so that the potential energies of both components in a redox couple can be

represented by identical but shifted parabolas. This may be understood by considering Fig. 4.1, which illustrates CT reaction O2. In the reactant configuration, an adsorbed single ionized oxygen atom on the electrolyte near the TPB is in close proximity to a nickel surface. The electronic energy of this configuration is a function of the nuclear coordinates, shown schematically in one dimension as the potential surface (left part of Fig. 4.1). If an electron is removed from oxygen anion, a different potential energy surface is obtained. This is shown as the potential surface on the right where now the minimum energy position corresponds to the discharge oxygen being adsorbed on Ni surface. The intercept of two parabolas correspond to the transition state for electron transfer.

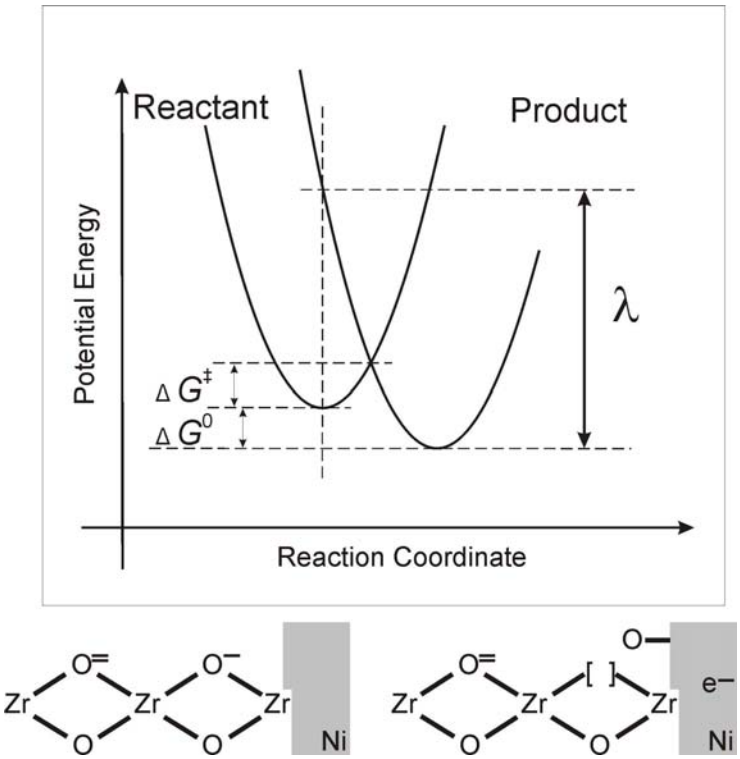

Figure 4.1: Schematic illustration of the CT reaction O2 in the framework of Marcus theory

The standard Gibbs energy within Marcus theory is given by following equation

$$\Delta G^{\ddagger} = \frac{(\lambda + \Delta G^{0})^{2}}{4\lambda}, \tag{4.27}$$

where, ΔG^{0} is the standard Gibbs energy and the λ is the reorganization energy of the system. The parameter λ is the change of Gibbs energy associated with reorganization of the potential

energy of species to their equilibrium positions. The transfer coefficient α and symmetry factor β are expressed as

$$\alpha = \frac{1}{2} - \frac{F}{2\lambda}|\eta|, \tag{4.28}$$

$$\beta = \frac{1}{2} + \frac{\Delta G^0}{2\lambda} - \frac{F}{4\lambda}|\eta|, \tag{4.29}$$

in which η is overpotential and F is Faraday's constant. From the equations (4.28) and (4.29), the potential dependency of charge transfer coefficient and symmetry factor can be derived by finding the derivatives in terms of η. The value of 0.5 for both α and β, at the standard potential, is associated with the assumption of a single harmonic oscillator with the same frequency in the initial and final states of the CT reaction. The potential dependency of α and β was studied for different electrochemical systems and reported in the literature [81-86]. In addition, the CT coefficient α can be calculated on the certain overpotential region [η_1, η_2] via equation (4.30) [87]

$$\alpha = \frac{1}{2} - \frac{e}{4E^{\text{act}}}(\eta_1 + \eta_2), \tag{4.30}$$

where, E^{act} is the activation energy that interpolates Marcus formula in the available overpotential region. From the last equation it follows that α is smaller than 0.5 for exoergic reactions and greater than 0.5 for endoergic reactions and faster reactions have smaller transfer coefficient. Finally, it should be noted that charge transfer coefficient and symmetry factor could itself be a function of temperature, but this was not confirmed in any available measurements.

4.3 Modeling and Simulations of Ni/YSZ Model Anodes

The simulations of CO electrochemical oxidation are performed within the physically based modeling framework shortly described in this chapter. The full description of the modeling approach is given by Bessler et al. [77, 88] and Vogler [89]. The main assumptions of the present model are:

1) Elementary kinetic description of the chemical processes is applied. A mean-field approach is used for surface chemistry and surface transport. The models are thermodynamically consistent by using reversible reactions throughout.

2) The charge transfer reactions take place at TPB and assumed to be surface spillover.

3) Fickian diffusion approach is used to describe surface diffusion which modeled in one dimension perpendicular to TPB.

4) The gas-phase composition and temperature are assumed to be identical at every point on each TPB line.

4.3.1 SOFC Model Anodes

In the present work modeling and simulations were applied to understand chemical and electrochemical processes which occur on Ni/YSZ point and pattern electrode. As described by Lauvstad et al. [29], a Ni point electrode was prepared by treading a metal wire (99.98% purity Ni, supplied by Goodfellow Corporation) of 0.5 mm diameter in an alumina tube, forming a loop at the top. A contact area approximating an ellipse was obtained by pressing the top of this loop slightly against the electrolyte, as shown in Fig. 4.2.

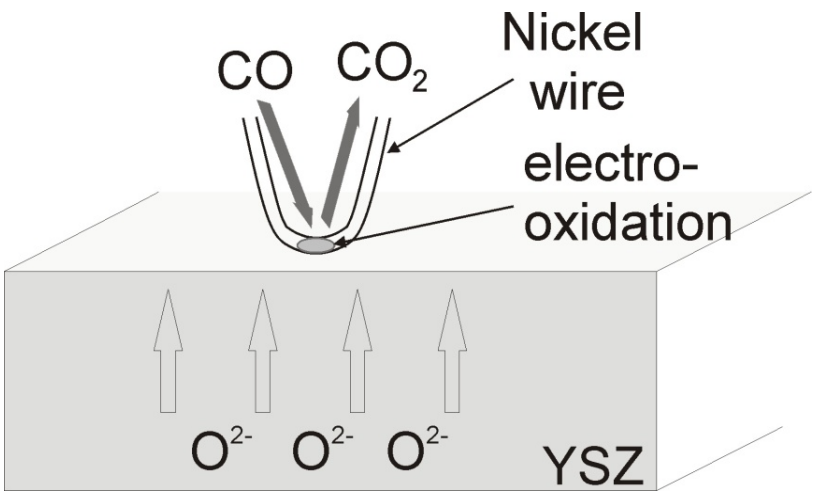

Figure 4.2: Schematic illustration of the Ni point electrode

The contact area is in the range of 0.1 mm^2 and the TPB length about 1 mm. The advantages of point electrodes are 1) the TPB length is well defined, 2) the interface between Ni and YSZ is easy to investigate after an electrochemical experiment, and 3) it is relatively easy obtaining a well defined electrode potential.
The second type of electrode used, is called patterned electrode and is illustrated in Fig. 4.3.

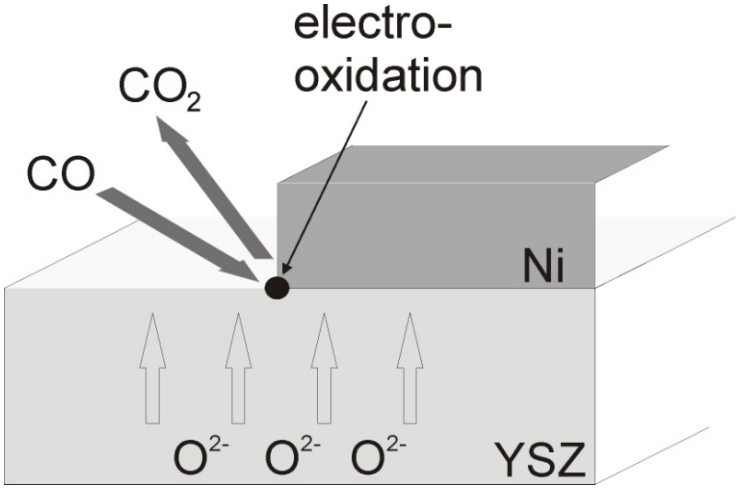

Figure 4.3: Schematic illustration of Ni pattern electrode

For this type of model anode, metal patterns are photolithographically applied on a solid electrolyte substrate. This technique allows obtaining a well-defined contact area and high TPB lengths. The pattern anode is prepare by either a) metal etching: a dense thin metal layer is deposited on the electrolyte substrate or b) metal lift-off: the photoresist is applied, structured and developed on the electrolyte substrate. In the pattern anode, the metal thickness varies from 0.1 to 2 μm, with pattern widths in the range of 5-50 μm. This gives absolute TPB lengths in the range of 1-10 m within a 1 cm^2 electrode [90].

4.3.2 Surface Diffusion

Charge transfer is associated with mass transport over the TPB. This leads to surface and bulk concentration gradient resulting diffusion for both on surface and in the bulk. Here, we assume that, on a microscopic scale, the processes taking place at TPB can be represented in one dimension *z* perpendicular to the TPB line extending onto both electrolyte and electrode surfaces. Diffusion in the bulk lattice structure and the surfaces of electrolyte and electrode are treated using a Fick's law

$$\vec{J}_i = -D_i \cdot \vec{\nabla} \cdot a_i \,. \tag{4.31}$$

The flux $\vec{J}_i$ of a species *i* is proportional to the gradient in the species' concentration and here is given in dimensionless activity a_i ($a_i = \theta_i = \sigma_i / \Gamma_i \cdot c_i$).

4.3.3 Reaction Mechanism

In this work, the elementary kinetic modeling approach is used to describe experimental data on both point and pattern electrodes as schematically illustrated in Fig. 4.4.

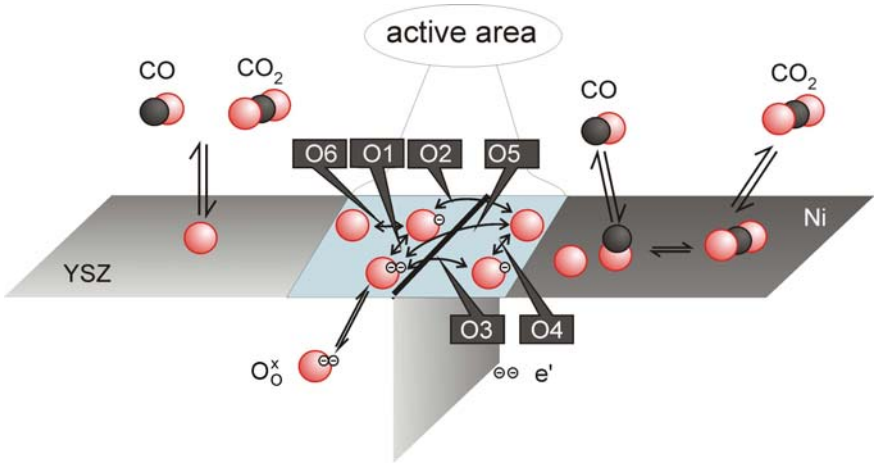

Figure 4.4: SOFC anode modeling: Elementary kinetic reaction-diffusion approach

In the present thesis, four different charge transfer reaction mechanisms are assumed to be present during the CO electrochemical oxidation. All of the charge transfer reactions occur at the TPB of gas phase, electrode and electrolyte. This assumption is based on the respective molecular, electronic and ionic transport properties of the involved phases, where the Ni electrode is a purely electronic conductor and the YSZ electrolyte is essentially a purely ionic conductor.

The charge transfer reactions used in this study are schematically depicted in Fig. 4.4. The first mechanism (O1+O2) consists of two consecutive single-electron CT reactions

O1 $$O^{2-}_{YSZ} \rightleftharpoons O^{1-}_{YSZ} + e^{-}_{Ni}$$

O2 $$O^{1-}_{YSZ} + \square_{Ni} \rightleftharpoons O_{Ni} + \square_{YSZ} + e^{-}_{Ni}$$

The first reaction O1 represents a single electron oxidation step of O^{2-}_{YSZ}, followed by a second reaction O2 representing a spillover with simultaneous CT of O^{1-}_{YSZ} to the Ni surface.

The second mechanism (O3+O4) consists of a first reaction O3, where an O^{2-}_{YSZ} anion initially adsorbed at the YSZ surface spills over to the Ni anode (thereby releasing an electron), followed by reaction O4 during which the O^{1-}_{Ni} anion on Ni is finally discharged

O3 $$O^{2-}_{YSZ} + \square_{Ni} \rightleftharpoons O^{1-}_{Ni} + \square_{YSZ} + e^{-}_{Ni}$$

O4 $$O^{1-}_{Ni} \rightleftharpoons O_{Ni} + e^{-}_{Ni}$$

The third mechanism (O5) represents a single-step oxygen O^{2-}_{YSZ} spillover reaction, in the course of which two electrons are transferred to the Ni anode simultaneously

O5 $$O^{2-}_{YSZ} + \square_{Ni} \rightleftharpoons O_{Ni} + \square_{YSZ} + 2\,e^{-}_{Ni}$$

The fourth mechanism represents the combination of first CT mechanism and the following reaction

O6 $$O^{1-}_{YSZ} \rightleftharpoons O_{YSZ} + 2\,e^{-}_{Ni}$$

The CT reaction O6 is the continuation of reaction O1 in which doubly negative oxygen atoms lose one electron on YSZ surface. The latter CT reaction (O6) can occur in the case when Ni surface is blocked, for example, by oxygen which produces in the reaction of CO_2 dissociation.

4.4 Numerical simulations

Simulation is applied to reproduce the chemical and electrochemical CO oxidation within Ni/YSZ SOFC anode. SOFC anodes consist of three phases which are metal, electrolyte and gas. The schematic illustration of computational approach used in this thesis is shown in Fig. 4.5. It represents the experimental situation of a patterned Ni anode on a YSZ single crystal (Fig. 4.5 a) and b)). Here, the species transport occurs only in *z* direction perpendicular to the TPB (Fig. 4.5 c)).

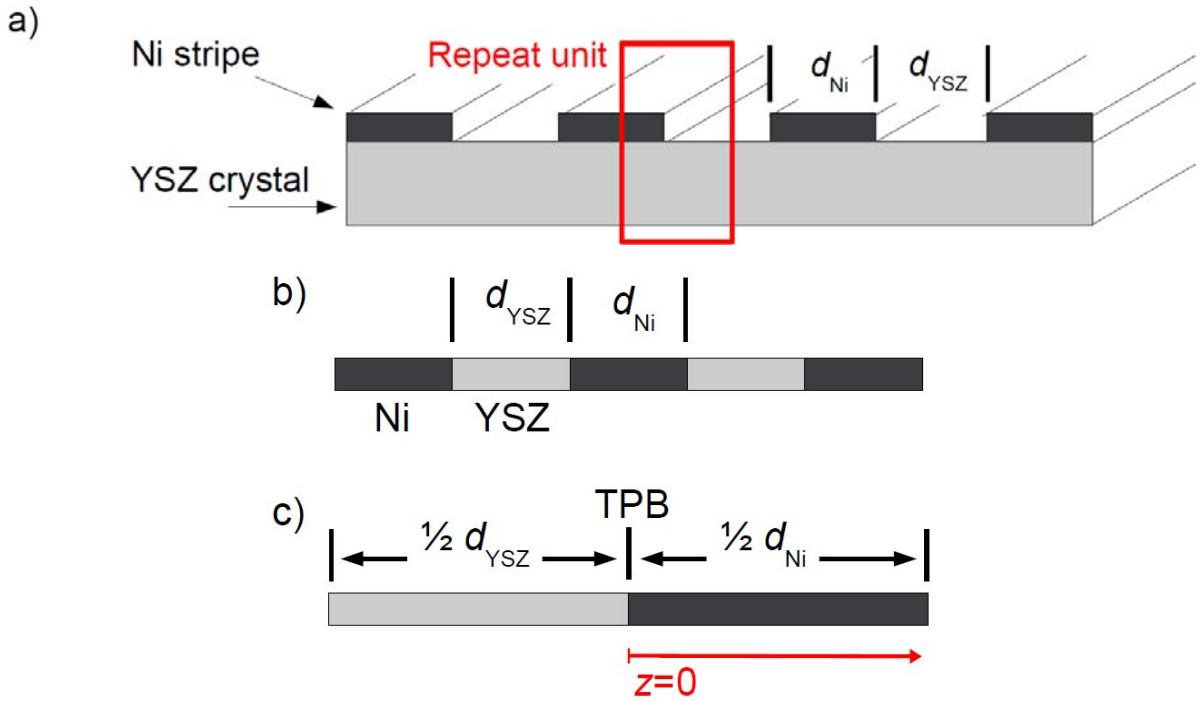

Figure 4.5: Schematic representation of Ni/YSZ anode modeling approach.
a) Schematic view of the 3D pattern geometry, b) and c) illustration of the 3D structure by a 1D model

The modeling approach described in this chapter represents the implicit relationship between current and overpotential. This modeling approach is implemented by Bessler, Gewies and Vogler into the software package DENIS [77]. DENIS software package allows simulation of current voltage relations along with electrochemical impedance spectra.
The coupled chemistry and surface transport are represented by a partial differential equation which spatially discretized using a finite volume technique. The LIMEX [91] is used to solve time-integrated system of differential algebraic equations. Chemistry source terms are calculated using the software package DETCHEM [69]. In order to simulate Tafel plots, the overpotential is set to a constant value and the equation system is solved for the current in the steady state. This is preformed for a range of overpotentials. The polarization resistance, calculated for different overpotentials, holds the same information as a Tafel plot.

5. Results of DFT Calculation on YSZ Surface

Although Ni/YSZ based SOFC are widely used, the actual microscopic details of the electrochemical reaction mechanism occurring at the three-phase boundary of gas-phase, electrode, and electrolyte, are not yet fully understood even for simple electrochemical systems such as carbon monoxide (CO) and hydrogen (H_2). In order to explain the details of fuel oxidation on electrolyte surface within Ni/YSZ SOFC anode, quantum chemical calculations based on density functional theory (DFT) were performed to investigate the molecular energetics of CO and H_2 oxidation.

The computational details of DFT calculations are given in the first subchapter (5.1). The mechanisms of CO oxidation on YSZ surface are described in the second subchapter (5.2). In the third subchapter (5.3), H_2O dissociation, as well as the adsorption and oxidation reaction of H_2 on YSZ, is presented. Finally, in the last part (5.4) of this chapter, the summary of the present DFT calculations is given.

5.1 Computational details

Quantum chemical calculations based on density functional theory were performed to investigate CO/H_2 oxidation and H_2O dissociation energetics on YSZ surfaces. The present calculations were performed using the CASTEP (Cambridge Sequential Total Energy Package) computer code [37] in the framework of the generalized gradient approximation (GGA), as proposed by Perdew and Wang [41], in combination with Vanderbilt ultrasoft pseudopotentials [92]. For systems with an even number of electrons, restricted nonspin-polarized calculations were performed. For systems with an odd number of electrons, unrestricted spin-polarized calculations were carried out. The plane wave basis set was truncated at a kinetic energy of 420 eV. Computations were performed over a range of k-points within the Brillouin zone as generated by the full Monkhorst-Pack scheme [93] with a 2×2×1 mesh. A further increase of the cut off energy and the number of *k*-points resulted in negligibly small changes in adsorption energies (typically less than 5 kJ/mol), indicating that the energy values are well converged. A slab was repeated periodically, leaving at least a 10 Å wide vacuum region in the direction perpendicular to the surface. The atoms of the bottom multilayer were fixed in all calculations, while the positions of atoms of the two outermost multilayers and the positions of atoms of the adsorbed molecules were optimized during the process of structural relaxation. A complete linear synchronous transit (LST)/quadratic synchronous transit (QST) scheme [94] was used in the transition state searches for the surface reaction steps. A force convergence criterion of 0.03 eV/Å was applied in all calculations.

The slabs used in the present study to investigate CO and H_2 oxidation on an oxygen-enriched YSZ surface, denoted as YSZ+O, and H_2O dissociation on a YSZ surface are depicted in Fig. 5.1 a) and b), respectively. Practically, the electrolyte denoted as YSZ+O can be obtained by

supplying O^{2-} anion to an YSZ vacancy, which happened in the regime of anodic polarization of SOFC.

The procedure applied to obtain a representative slab for the (111) surface of YSZ, as shown in Fig. 5.1 b), is similar to the one described in Ref. [95], which starts from a pure (111) terminated zirconia slab, that consists of 12 ZrO_2 formula units with 36 atoms (for further details see Ref. [95] and Fig. 2 therein). From the pure zirconia slab an oxygen atom was removed to account for vacancy formation (denoted as "vac." in Fig. 5.1 b)) and two zirconium atoms were substituted by two yttrium atoms which are depicted as green atoms (Y) corresponding to a 9% mol concentration of yttria in YSZ. The energetically most stable YSZ slab corresponds to the structure with two atoms of yttrium close to each other and preferentially occupying the next-nearest neighbor sites to the oxygen vacancy [96, 97].

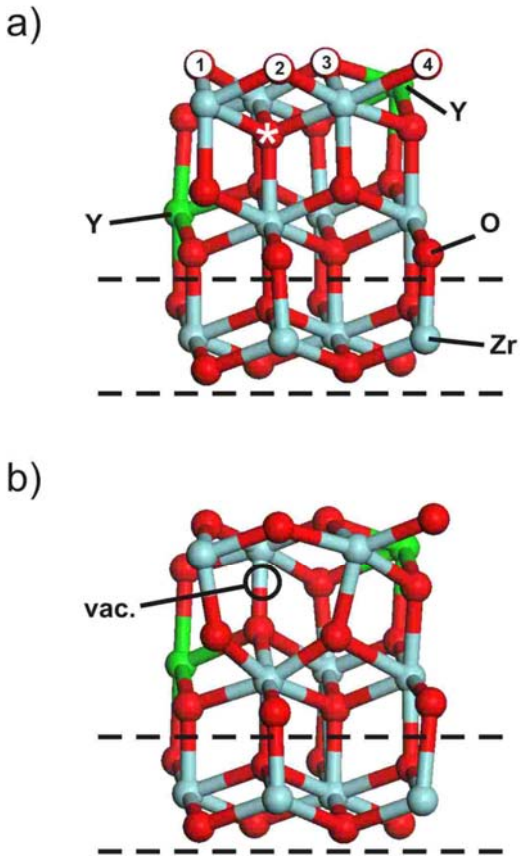

Figure 5.1: Slabs employed in the present DFT calculations: (a) Oxygen rich YSZ+O with the additional oxygen atom (∗) occupying the subsurface oxygen vacancy of YSZ, the structure of which is reproduced in (b) with the positing of the subsurface oxygen vacancy marked as "vac."

Therefore, for calculations, we adopted the mentioned YSZ slab with the subsurface vacancy and two Y atoms, substituting Zr in the outermost and the second surface layers. Finally, in order to generate an oxygen-enriched surface, an additional oxygen atom (marked by ∗ in Fig. 5.1 a)) was

introduced to occupy the subsurface oxygen vacancy of YSZ. The four different surface oxygen atoms of the YSZ+O surface unit cell are indicated by consecutive number O1-O4.

5.2 DFT calculation of CO oxidation over YSZ

We have investigated the oxidation of CO molecule over the YSZ and YSZ+O surfaces. On the YSZ+O surface, CO molecule can get oxidized by taking one of the four surface oxygen atoms (see Fig. 5.1 a)). For the oxidation of CO on all oxygen atoms in the YSZ+O surface, Eley-Rideal mechanism was assumed. The mechanism of CO oxidation can be described as

$$CO + O_{YSZ} \rightleftharpoons CO_2 + \square_{YSZ}, \qquad (5.1)$$

The reaction pathway for CO oxidation on O1 oxygen atom is depicted in Fig. 5.2. The calculation revealed that the adsorption of a CO molecule leads to immediate formation of carbon dioxide (CO_2). The formation of CO_2 is always supported by increase of activation energy from O1 to O4.

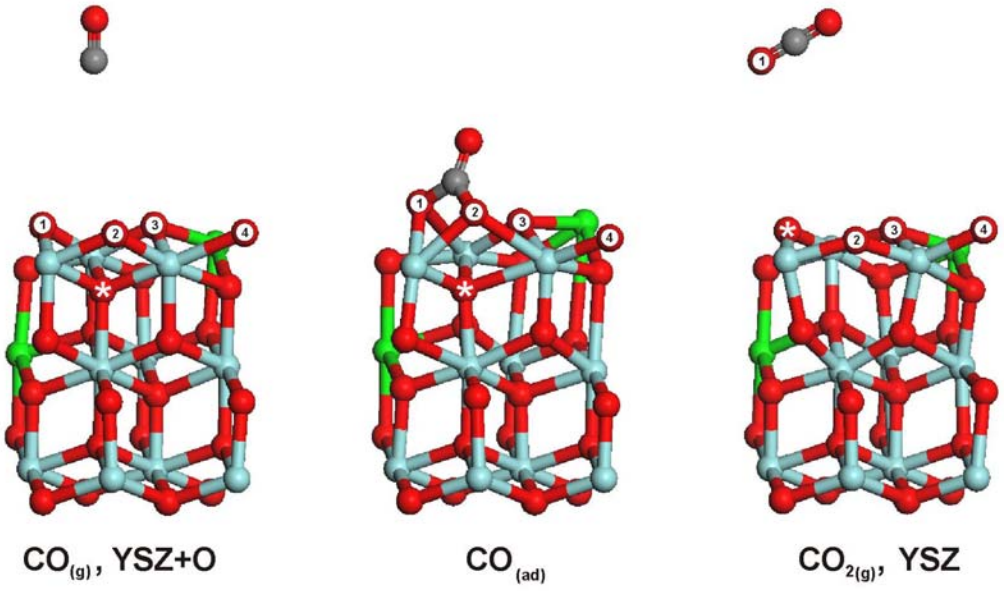

Figure 5.2: Illustration of the surface reaction pathway of the heterogeneous CO oxidation reaction on the YSZ+O surface as obtained in the present DFT studies.

The energetics of the reaction pathway of CO oxidation on an O1 atom is illustrated in Fig. 5.3. The formation of CO_2 occurs with an activation energy of 41.3 kJ/mol and a decrease in enthalpy by –550.2 kJ/mol. The formed CO_2 molecule is weakly adsorbed by oxygen atom to two Zr atoms in the slab. Desorption of CO_2 into the gas phase takes place with an increase in enthalpy by +23.5 kJ/mol and without activation energy. Also, there is no barrier for the backward reaction of carbon dioxide adsorption on the YSZ surface.

The same picture was observed for CO oxidation on O2 which has the same location as O1 in the YSZ+O slab. The formation of CO_2 occurs with the same barrier as in the case O1.

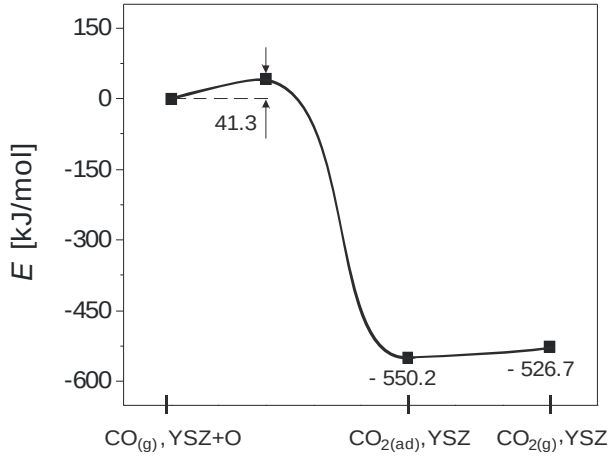

Figure 5.3: The energetics of the CO oxidation reaction on O1 and O2 oxygen atoms.

In the case of third oxygen atom which is bond to one yttrium atom and one zirconium atom in the YSZ+O slab, CO oxidation occurs with different energetics in comparison to CO oxidation on O1 and O2 atoms. Fig. 5.4 shows the energetics of CO oxidation over YSZ+O surface by O3 oxygen atom. As can be observed from this picture, the activation energy of CO_2 formation is 57.6 kJ/mol along with enthalpy decrease by –530.1 kJ/mol.

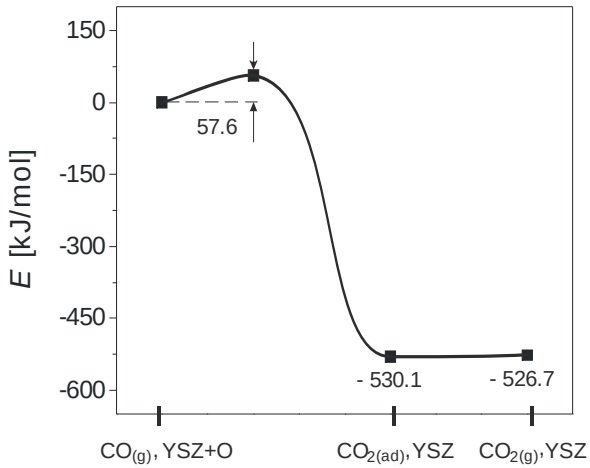

Figure 5.4: The energetics of the CO oxidation reaction on O3 oxygen atom.

In contrast to the previous cases (O1 and O2 oxygen atoms), where CO_2 formation is followed by enthalpy decrease of –550.2 kJ/mol, for O3 atom enthalpy decrease is slightly less (–530.1

kJ/mol). This can be explained by migration of oxygen atom from subsurface layer. Since in the case of O1 and O2, the migrated subsurface oxygen (marked with star in Fig. 5.3 a)) is bonded to two zirconium atoms, and for O3 oxygen migrated subsurface oxygen atom is bonded to yttrium and zirconium atoms.

Finally, we have investigated the oxidation of CO on O4 oxygen atom. The energetic pathway of this process is depicted in Fig. 5.5. The formation of carbon dioxide takes place with the highest activation energy (115.2 kJ/mol), in contrast to previous cases, and the decrease of enthalpy is slightly higher and reaches a value of –552.2 kJ/mol. Desorption of the CO_2 molecule into the gas phase is accompanied by small increase of enthalpy by 2 kJ/mol (–550.2 kJ/mol).

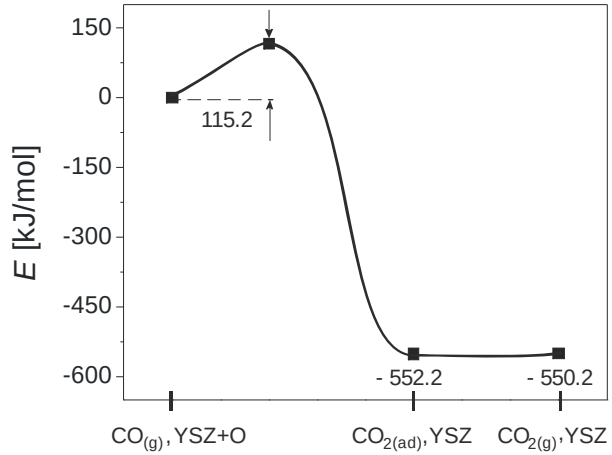

Figure 5.5: The energetics of the CO oxidation reaction on O4 oxygen atom.

Our findings indicate that CO oxidation on a YSZ+O surface is a highly exothermic process which occurs with different activation energies depending on the surface oxygen atom involved. Desorption of the CO_2 molecule into gas phase, in all cases, does not take place with an activation barrier but only with a slight increase in enthalpy.

The obtained results of CO oxidation over YSZ+O surface is in reasonable agreement with the one reported by Shishkin et al. [95]. They showed that CO oxidation on the YSZ+O surface is very favorable with substantial energy decrease by –489.1 kJ/mol. However, Shishkin et al. did not distinguish between oxygen surface atoms on YSZ+O surface and they did not comment on activation barrier of CO_2 formation.

In contrast to YSZ+O, the oxidation of CO on YSZ surface where one oxygen atom is removed (Fig. 5.1 b)) was not observed. Only physisorption of carbon monoxide was identified on YSZ surface. On the oxygen atoms within YSZ surface, the adsorption of carbon monoxide is an endothermic process with the enthalpy of +9.7 kJ/mol (O1 and O2 oxygen atoms), +26.7 kJ/mol (O3 oxygen atom) and +17.4 kJ/mol (O4 oxygen atom). Also, the possibility of CO adsorption on metals (Y, Zr) was investigated. Here, CO adsorbs exothermically with decrease in enthalpy by –32.6 kJ/mol when the molecule is bonded to an yttrium atom and by –20 kJ/mol when adsorbed on zirconium atom.

5.3 DFT calculation of H_2 oxidation over YSZ

Further DFT calculations were performed on hydrogen oxidation over the YSZ+O and YSZ surfaces. The sequence of the reactions of H_2 oxidation on the YSZ+O surface can be described as following

$$H_2 + O_{YSZ} + O_{YSZ} \rightleftharpoons HO_{YSZ} + HO_{YSZ} \quad ,$$

$$HO_{YSZ} + HO_{YSZ} \rightleftharpoons H_2O_{YSZ} + O_{YSZ} \quad , \qquad (5.2)$$

$$H_2O_{YSZ} \rightleftharpoons H_2O_{gas} + \square_{YSZ} \quad .$$

The H_2 oxidation on the YSZ+O surface leads to direct formation of gaseous H_2O and YSZ via the formation of OH surface intermediates, which can further react to yield surface H_2O that finally desorbs into the gas phase leaving back the YSZ surface. As described above, there are four oxygen atoms where reactions can occur. In Fig. 5.6, two low-energy reaction pathways for the heterogeneous H_2 oxidation reaction on the YSZ+O surface, as obtained in the DFT calculations, are schematically depicted. Both, the pathway shown in the upper part (I) and the pathway shown in the lower part (II) of Fig. 5.6 lead to direct formation of gaseous H_2O and YSZ by barrier less dissociative adsorption of H_2 on surface oxygen atoms via the formation of OH surface intermediates. These intermediates can further react to yield surface H_2O that finally desorbs into the gas phase leaving back an YSZ surface.

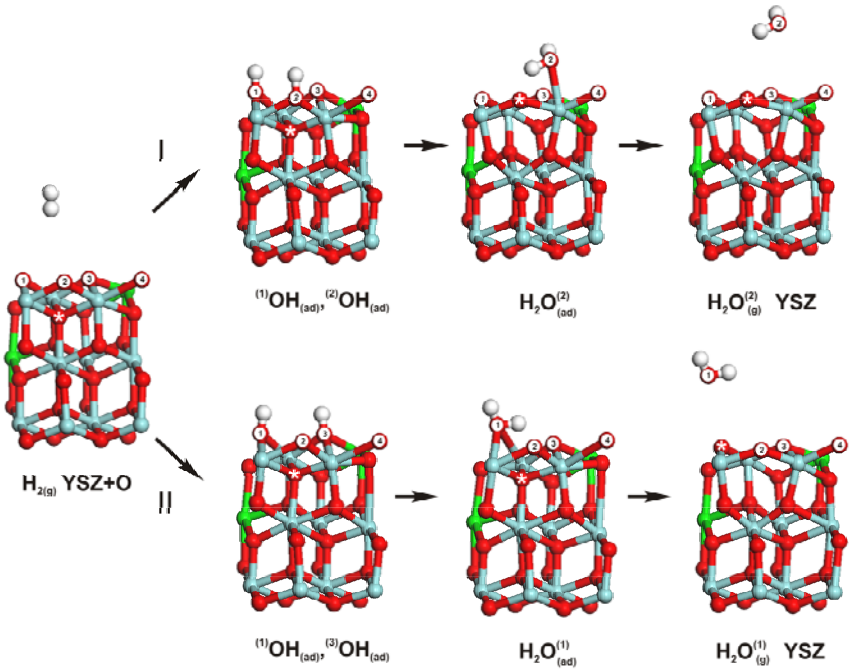

Figure 5.6: Illustration of two energy surface reaction pathways I and II, as obtained in the present DFT studies of the heterogeneous H_2 oxidation reaction on the YSZ+O surface. Numbering of the oxygen surface atoms initially present at the YSZ+O surface is the same as in Fig. 5.1 a).

The energetics of the two reaction pathways I and II illustrated in Fig. 5.6 is depicted in Fig. 5.7 a) and b), respectively. In the case of hydrogen adsorption on O1 and O2 oxygen atoms (Fig. 5.6 I), the enthalpy decreases by –514.4 kJ/mol which is slightly higher than for H_2 adsorption on O1, O3 oxygen atoms. The water molecule on the YSZ+O surface can be formed as the hydrogen of one OH group migrates toward the oxygen of the other OH group, forming H_2O. The activation energy of water formation for both cases is relatively significant and reaches values of 173.6 kJ/mol (pathway I) and 115.6 kJ/mol (pathway II). However, water desorption from YSZ+O surface is followed by completely different ways in both cases. In the case of H_2O desorption by taking the O2 oxygen atom, there is no activation energy, only an enthalpy increase by +41.7 kJ/mol. In contrast, H_2O desorption, following the reaction pathway depicted in Fig. 5.6 II, occurs with activation energy of 24.9 kJ/mol.

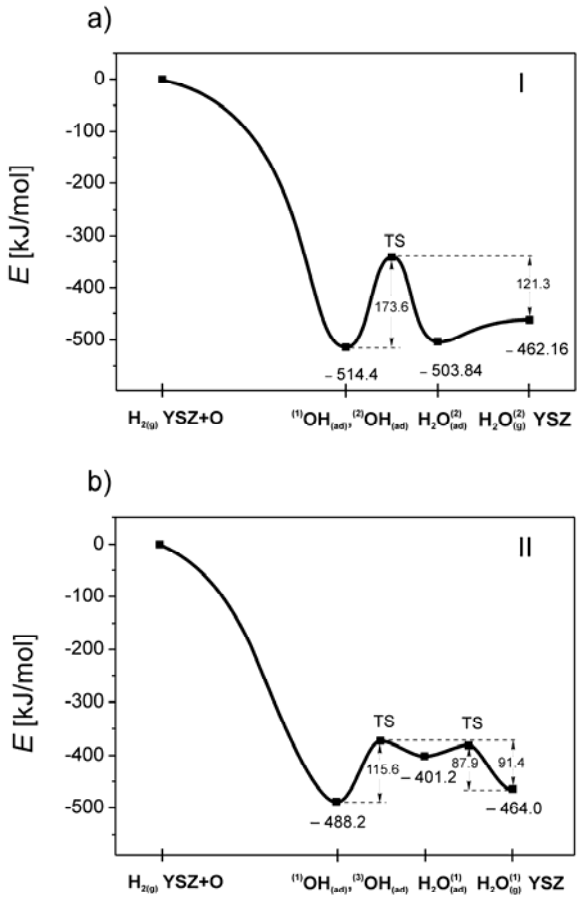

Figure 5.7: Energetic pathways for the two surface reactions illustrated in Fig. 5.6. The energy pathway depicted in a) corresponds to the reaction sequence I in Fig. 5.6. The energy pathway reproduced in b) corresponds to the reaction sequence II of Fig. 5.6.

The latter results also reveal that the reverse reaction, namely the dissociative adsorption of H_2O on YSZ leading to surface OH is an activated process with overall activation energies of E_a(I) =

121.3 kJ/mol and E_a(II) = 91.4 kJ/mol. The latter value is in reasonable agreement with the value of 86.8 kJ/mol used by Goodwin et al. [6] to describe the overall process of dissociative H_2O chemisorption.
Also, we performed DFT calculations to investigate the adsorption of H_2 on the YSZ surface. For this reaction system, however, we were unable to locate any low energy dissociative adsorption pathway resulting in surface OH formation without applying artificial constrains. Our unconstrained DFT calculations showed that the dissociative adsorption of H_2 on YSZ requires an activation energy of at least 200 kJ/mol. Hence we conclude, in mutual agreement with the DFT results reported in Ref. [95], that in contrast to the interaction of H_2 with an YSZ+O surface, the formation of OH surface species as well as any subsequent formation of water, is energetically highly unfavorable in the case of YSZ.

5.4 Conclusions

The present DFT results of CO and H_2 interaction with YSZ and YSZ+O model surfaces demonstrate the important role of the chemical state of the electrolyte surface (oxygen poor versus oxygen rich). In agreement with previous DFT studies [95], the present results emphasize the influence of the additional oxygen atom – supplied either by dissociative adsorption of gaseous O_2 or via bulk oxygen atoms – on the surface reactivity. Under conditions where external oxygen supply maintains the surface in an oxygen rich (YSZ+O) state, fuels can easily get oxidized. In the case of CO oxidation this leads to direct CO_2 formation via ER reaction type, and in the case of H_2, the surface get hydroxylated with the direct formation of H_2O. Under surface oxygen depleting operating conditions, the resulting YSZ surface is virtually inert toward CO and H_2 oxidation. Hence, it seems not unreasonable to anticipate that the electrode polarization (anodic versus cathodic) could have a pronounced influence on the actual surface reactivity of the electrolyte.

6. Results of Experimental and Simulated TPD/TPR Spectra

Temperature-programmed desorption (TPD), and reaction (TPR) measurements and simulations were performed in order to determine adsorption/desorption and surface reactions kinetic data as well as thermodynamic parameters for the $CO/CO_2/Ni$, $CO/CO_2/YSZ$ and $H_2/H_2O/YSZ$ heterogeneous reaction systems. The methodology of TPD/TPR spectra simulation is described, in subchapter (6.1). The results of TPD/TPR measurements along with simulations on Ni(111) surface is given in second subchapter (6.2). The investigation of adsorption/desorption and surface decomposition reactions on YSZ surface is described in section 6.3. The conclusions of the present TPD/TPR measurements and simulations are presented in last subchapter (6.4).

6.1 Methodology of TPD/TPR simulation

Numerical simulations of TPD spectra were carried out using the DETCHEM software package [69], which allows the calculation of temperature- and time-dependent surface coverages and surface species fluxes in the framework of a zero-dimensional surface reaction model employing thermodynamically consistent reversible elementary reaction kinetics.

In the model approach, it is assumed that the adsorbed species are randomly distributed on the surface and one can average them over local inhomogenities. Then a rate law of the heterogeneous reactions can be written similarly to the usual gas phase kinetics

$$\dot{s}_i^{\mathrm{A}} = \sum_{k \in R_{\mathrm{s}}} \nu_{\mathrm{ik}} k_{\mathrm{fk}} \prod_{j \in S} c_j^{\nu'_{\mathrm{jk}}}, \tag{6.1}$$

where, ν is stoichiometric coefficients, c_j is species concentration. The rate constant k_{fk} is calculated by the following equation

$$k_{\mathrm{fk}} = A_{\mathrm{k}} T^{\beta} \exp\left(-\frac{E_{\mathrm{act}}}{RT}\right) f_{\mathrm{k}}\left(\{\theta_i\}\right), \tag{6.2}$$

here, $f_k\left(\{\Theta_i\}\right)$ term is described by an Arrhenius-like expression which takes into account the coverage dependency of the rate constant according to

$$f_{\mathrm{k}}\left(\{\theta_i\}\right) = \prod_{i \in S} \theta_i^{\mu_{\mathrm{ik}}} \exp\left(\frac{\varepsilon_{\mathrm{ik}} \theta_i}{RT}\right), \tag{6.3}$$

with θ_i coverage of species i.

The coverage of adsorbed species varies on the surface and is given by

$$\theta_i = \frac{c_i \sigma_i}{\Gamma_{\mathrm{k}}}, \tag{6.4}$$

where, Γ_{k} – surface sites density. For adsorption reactions the sticking coefficients are commonly used. They are converted to conventional rate coefficients by

$$k_{\mathrm{f}} = \frac{s_i^0}{\Gamma_{\mathrm{k}}} \sqrt{\frac{RT}{2\pi M_{\mathrm{i}}}}, \tag{6.5}$$

with s_i^0 the initial sticking coefficient.

6.2 TPD/TPR on Ni(111) sample

6.2.1 CO adsorbate structure on Ni(111) surface.

Carbon monoxide adsorption on the Ni(111) close packed surface is among the most fully investigated adsorption system. Table 6.1 gives an overview of observed ordered structures throughout the literature. The types of adsorption strongly depend on CO coverage. Different structure types were extracted for CO on Ni(111) surface using PED (photo-electron diffraction), LEED (low-energy electron diffraction), STM (scanning tunneling microscopy), SEXAFS (surface-extended X-ray absorption fine structure) and XPS (X-ray photon emission spectroscopy) methods.

Table 6.1: Structure formed by CO on Ni(111) surface

Θ	Pattern	Structure	Method	Reference
0.25	p(2x2)	65% hcp, 35% fcc	PED, LEED	[98]
0.33	p($\sqrt{3}$ x $\sqrt{3}$)	Bridge	PED	[99]
0.50	c(2x4)	hcp, fcc	LEED, PED, STM, SEXAFS	[99-101], [102], [103]
0.57	p($\sqrt{7}$ x $\sqrt{7}$)	top, bridge	LEED, PED, STM	[100]

Note: hcp, fcc CO molecule is adsorbed on three fold hollow sites; bridge - CO molecule is adsorbed on bridge position, top - CO molecule is adsorbed on top position.

The types of CO adsorption can be divided into 4 groups. The first group corresponds to adsorption when the coverage of carbon monoxide does not exceed 0.25, where CO occupies mainly fcc and hcp sites. Davis et al. [98] used the PED and LEED methods to show that CO molecules form a p(2x2) structure and occupy the same two (hcp and fcc) inequivalent hollow sites. Also, their results indicate a preference for the hcp hollow site directly above a second-layer Ni. This preference of hcp is 65 ± 20 %. In the second region between 0.25 and 0.4, CO

bridge adsorption type is preferable. Kevan et al. [99] showed for the first time that normal photoelectron diffraction can yield definitive structure determination in molecular adsorption systems. The results obtained by these authors indicate that CO with a coverage of about 0.33 occupy the twofold bridge site in p($\sqrt{3}$ x $\sqrt{3}$) package. The next adsorption type occurs when the CO coverage is near 0.5 with fcc and hcp sites preferred. This is the most investigated system of CO adsorbate structure on Ni(111) surface. Becker et al.[103] using SEXAFS, Davila et al. [101] and Davis et al. [98] using PED, Mapeldoram et al. [104] using LEED, and Held et al. [100] using XPS showed that CO at a coverage of 0.5 formed a c(2x4) structure, where CO was adsorbed on threefold hcp and fcc hollow sites. In the last region ($\theta_{CO} > 0.55$), the p($\sqrt{7}$ x $\sqrt{7}$) structure with on top and bridge site is formed [100]. Also, it was reported by Held et al. [100] that at higher CO coverage ($\theta_{CO} \approx 0.62$) the compressed c(2$\sqrt{3}$ x 4) rect structure with occupied top and bridge sites is observed.

In the present work, TPD spectra of CO desorption from Ni(111) surface was investigated along with LEED measurements in order to determine adsorbate structure. The Ni sample was exposed to a CO pressure of 10^{-8} mbar at room temperature. The LEED pattern depicted in Fig. 6.1 a) was observed. The same LEED pattern has been observed in previous CO adsorption studies (see Fig. 1 in Ref.[105] and Ref.[106], respectively). In Ref.[106], the LEED diffraction spots (as schematically shown in Fig. 6.1 b) were attributed to three domain orientations rotated by 120° with respect to each other. In the latter studies, continuous change of the angle α (Fig. 6.1 b)) with coverage θ was observed, with a maximum value of 24° being reached at room temperature saturation coverage. From the maximum splitting observed in the LEED pattern a value of θ_{CO} = 0.53 (one monolayer, θ = 1 equals the number of Ni atoms in the (111) surface plane) was derived in Ref.[106] for the room temperature saturation coverage. In the present study, a value of $\alpha = (25 \pm 1)°$ was obtained, which indicates a similar CO equilibrium surface coverage as in Ref.[106].

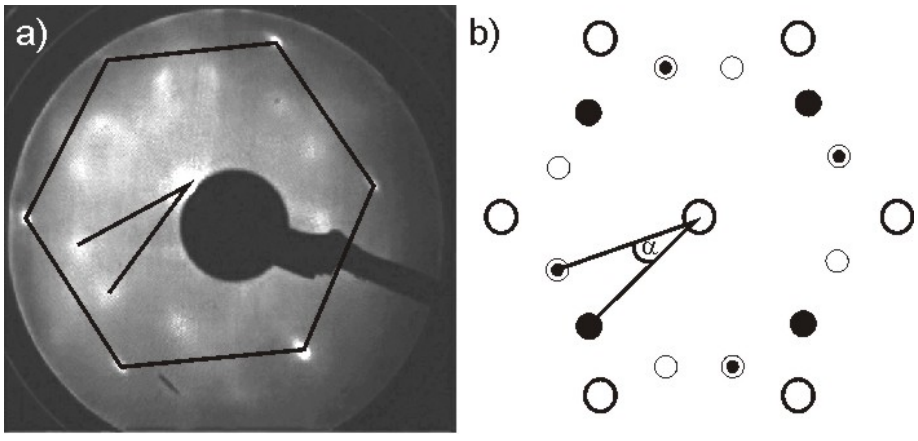

Figure 6.1: Room temperature LEED pattern for CO adsorption on Ni(111) at a CO pressure of 10^{-8} mbar. a) Photograph of the observed pattern for an electron energy of 120 eV. b) Schematic sketch (see e.g. Fig. 1a of Ref. [106]) of the diffraction spots caused by a superposition of three domain rotations. Large open circles represent spots from the substrate lattice. Small circles originate from the CO adsorbate layer.

Also, the cleanliness of the Ni and YSZ surfaces was checked by Auger electron spectroscopy. Each sample was investigated before and after the TPD/TPR measurements. The carbon formation, segregation of impurities etc., were not detected neither on Ni nor on YSZ surface.

6.2.2 Experimental and simulated CO TPD/TPR spectra on Ni(111) surface.

We have first studied the interaction of CO with the individual Ni surface. Fig. 6.2 shows results of CO TPD measurements, which were performed at three different heating rates of 2.5 K/s, 5 K/s and 7 K/s (open symbols) along with the results of the respective numerical simulations (solid lines). For the simulations, an initial CO surface sticking coefficient of $s^0_{CO} = 0.5$ was used [107]. The experimental data show a desorption peak at a temperature of ca. 400 K. The peak has a distinct shoulder towards lower temperature. In order to reproduce this behavior with the numerical simulation, two distinct CO(I) and CO(II) surfaces species were assumed to be present on the Ni surface. It will be explained below that these two species can be identified as adsorption on hcp (hexagonal closed packed) and fcc (face centered cubic) sites, respectively. For each species, a linear coverage dependency of the activation energy for desorption on coverage was included to account for the experimentally observed decrease of the CO heat of adsorption in the coverage range $0 < \theta_{CO} < 0.6$ [106, 108]. Best agreement between measured and simulated TPD spectra was achieved using the expressions $E^{act}_{des,CO(I)}(\theta_{CO}) = 111.2$ kJ/mol $- (50\ \text{kJ/mol} \times \theta_{CO})$ and $E^{act}_{des,CO(II)}(\theta_{CO}) = 102.1$ kJ/mol $-(70\ \text{kJ/mol} \times \theta_{CO})$ for the two CO surfaces species along with a common temperature-independent pre-exponential factor of $7.0 \cdot 10^{11}\ s^{-1}$.

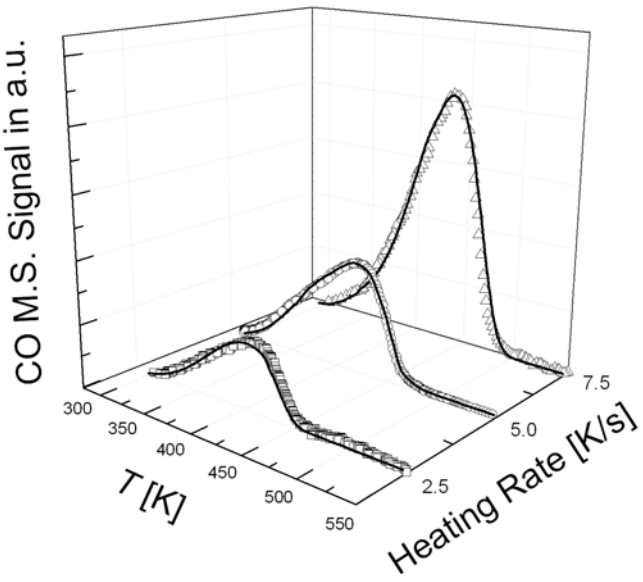

Figure 6.2: Comparison between simulated (solid lines) and experimental (open symbols) TPD spectra for CO chemisorbed on Ni(111) recorded with different heating rates.

Fig. 6.3 shows the simulated surface coverages of the individual CO(I) and CO(II) species as well as the total CO coverage during the TPD experiment. At room temperature, the total CO equilibrium coverage is θ_{CO} = 0.51. This value is in good agreement with the total CO equilibrium coverage value of θ_{CO} = 0.53 derived from the measured LEED pattern. The calculated distribution of CO(I) and CO(II) adsorption sites is 58 % vs. 42 %. In a photoelectron diffraction study, Davis et al. [98] identified for a total CO coverage of 0.5 ML a site distribution of 65 % and 35 % for CO molecules adsorbed at hcp and fcc hollow sites, respectively. Based on a comparison of these values, it is reasonable to identify the CO(I) and CO(II) species with CO molecules adsorbed on these two energetically inequivalent hollow adsorption sites [109].

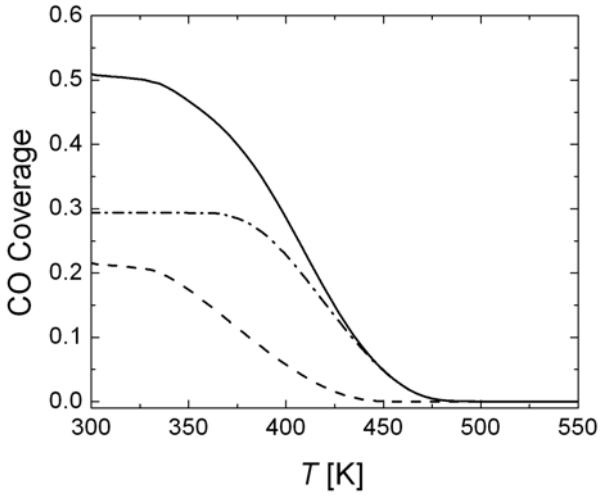

Figure 6.3: Simulation results of the temperature-dependence of the Ni(111) CO equilibrium coverage for a CO pressure of $p(CO) = 10^{-8}$ mbar. Solid line represents the total CO coverage. Dashed-dotted and dashed lines represent the fractional coverages of the CO(I) and CO(II) surface species respectively.

6.2.3 CO oxidation on Ni(111) surface.

CO oxidation on Ni(111) was studied for a CO partial pressure of $p(CO) = 10^{-6}$ mbar and an O_2 partial pressure of $p(O_2) = 10^{-6}$ mbar. TPR spectra were recorded with a heating rate of 5 K/s. Experimental results are shown in Fig. 6.4 along with the results of a numerical simulation.

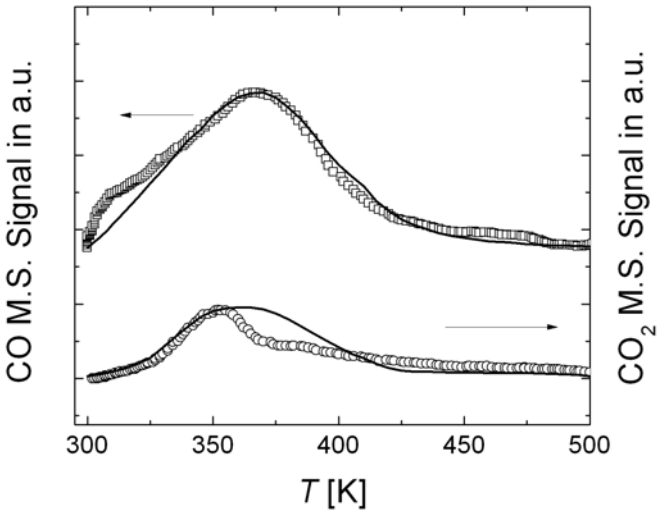

Figure 6.4: Comparison between simulated (solid lines) and experimental (open symbols) TPD and TPR spectra for CO desorption and CO_2 formation in the CO oxidation on Ni(111).

There is a good agreement between simulation and experiment. Desorption of CO occurs along with CO_2 formation. The fact that the CO_2 production decreases as the CO surface coverage decreases indicates that the CO oxidation on Ni(111) proceeds via a Langmuir-Hinshelwood (LH) surface reaction mechanism, in which both reagents, CO and oxygen (the latter being strongly adsorbed as O surface atoms after dissociative adsorption of molecular oxygen), react at the surface to form CO_2. From fitting the numerical simulation to the experimental data, a pre-exponential factor of $2.0 \cdot 10^{19}$ $cm^2/(mol\ s)$ along with an activation energy of 123.6 kJ/mol was obtained for the $CO_{Ni} + O_{Ni} \rightarrow CO_{2,Ni} + \square_{Ni}$ surface reaction step. For the subsequent CO_2 desorption step, $CO_{2,Ni} \rightarrow CO_2 + \square_{Ni}$, a pre-exponential factor of $7.0 \cdot 10^{11}$ s^{-1} and an activation energy of 41.0 kJ/mol were obtained.

6.3 TPD/TPR on YSZ sample

6.3.1 TPD/TPR investigation of CO adsorption/desorption and oxidation on YSZ surface.

CO oxidation was studied on the individual YSZ surface for a CO partial pressure of $p(CO) = 10^{-6}$ mbar and an O_2 partial pressure of $p(O_2) = 10^{-6}$ mbar. Experimental spectra were recorded with a heating rate of 5 K/s. Experimental results are shown in Fig. 6.5 together with the results of the numerical simulation.

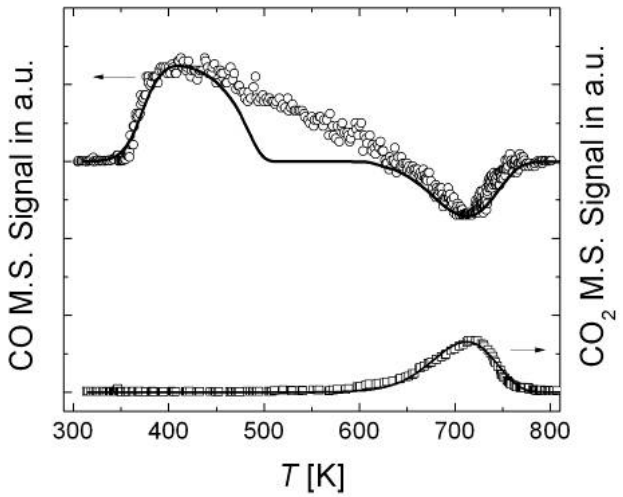

Figure 6.5: Comparison between simulated (solid lines) and experimental (open symbols) TPD and TPR spectra for CO desorption and CO_2 formation in the CO oxidation on YSZ.

The agreement between experiment and simulation is very good in case of the CO_2 TPR spectrum (lower part of Fig. 6.5). The observed deviation between experiment and simulation of the CO spectrum (upper part of Fig. 6.5) in the intermediate temperature range is most probably due to CO desorption from YSZ surface defect sites.
However, in the present simulation it was assumed that CO can absorb/desorbs on a single site only. The experiment shows that the CO_2 formation starts at a temperature of ca. 600 K. At this temperature, however, almost all CO initially adsorbed at the YSZ surface has been already desorbed. The latter fact, along with the observation of a substantial decrease of the CO gas-phase pressure at ca. 700 K (which closely follows the CO_2 formation data curve), indicates that CO oxidation over YSZ proceeds predominately via an Eley-Rideal (ER) reaction mechanism. In this mechanism, gas-phase CO directly reacts with YSZ oxygen surface atoms, O_{YSZ}, to yield gas-phase CO_2. By fitting the numerical simulations to the experiment, using value of 115.2 kJ/mol from present DFT calculation (chapter 5, Fig. 5.5), a pre-exponential factor of $1.0 \cdot 10^{22}$ $cm^2/(mol\ s)$ was derived for the $CO + O_{YSZ} \rightarrow CO_2 + \square_{YSZ}$ surface reaction step.

6.3.2 TPD/TPR investigation of H_2O interaction with YSZ.

The experimental results of water interaction with YSZ consist of three measurement series differing in the gas atmosphere the sample was exposed to. We start with the TPD measurements in H_2O followed by TPDs in pure hydrogen and finally in a mixture of H_2 and O_2.
During the recording of H_2O TPD spectra, it was found that desorption from the sample holder contributes to the actual water desorption TPD curve from YSZ sample forming a background signal. With the purpose of subtracting the influence of background on TPD curve, a background subtraction procedure was applied. In Fig. 6.6 a), a typical raw experimental TPD spectrum is shown. In order to obtain a TPD spectrum representing the actual desorption of H_2O from the YSZ sample, the H_2O signal background was measured (see Fig. 6.6 b)). The actual H_2O TPD spectrum, after the subtraction of the background from raw spectrum, is shown in Fig. 6.6 c). All

TPD spectra shown in the following figure were obtained by applying this background correction procedure.

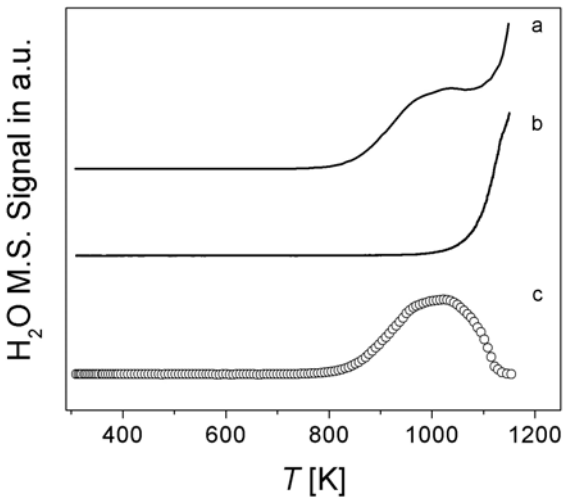

Figure 6.6: Background correction procedure. a: Raw H_2O TPD spectrum, b: Background contribution from the sample holder, c: Background subtracted TPD spectrum representing H_2O desorbing from the YSZ sample. The TPD spectra are shifted vertically against each other for clarity

A time series of H_2O TPD spectra obtained for an YSZ sample exposed to ambient air humidity ($p(H_2O)$ = 24 mbar) prior to the measurements is depicted in Fig. 6.7. The three consecutively recorded spectra (curves a, b, c) revealed the decreasing amount of desorbing H_2O molecules as manifested by curve c, which was obtained in run three, where practically no H_2O desorption signal could be observed anymore. The experimental data (Fig. 6.7 a), b)) show a desorption peak at a temperature of about 1020 K. The peak has a distinct shoulder towards lower temperature.

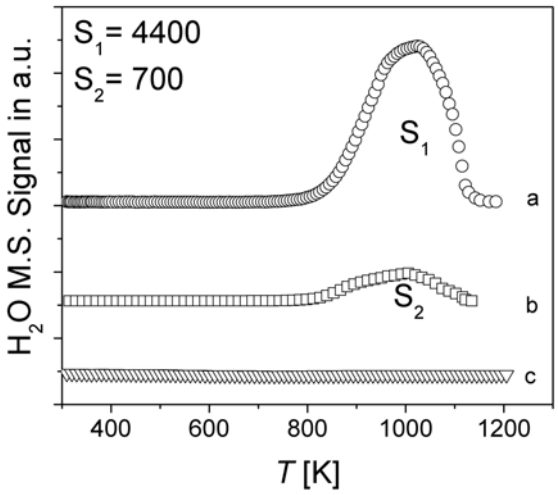

Figure 6.7: Time series of H_2O TPD spectra. a: First spectrum of an YSZ sample exposed to ambient air humidity prior to the TPD measurement, b: Second spectrum recorded right after spectrum a, c: Third spectrum recorded right after spectrum b.

The H_2O coverage on the YSZ sample can be estimated by comparing the sum of the integrated areas of the two TPD spectra (Fig. 6.7 a) and b)) with the integrated area of a CO TPD spectrum obtained from a Pt(111) [110]. In Ref. [110], Pt(111) surface was exposed to a CO partial pressure of 10^{-8} mbar until a sharp c(4×2)Pt(111)-CO LEED pattern corresponding to a CO coverage of 0.5 monolayer was observed. The calculation leads to the H_2O coverage of about 600. This is not realistic value for the H_2O coverage on YSZ surface and it is reasonably to assume that H_2O dissolved in the bulk of YSZ. In the basis of this assumption a value of $x(H_2O_i) = 6 \cdot 10^{-5}$ was estimated for the mole fraction of H_2O solved in YSZ. In the latter estimate, the different electron impact ionization cross sections of CO (to CO^+ [111]) and H_2O (to H_2O^+ [112]) were taken into account. Platinum surface atom density of 15×10^{14} atoms cm^{-2} was used along with a YSZ bulk density value of 6.1 g/cm^3. Assuming that the solution of H_2O in YSZ leads to the formation of two interstitial protons (hydrogen, H_i) this value corresponds to a value of $x(H_i) = 12 \cdot 10^{-5}$ for the mole fraction of solute protons. The latter value is approximately five times higher than the value of $x(H_i) = 2.2 \cdot 10^{-5}$ obtained by Wagner [113] for YSZ (10% mol Y_2O_3) at comparable H_2O partial pressure of 24 mbar.

Following the third measurements Fig. 6.7 c) when no water remains in YSZ sample, the re-adsorption of H_2O was investigated. The subsequent TPD spectrum of H_2O desorption, when the YSZ sample was exposed to water pressure of $1 \cdot 10^{-6}$ mbar for 25 min (corresponding to an exposure of 1100 Langmuir), is shown in Fig. 6.8. Applying the same procedure, described above, the amount of H_2O dissolved in YSZ sample was estimated. The integrated area of H_2O desorption (see Fig. 6.8) is 1770 which correspond to a mole fraction of $x(H_2O_i) = 2.1 \cdot 10^{-5}$ of water in YSZ. The latter value gives a value of $4.2 \cdot 10^{-5}$ of interstitial protons in YSZ sample.

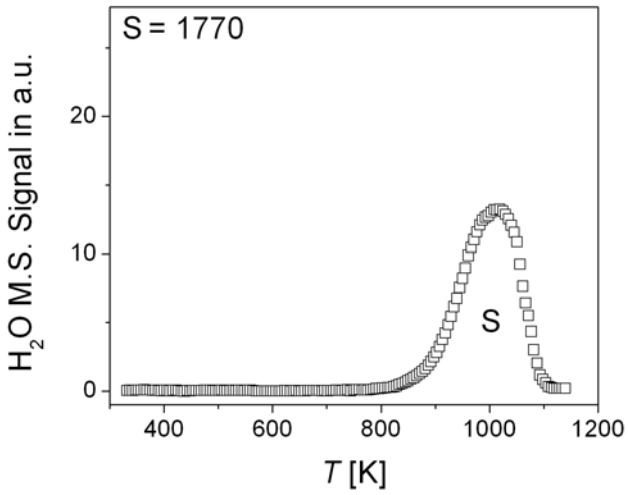

Figure 6.8: TPD spectrum of H_2O desorption from YSZ after exposing the sample to a H_2O at $p(H_2O) = 1 \cdot 10^{-6}$ mbar for 25 minutes.

The third type of measurement was performed in a pure H_2 atmosphere with $p(H_2) = 1 \cdot 10^{-6}$ mbar. The YSZ sample was cleaned up following the procedure described in Fig. 6.7, after which the sample was exposed to H_2 prior to TPD measurements. The H_2O TPD spectrum obtained after exposing the YSZ sample to H_2 is shown in Fig. 6.9 a). The corresponding TPD spectrum of hydrogen, corresponding to the of H_2O spectrum shown in Fig. 6.9 a), was measured and is shown in Fig. 6.9 b).

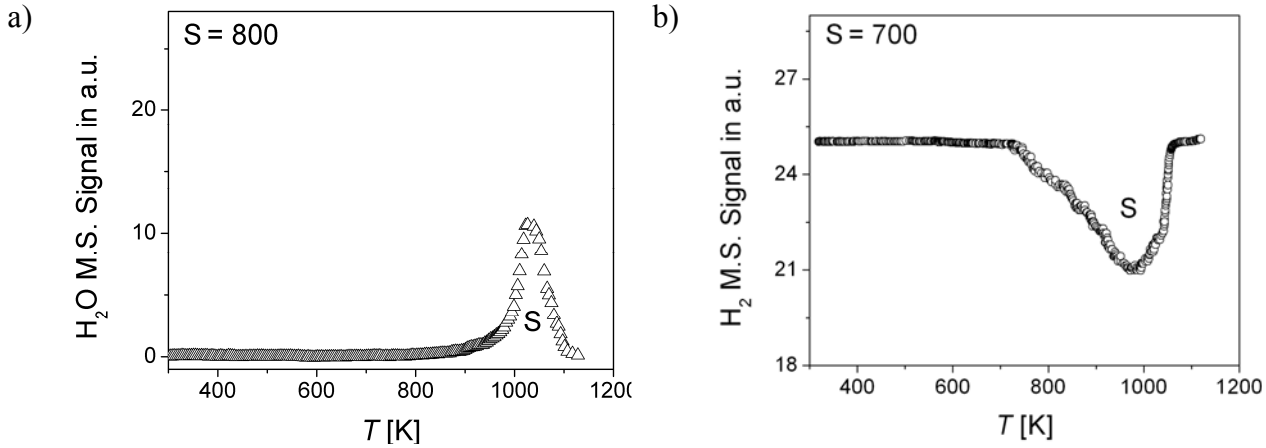

Figure 6.9: a) TPD spectrum of H_2O desorption from YSZ after exposing the sample to a H_2 at $p(H_2) = 1 \cdot 10^{-6}$ mbar for 25 minutes. b) TPD spectrum of H_2 on YSZ during the recording of H_2O TPD curve.

Following the calculation of water content in YSZ, described above, the amount of H_2O desorbing from the sample (Fig. 6.9 a)) is $x(H_2O_i) = 0.9 \cdot 10^{-5}$ which correspond to $1.8 \cdot 10^{-5}$ mol fraction of interstitial hydrogen. The amount of dissolved hydrogen in the YSZ sample calculated from the integrated area of Fig. 6.9 b) is $1.6 \cdot 10^{-5}$. The similarity of interstitial hydrogen amount in both cases ($1.8 \cdot 10^{-5}$ and $1.6 \cdot 10^{-5}$) indicates that hydrogen adsorption on an oxygen-poor YSZ sample is an activated process which starts at about 700 K (Fig. 6.9 b)). This

observation is in good agreement with the present DFT calculations (see chapter 5, paragraph 5.3) which showed that hydrogen interaction with oxygen poor YSZ surface is not favourable and occurs with a large barrier.
In the last set of experiments, the YSZ sample was exposed to a H_2/O_2 mixture ($p(H_2) = p(O_2) = 1 \cdot 10^{-6}$ mbar) for 25 minutes prior to TPD spectra measurements. The TPD spectrum of H_2O desorption after the interaction of hydrogen/oxygen gasses with YSZ sample is shown in Fig. 6.10 a). Also, the corresponding H_2 and O_2 TPD spectra (Fig. 6.10 b)) were recorded.

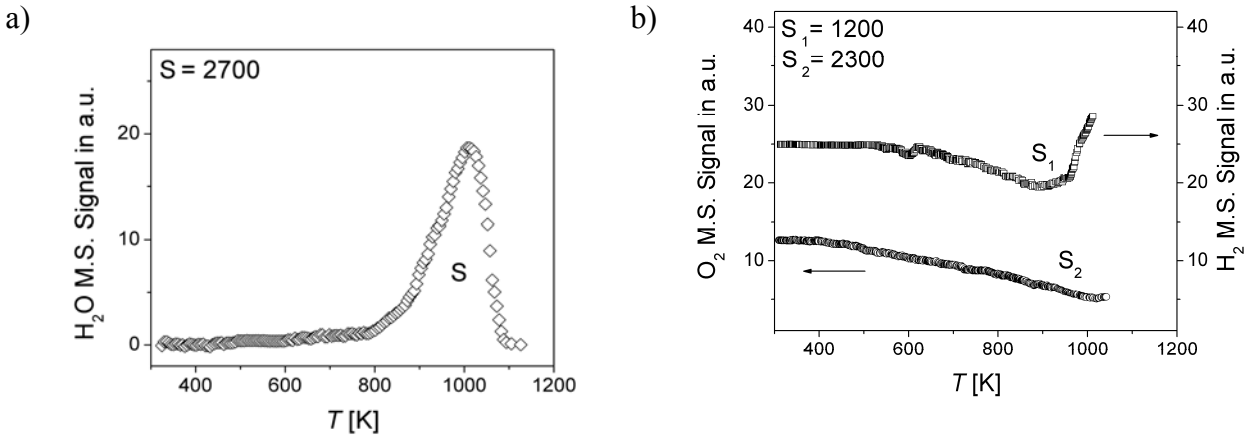

Figure 6.10: a) TPD spectrum of H_2O desorption from YSZ after exposing the sample to H_2/O_2 at $p(H_2) = p(O_2) = 1 \cdot 10^{-6}$ mbar for 25 minutes. b) TPD spectrum of H_2/O_2 on YSZ during the recording of H_2O TPD curve.

The applied calibration experiments revealed that YSZ exposure to a H_2/O_2 atmosphere also leads to a considerable amount of YSZ bulk H_2O formation resulting in values of $x(H_2O_i) = 3.2 \cdot 10^{-5}$ and $x(H_i) = 6.4 \cdot 10^{-5}$ which are only a factor of two lower than the values obtained in the present water adsorption studies (Fig. 6.7). It indicates that in an oxygen-rich YSZ sample hydrogen can easily be dissolved, which is in good agreement with the present DFT calculations. The amount of interstitial hydrogen which was dissolved in YSZ during H_2O curve measurements (Fig. 6.10 a)) was calculated based on integrated area analysis of H_2 curve (Fig. 6.10 b)) and reach a value of $2.8 \cdot 10^{-5}$. This value is about 2.5 times lower than amount of interstitial hydrogen calculated from water desorption curve (Fig. 6.10 a)) which indicates that in the presence of oxygen, hydrogen can dissociate on an oxygen-rich YSZ surface at low temperature.

Simulations of experimental TPD/TPR spectra of water interaction with YSZ, described above, were performed based on the present DFT calculations (see chapter 5, paragraph 5.3). As mentioned at the beginning of this chapter, the numerical simulations of TPD spectra were carried out using the DETCHEM software package [69].
The adsorption/desorption and surface reaction kinetics data, summarized in Table 6.2 and Table 6.3, was obtained in the present work by systematically adjusting the respective pre-exponential factors (k^0) in the TPD simulation until best agreement with the experimental TPD

spectra was achieved. The schematic illustration of the assumed reaction pathway of hydrogen oxidation is given in Fig. 5.6 (pathway I) and Fig. 5.7 a) (energetics).

Table 6.2: Summary of the reaction kinetics parameters of H_2 oxidation on YSZ+O. YSZ+O surface site density is $1.3 \cdot 10^{-9}$ mol/cm^2. k^0 – pre-exponential factor, $s_0^{(*)}$ – sticking coefficient.

№	Reaction	$k^0/s_0^{(*)}$	E_i^{act} (kJ/mol)
1	$H_{2(g)} + 2\,\square_{YSZ} \rightarrow {}^{(1)}OH_{(ad)} + {}^{(2)}OH_{(ad)}$	$1.2 \cdot 10^{-2(*)}$	0
2	${}^{(1)}OH_{(ad)} + {}^{(2)}OH_{(ad)} \rightarrow H_{2(g)} + 2\square_{YSZ}$	$1.1 \cdot 10^{10}$ cm^2/(mol s)	514.4
3	${}^{(1)}OH_{(ad)} + {}^{(2)}OH_{(ad)} \rightarrow H_2O^{(2)}_{(ad)} + {}^{(1)}O_{(ad)}$	$1.1 \cdot 10^{17}$ cm^2/(mol s)	173.6
4	$H_2O^{(2)}_{(ad)} + {}^{(1)}O_{(ad)} \rightarrow {}^{(1)}OH_{(ad)} + {}^{(2)}OH_{(ad)}$	$1.6 \cdot 10^{25}$ cm^2/(mol s)	164
5	$H_2O^{(2)}_{(ad)} \rightarrow H_2O_{(g)} + \square_{YSZ}$	$8.5 \cdot 10^{13}$ cm^2/(mol s)	41.7
6	$H_2O_{(g)} + \square_{YSZ} \rightarrow H_2O^{(2)}_{(ad)}$	$1.2 \cdot 10^{-4(*)}$	0

The Arrhenius activation energies E_i^{act}, used in Table 6.3 are taken from Fig 5.7 b) with corresponding energy surface reaction pathways II showed in Fig. 5.6.

Table 6.3: Summary of the reaction kinetics parameters of H_2 oxidation on YSZ+O. YSZ+O surface site density is $1.3 \cdot 10^{-9}$ mol/cm^2. k^0 – pre-exponential factor, $s_0^{(*)}$ – sticking coefficient.

№	Reaction	$k^0/s_0^{(*)}$	E_i^{act} (kJ/mol)
1	$H_{2(g)} + 2\,\square_{YSZ} \rightarrow {}^{(1)}OH_{(ad)} + {}^{(3)}OH_{(ad)}$	$1.2 \cdot 10^{-2(*)}$	0
2	${}^{(1)}OH_{(ad)} + {}^{(3)}OH_{(ad)} \rightarrow H_{2(g)} + 2\square_{YSZ}$	$1.1 \cdot 10^{10}$ cm^2/(mol s)	488.2
3	${}^{(1)}OH_{(ad)} + {}^{(3)}OH_{(ad)} \rightarrow H_2O^{(1)}_{(ad)} + {}^{(3)}O_{(ad)}$	$1.1 \cdot 10^{14}$ cm^2/(mol s)	115.6
4	$H_2O^{(1)}_{(ad)} + {}^{(3)}O_{(ad)} \rightarrow {}^{(1)}OH_{(ad)} + {}^{(3)}OH_{(ad)}$	$5.6 \cdot 10^{20}$ cm^2/(mol s)	28.6
5	$H_2O^{(1)}_{(ad)} \rightarrow H_2O_{(g)} + \square_{YSZ}$	$8.5 \cdot 10^{14}$ cm^2/(mol s)	25.1
6	$H_2O_{(g)} + \square_{YSZ} \rightarrow H_2O^{(1)}_{(ad)}$	$1.2 \cdot 10^{-4(*)}$	87.9

Fig. 6.11 shows the results of the numerical simulations obtained for the two different H_2 oxidation mechanisms with corresponding experimental data (open symbols) of H_2/O_2 and H_2O interaction with YSZ surface. The comparison of experimental TPD curve of water desorption after the sample was exposed to H_2/O_2 mixture, simulated based on mechanism from Table 6.2 (solid line) and Table 6.3 (dashed line), is shown in Fig. 6.11 a). In Fig. 6.11 b), the comparison between simulations, simulated using the mechanisms from Table 6.2 and Table 6.3, and experimental water TPD spectrum, obtained after YSZ was exposed to H_2O, is given. All simulations represent best fits of the reaction pre-exponential factors (k^0) for each individual mechanism. The comparison between the experiments and the simulations show that both mechanisms are able to describe the experimental data in a reasonable way over the complete range of temperature with only small differences. However, this comparison indicates that best agreement between modeling and experiment is obtained by means of the mechanism shown in Table 6.2.

As already mentioned in chapter 5 (DFT calculations on YSZ) the mechanisms of H_2 oxidation shown in Table 6.2 and Table 6.3 are energetically the most favorable pathways taking place on YSZ surface. For this reason these pathways were chosen in order to simulate experimentally measured H_2O TPD spectra.

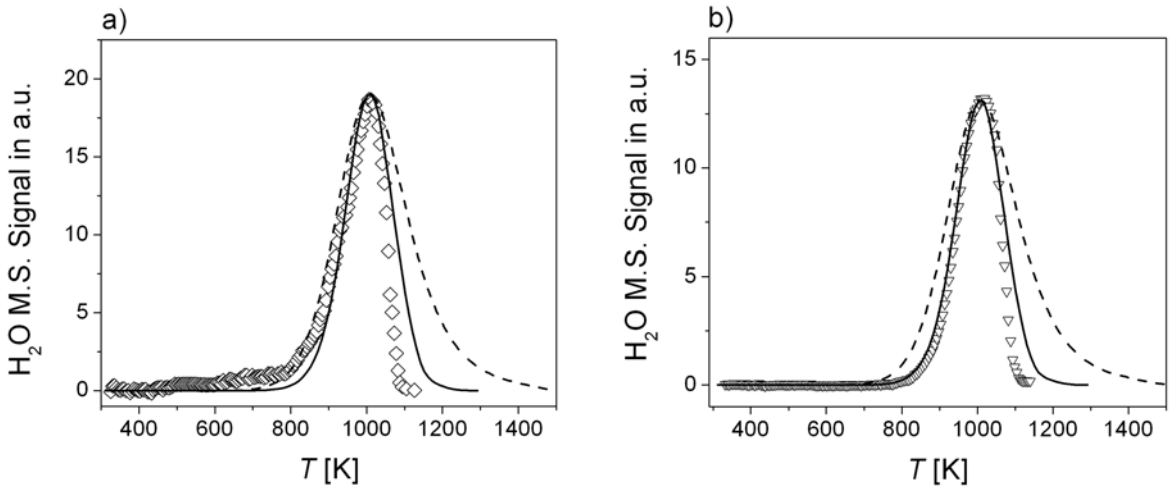

Figure 6.11: Comparison of H_2O TPD spectra obtained from numerical simulations based on reaction mechanisms described in Table 6.2 (solid line) and Table 6.3 (dashed line) and experimental H_2O spectrum (open symbols) obtained for (a) H_2/O_2 atmosphere ($p(H_2) = p(O_2) = 1 \cdot 10^{-6}$ mbar), (b) H_2O atmosphere ($p(H_2O) = 1 \cdot 10^{-6}$ mbar).

Fig. 6.12 shows the computed coverages of surface species for a temperature range from 300 to 1300 K during the simulation of H_2O TPD curve presented in Fig. 6.12 a) (solid line).

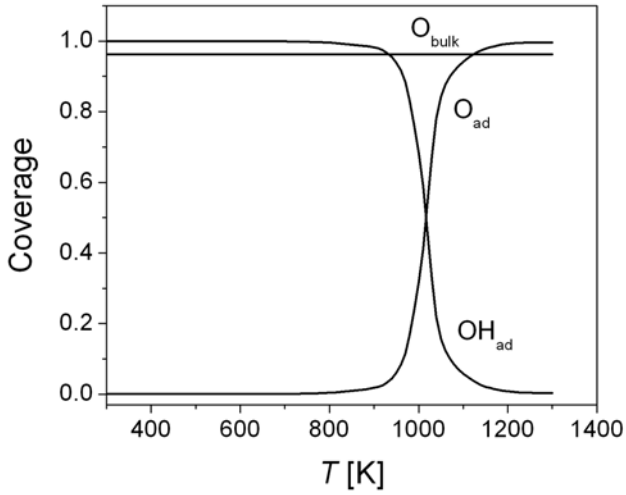

Figure 6.12: Computed surface species coverage for the simulated H_2O TPD spectrum showed in Fig. 6.10 a) solid line.

6.4 Conclusions

Using temperature-programmed desorption and reaction experiments, elementary kinetic mechanisms of CO adsorption, desorption and oxidation on the individual Ni and YSZ surfaces as well as H_2 oxidation on YSZ were developed and validated. The CO desorption spectra on the Ni(111) surface were measured and successfully simulated for different heating rates of 2.5, 5 and 7 K/s. The results of water and hydrogen interaction with YSZ indicate that H_2 dissolution in oxygen-rich YSZ is a favorable process which leads to the formation of interstitial hydrogen or hydroxyl species. The Arrhenius activation energies from present DFT calculations (chapter 5) were used to model experimental TPD/TPR spectra of CO and H_2 oxidation on YSZ surface.

7. Results of Electrochemical Simulations

Based on the experimental TPD/TPR measurements described in the previous chapter, an elementary kinetic reaction mechanism of the electrochemical CO oxidation at Ni/YSZ anodes was developed. Numerical simulations were performed for two data sets reported by Lauvstad et al. [29] and Utz et al. [33] . The simulations of steady-state polarization curves and electrochemical impedance spectra for the Ni point electrode [29] is described firstly (7.1). The experimental electrochemical results for Ni/YSZ pattern anode [33] was modeled and presented in the second subchapter (7.2). Some aspects of the charge transfer reaction in Ni/YSZ SOFC system are discussed in 7.3. At the end of this chapter, the conclusions of electrochemical simulation results will be given (7.4).

7.1 Ni, CO-CO_2|YSZ point anode

7.1.1 Simulation targets for model validation

In chapter 4, the basic principle of Ni/YSZ point anode structure and operation were described. The advantages of point electrodes are 1) the TPB length is well defined, 2) the interface between Ni and YSZ is easy to investigate after an electrochemical experiment, and 3) it is relatively easy to obtain a well defined electrode potential. However, despite the simplicity of point electrodes, the microscopic details of the electrochemical reaction mechanism of the anode, occurring at the three-phase boundary (TPB) of gas-phase, electrode, and electrolyte, are not yet fully resolved even for simple systems such as the electrochemical carbon monoxide (CO) oxidation reactions [114]. In this work we present the combination of computational studies based on detailed elementary reaction models along with electrochemical experiments in order to understand the actual interfacial electrochemistry [115].

In the present work we show the results of electrochemical simulations based on experimental measurements done by Lauvstad et al. [29]. Lauvstad et al. performed electrochemical steady-state polarization and impedance measurements employing well-defined point-shaped Ni electrodes in contact with a YSZ electrolyte exposed to various CO/CO_2 mixtures. Based on their theoretical analysis, it was concluded that the reaction involves at least two adsorbed species, which were identified as chemisorbed atomic oxygen and molecular CO [28]. Lauvstad et al. assumed a one-step charge-transfer reaction,

$$CO_{Ni} + O^{2-}_{YSZ} \rightleftharpoons CO_2 + \square_{Ni} + \square_{YSZ} + 2\,e^-_{Ni}\,, \qquad (7.1)$$

where, the subscript (Ni, YSZ) denotes the surface the species is attached to and □ stands for a free surface site. Reaction (7.1) involves the simultaneous transfer of two electrons from an oxygen anion to the Ni electrode along with gaseous CO_2 formation. From a microscopic point of view, it is unlikely that such a complex process can proceed in one single elementary step.

In this work we present results from numerical modeling studies of the electrochemical CO oxidation in which the above one-step reaction is further resolved into single-electron charge transfer followed by CO oxidation steps, occurring on the Ni and YSZ surfaces. A consistent kinetic and thermodynamic data set for CO adsorption/desorption and heterogeneous CO oxidation on both individual Ni and YSZ surfaces was derived based on TPD/TPR measurements (see chapter 6).
In order to validate the reaction mechanism and to identify the charge-transfer pathway, results of numerical simulations are compared with steady-state polarization measurements of Lauvstad et al. [28, 29]. In the Lauvstad et al. study, a well-defined model anode system consisting of a point-shaped Ni electrode in contact with YSZ electrolyte was employed, which was exposed to different $CO/CO_2/Ar$ mixtures at an operating temperature of 1149 K. The area-specific TPB length in the experiments was 220 cm/cm^2.

Results

7.1.2 Elementary kinetic reaction mechanism

Based on the results of the TPD and TPR investigations, an elementary kinetic mechanism of the electrochemical CO oxidation under SOFC operating conditions was derived. The mechanism is illustrated schematically in Fig. 7.1. It consists of three gas-phase species (CO, CO_2, O_2), four Ni surface species ($\square_{Ni}$, CO_{Ni}, $CO_{2,Ni}$, O_{Ni}), four YSZ surface species ($\square_{YSZ}$, CO_{YSZ}, O^{1-}_{YSZ}, O^{2-}_{YSZ}) and two YSZ bulk species ($O^{X}_{O\,YSZ}$ and $V^{\bullet\bullet}_{O\,YSZ}$). The molar thermodynamic data of these species is summarized in Table 7.1. The values were taken from literature or derived from a thermodynamically consistent analysis of the TPD and TPR data. Note that, unlike for the TPD simulations, only one single CO_{Ni} species is used in this mechanism. This is due to the fact that at SOFC operating temperatures the CO coverage is very small only ($\theta_{CO} \sim 10^{-2}$), so that only the most stable species is assumed to be present. For the same reason, the activation energy of the Ni desorption is assumed to be coverage independent.

Table 7.1: Molar thermodynamic data (enthalpies and entropies) for gas-phase, surface and bulk species for T =1149 K. The symbols $\square_{Ni}$ and $\square_{YSZ}$ denote a free surface site on Ni and YSZ, respectively.

Species, i	h_i (kJ/mol)	s_i (J/K mol)	Ref.
Gas			
CO	–84	238	[116]
CO_2	–353	275	[116]
O_2	26	247	[116]

Ni surface			
$\square_{Ni}$	0	0	reference specie [117]
CO_{Ni}	–197	193	this work
$CO_{2,Ni}$	–394	205	this work
O_{Ni}	–222	39	[107]
O^{1-}_{Ni}	–222	39	set to same value as O_{Ni}
YSZ surface			
$\square_{YSZ}$	0	0	reference specie [117]
CO_{YSZ}	–159	172	this work
O^{2-}_{YSZ}	–236	0	[118]
O^{1-}_{YSZ}	–236	0	set to same value as O^{2-}_{YSZ}
Bulk species			
$V^{\bullet\bullet}_{O\,YSZ}$	0	0	reference specie [117]
$O^{X}_{O\,YSZ}$	–236	0	[118]

Table 7.2 lists the elementary reactions and their rate coefficients of the CO and CO_2 adsorption/desorption, heterogeneous CO oxidation, and electrochemical charge-transfer (CT) reactions. The rate coefficients of the heterogeneous reactions were obtained from TPD and TPR experiments.

Table 7.2: Summary of the kinetic parameters for Ni and YSZ surface reactions and charge-transfer reactions. Ni and YSZ surface site densities are $6.1 \cdot 10^{-9}$ mol/cm^2 and $1.3 \cdot 10^{-9}$ mol/cm^2, respectively. Symmetry factors of the charge-transfer reaction are set to 0.5. The parameters are k^0 pre-exponential factor, s_i^0 initial sticking coefficient, k_{CT} charge transfer reaction rate constant. The symbols $\square_{Ni}$ and $\square_{YSZ}$ denote a free surface site on Ni and YSZ, respectively. The units of rate constant follow from the formulation of the rate equations as given in Ref. [117]

No.	Reaction	k^0 (or s_i^0)	E^{act} (kJ/mol)	Ref.
Ni surface reactions				
1	$CO + \square_{Ni} \rightleftharpoons CO_{Ni}$	$s_i^0 = 5.0 \cdot 10^{-1}$	0	[107]
2	$CO_{2,Ni} \rightleftharpoons CO_2 + \square_{Ni}$	$7.0 \cdot 10^{11}$ 1/s	41	TPD experiments
3	$CO + O_{Ni} \rightleftharpoons CO_2 + \square_{Ni}$	$1.0 \cdot 10^{23}$ cm^2/(mol s)	180.0	
4	$CO_{Ni} + O_{Ni} \rightleftharpoons CO_{2,Ni} + \square_{Ni}$	$2.0 \cdot 10^{19}$ cm^2/(mol s)	123.6	TPD experiments
YSZ surface reactions				
5	$CO + \square_{YSZ} \rightleftharpoons CO_{YSZ}$	$s_i^0 = 4.0 \cdot 10^{-2}$	0	TPD experiments
6	$CO + O_{YSZ} \rightleftharpoons CO_2 + \square_{YSZ}$	$1.0 \cdot 10^{20}$ cm^2/(mol s)	158.1	TPD experiments
7	$O^{2-}_{YSZ} + V^{\bullet\bullet}_{O\,YSZ} \rightleftharpoons O^{X}_{O\,YSZ} + \square_{YSZ}$	$1.6 \cdot 10^{22}$ cm^2/(mol s)	90.9	[119]
Charge-transfer reactions		k_{CT} (T = 1149 K)		
O1+O2	$O^{2-}_{YSZ} \rightleftharpoons O^{1-}_{YSZ} + e^-_{Ni}$	$8.4 \cdot 10^{-6}$ mol/(cm s)		Fit to electrochemical data
	$O^{1-}_{YSZ} + \square_{Ni} \rightleftharpoons O_{Ni} + \square_{YSZ} + e^-_{Ni}$	$7.4 \cdot 10^{-1}$ mol/(cm s)		
O3+O4	$O^{2-}_{YSZ} + \square_{Ni} \rightleftharpoons O^{1-}_{Ni} + \square_{YSZ} + e^-_{Ni}$	$5.3 \cdot 10^{-6}$ mol/(cm s)		Fit to electrochemical data
	$O^{1-}_{Ni} \rightleftharpoons O_{Ni} + e^-_{Ni}$	$2.1 \cdot 10^{-1}$ mol/(cm s)		

O5	$O^{2-}_{YSZ} + \square_{Ni} \rightleftharpoons O_{Ni} + \square_{YSZ} + 2\,e^{-}_{Ni}$	$4.9 \cdot 10^{-6}$ mol/(cm s)	Fit to electrochemical data

The surface chemistry on Ni consists of 4 reactions (in Table 7.2, numbering from 1 to 4). These are CO and CO_2 adsorption/desorption and CO oxidation following by a Langmuir-Hinshelwood type mechanism (reaction 4). The Ni surface mechanism was completed by an Eley-Rideal type reaction (reaction 3) suggested in Ref. [120] involving the reaction of gas-phase CO with adsorbed atomic oxygen to gas phase CO_2. For the YSZ surface there is no validated reaction mechanism available in literature. That is why, one of the novelty of the present approach is that we performed additional studies of CO oxidation on YSZ (which to the best of our knowledge has not yet been studied experimentally) in order to derive accurate kinetics data for the use in the subsequent CO electrooxidation simulations. This process is described by reaction 6 in Table 7.2 and it represents ER CO oxidation reaction in order to consistently reproduce the SOFC results at elevated as well as low CO partial pressures. The transport of bulk oxygen species to the YSZ surface occurs by a bulk-surface migration process via electrolyte vacancies, which in Table 7.2 is represented by reaction 7. The kinetics parameters of reaction 7 are taken from Ref.[117].

The CT reactions were assumed to take place directly at the TPB between Ni, YSZ and the gas-phase only. We have compared three different charge-transfer mechanisms based on oxygen spillover, as shown in Table 7.2, which are illustrated in Fig. 7.1 and discussed in detail in chapter 4. The first mechanism (O1+O2) consists of two consecutive single-electron CT reactions. The first reaction O1 represents a single electron oxidation step of O^{2-}_{YSZ}, followed by a second reaction O2 representing a spillover with simultaneous CT of an O^{1-}_{YSZ} to the Ni surface. The second mechanism (O3+O4) consists of a first reaction O3, where an O^{2-} anion initially adsorbed at the YSZ surface spills over to the Ni anode (thereby releasing an electron), followed by reaction O4 during which the O^{1-} anion on Ni is finally discharged. The third mechanism (O5) represents a single-step oxygen O^{2-}_{YSZ} spillover reaction, in the course of which two electrons are transferred to the Ni anode simultaneously. The rate constants were obtained by fitting of simulated Tafel plots to experimental data by Lauvstad et al. [28, 29] over a range of gas compositions. Because experimental data were available only at a single temperature of 1149 K, it was not possible to further separate the rate constants into an activation energy and a pre-exponential factor.

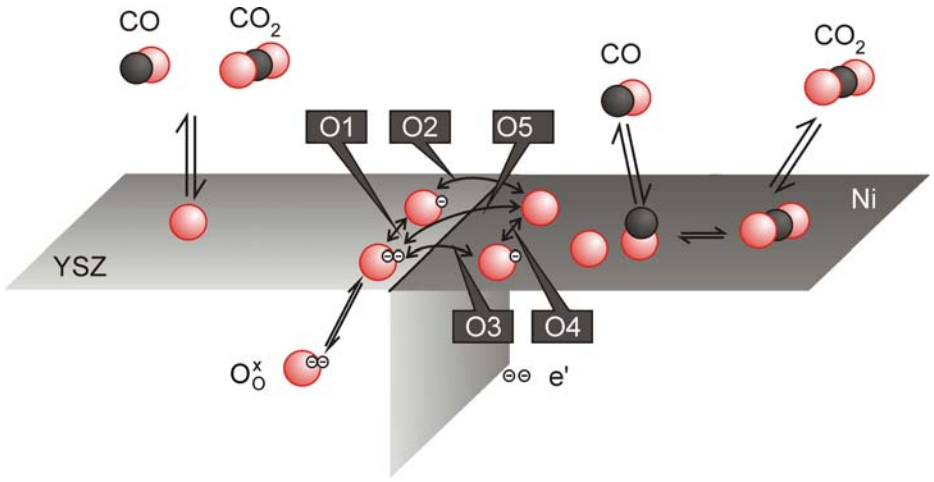

Figure 7.1: Schematic illustration of the reaction mechanism and the three different charge-transfer pathways taking place at the three-phase boundary of Ni, YSZ and gas phase (cf. Table 7.1)

The 1D reaction-diffusion model applied here includes diffusion of the CO, CO_2 and O surface species on Ni and YSZ perpendicular to the TPB. For CO and CO_2, a common diffusion coefficient of D_{Ni} (1149 K) = D_{YSZ} (1149 K) = $1.9 \cdot 10^{-7}$ cm^2/s [121] was employed. For O, diffusion coefficients of D_{Ni}(1149 K) = $1.9 \cdot 10^{-5}$ cm^2/s [122] and D_{YSZ}(1149 K) = $3.3 \cdot 10^{-8}$ cm^2/s [123] were used. Comparative simulations that were performed under the assumption of infinitely fast surface diffusion revealed that for the conditions studied here surface transport plays only a minor role in both, steady-state polarization behavior as well as impedance spectra. Pre-exponential factor and activation energy for bulk ion conductivity of the YSZ electrolyte are $k_0 = 5.5 \cdot 10^7$ S·K/m, and $E_i^{act} = 90$ kJ/mol, respectively.

Steady-state behavior

Figs. 7.2 – 7.4 show the results of the numerical simulations (solid lines) obtained for the three different CT mechanisms with corresponding experimental data (open symbols, taken from Ref. [29]). All simulations represent best fits of the reaction rate constants k_{CT} for each individual CT mechanism. The values for k_{CT} are listed in the lower part of Table 7.1. The comparison between the experiments and the simulations show that all three CT mechanisms are able to describe the experimental data in a reasonable way over the complete range of investigated gas compositions with only small differences.

In the plots marked by a) in the Figs. 7.2 – 7.4, experimental results showed as: circuits represent ratio $p(CO)/p(CO_2)$ = 333 mbar/670 mbar = 0.5; squares represent ratio $p(CO)/p(CO_2)$ = 67 mbar/670 mbar = 0.1; triangles represent ratio $p(CO)/p(CO_2)$ = 6.7 mbar/670 mbar = 0.01. In the same figures (7.2 – 7.4) in the plots marked by b) experimental data showed as: pentagons represent ratio $p(CO)/p(CO_2)$ = 0.67 mbar/6.7 mbar = 0.1; hexagons represent ratio

$p(CO)/p(CO_2)$ = 0.134 mbar/6.7 mbar = 0.02; inverse triangles represent ratio $p(CO)/p(CO_2)$ = 0.067 mbar/6.7 mbar = 0.01.

In the Fig. 7.2 experimentally measured steady-state polarization curves [29] are compared to simulations results for charge transfer mechanism O1+O2.

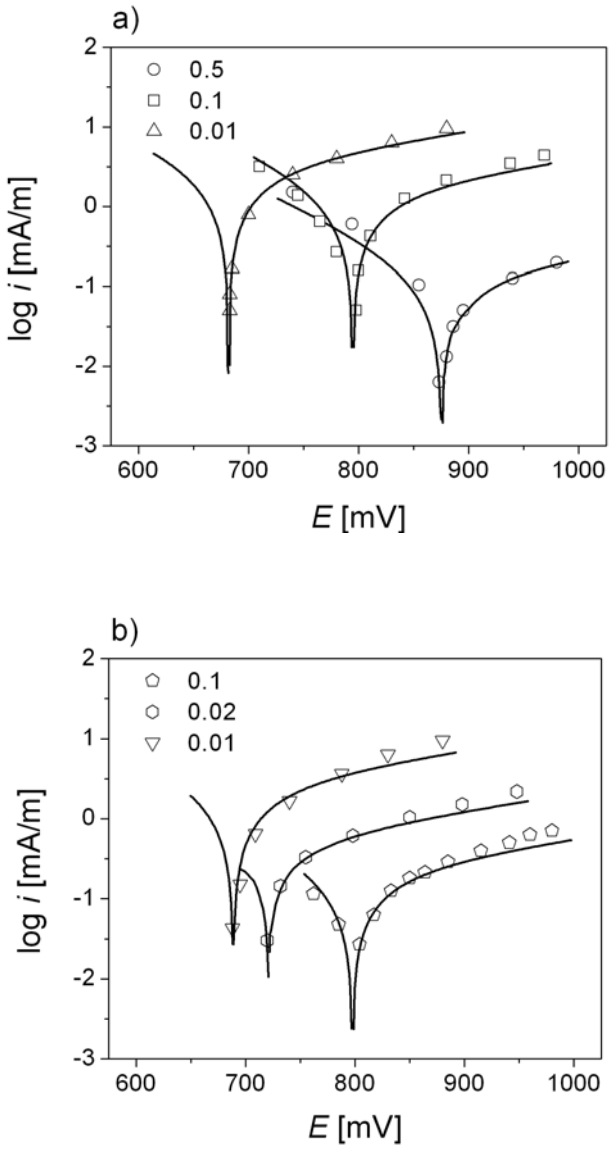

Figure 7.2: Electrochemical steady-state polarization curves. Experiment (open symbols from Ref. [29]) versus simulation with CT reaction mechanism O1+O2 (solid lines). The detailed description is given in the text.

The simulations results for O3+O4 CT mechanism are compared to the experimental data in the Fig. 7.3 a), b).

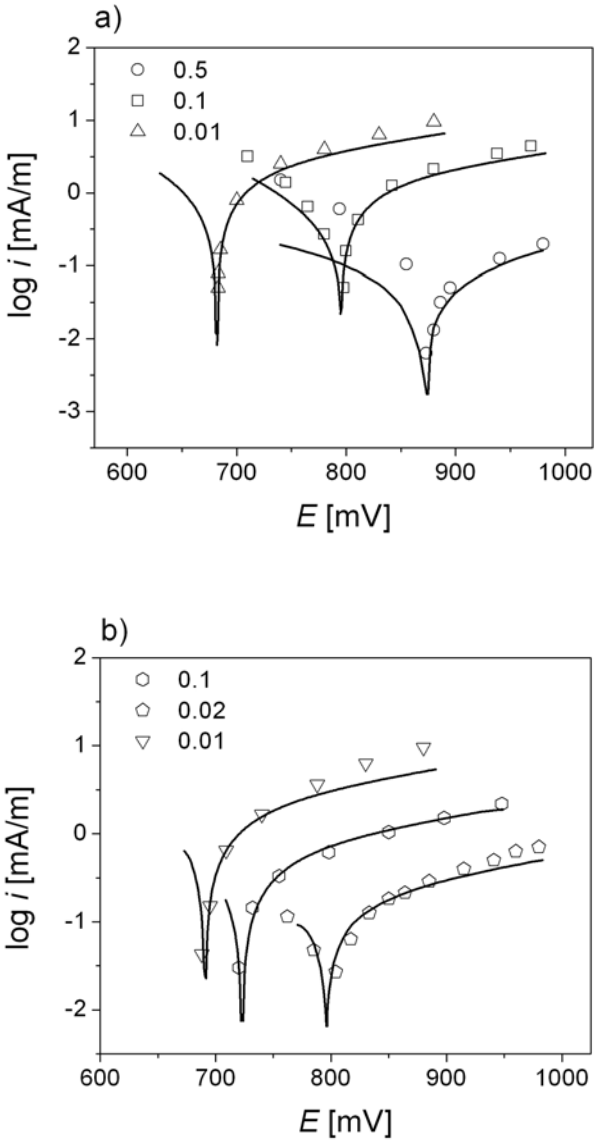

Figure 7.3: Electrochemical steady-state polarization curves. Experiment (open symbols from Ref. [29]) versus simulation with CT reaction mechanism O3+O4 (solid lines). The detailed description is given in the text.

The results for third CT mechanism (O5), which represents a single-step oxygen O^{2-}_{YSZ} spillover reaction, in the course of which two electrons are transferred to the Ni anode simultaneously, are shown in Fig. 7.4.

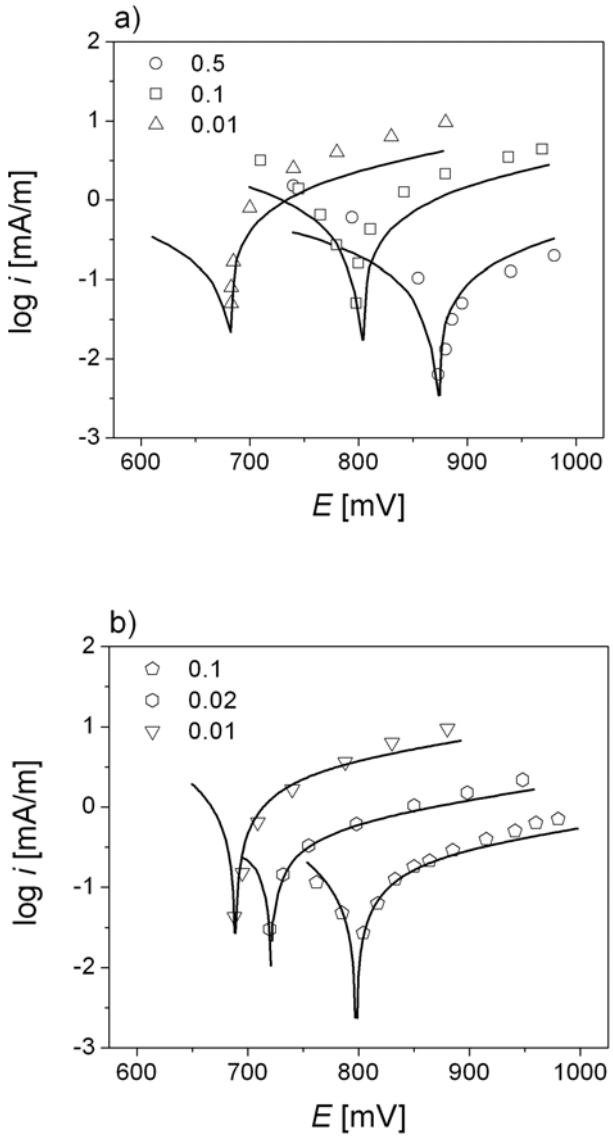

Figure 7.4: Electrochemical steady-state polarization curves. Experiment (open symbols from Ref. [29]) versus simulation with CT reaction O5 (solid lines). The detailed description is given in the text.

A number of observations are pointed out from the results shown in Figures 7.2 – 7.4:

1. All CT mechanisms reasonably reproduce experimental data at low partial pressure of CO and CO_2 (Figs. 7.2 – 7.4 marked by b)).
2. At high partial pressure of CO and CO_2 only CT mechanism O1+O2 describes properly all polarization curves (Figs. 7.2 – 7.4 marked by a)). The deviation from experimental results observed for cathodic branch at $p(CO)/p(CO_2)$ = 333 mbar/670 mbar = 0.5 using CT mechanisms O3+O4 and O5 could by associated with transfer of double ionized oxygen anion to the Ni surface.

For a direct comparison, simulations for the three CT mechanisms are compared for one particular condition in Fig. 7.5. This comparison indicates that best agreement between modeling and experiment is obtained by means of the O1+O2 two-step CT mechanism.

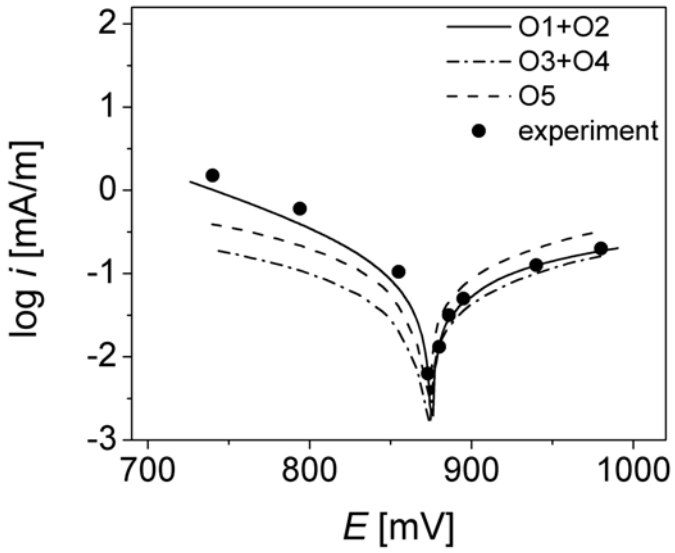

Figure 7.5: Data of Figs. 7.2 – 7.4 represented in a different combination. Simulations of three CT mechanisms are compared to experimental data (filled circles, from Lauvstad et al.[29]) at $p(CO) = 333$ mbar, $p(CO_2) = 670$ mbar, $T = 1149$ K.

Electrochemical impedance spectra

Lauvstad et al. have measured electrochemical impedance spectra for selected experimental conditions[29]. Impedance spectra can give additional information on the physicochemical processes and are, therefore, particularly suited for model validation. Numerical impedance simulations were performed employing the detailed reaction mechanism given in Table II along with the three different CT mechanisms (O1+O2, O3+O4, O5). As in case of the steady-state results, best agreement with experiment was observed for the O1+O2 CT mechanism. Fig. 7.6 shows simulated Nyquist and Bode plots based on this CT mechanism (solid lines) in comparison with experimental data (open symbols). The experimental spectra depicted in Fig. 7.6 a) and b) were measured at an overpotential of 1.7 mV. The spectra of Fig. 7.6 c) and d) were obtained at an overpotential of 75.6 mV. The measurements were performed at partial pressures of $p(CO) = 333$ mbar and $p(CO_2) = 670$ mbar. The characteristics of the experimental impedance spectra (magnitude of resistance, relaxation frequency, depression of semi-circle) are reproduced quantitatively in the simulation. This finding supports the validity of the model and the applied O1+O2 CT mechanism.

The model includes a description of the electrochemical double layer; and the double-layer capacitance is an additional fit parameter. The obtained area-specific double layer capacitance is C = 11.5 F/m^2. We have previously observed values of 3.7 F/m^2 for Ni/YSZ pattern anodes operated on H_2 [117] and 1.5 F/m^2 for Ni/YSZ cermet anodes [124] (all values at T = 1149 K).

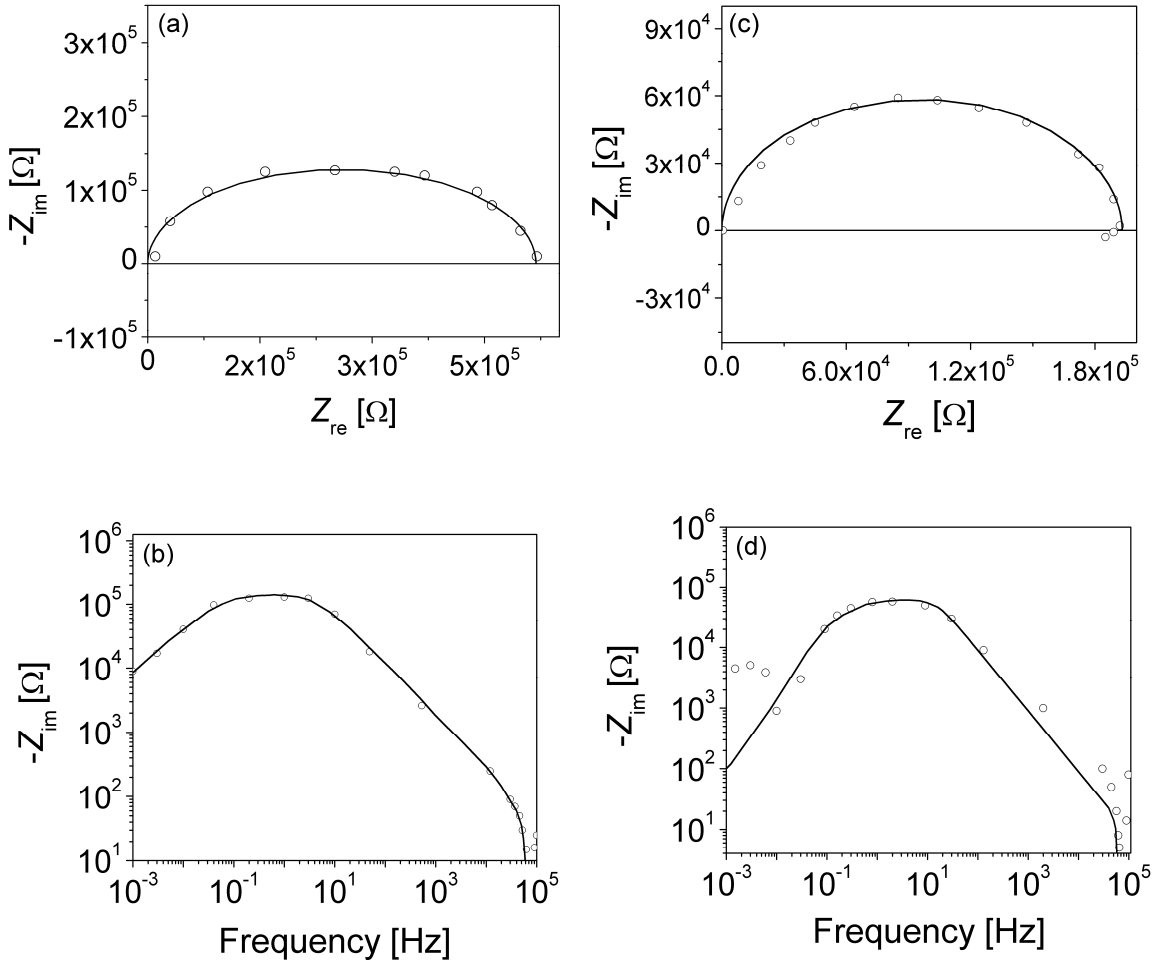

Figure 7.6: Comparison between experimental (open symbols, from Lauvstad et al. [29]) and simulated (solid lines) electrochemical impedance spectra. (a), (b) Spectra obtained at overpotential of 1.7 mV; (c), (d) spectra obtained at overpotential of 75.6 mV. p(CO) = 333 mbar, p(CO_2) = 670 mbar, T = 1149 K.

7.2 Ni, CO-CO_2|YSZ pattern anode

The derived model, for CO electrochemical oxidation in the simplest system, namely Ni/YSZ point electrode, is applied to characterize CO/CO_2 interaction with a more advance model anode, i.e. pattern anodes. In this work, previously published patterned-anode experiments by Utz et al. [33] are used to evaluate CO electrochemical oxidation mechanisms in NiYSZ pattern anodes. Several experimental studies of CO electrochemical oxidation within Ni/YSZ anodes have been

reported [21, 24, 31]. Nevertheless, Utz's paper [33] stands as the most complete data set available. In their work, patterned Ni anodes with an area of 10.25 × 10.25 mm^2 were fabricated on 8.5 mol% polycrystalline Y_2O_3 –stabilized ZrO_2 (YSZ) substrates (Itochu Ceratec Corp., Japan) following the procedure described in [125]. The design of the pattern is composed of an area of 9.25 × 9.25 mm^2 with parallel Ni stripes; in this study stripes with 25 µm width, a spacing of 160 µm and a thickness 800 nm are chosen. The frame with 500 µm width assures contacting of all stripes and this design yields a triple phase boundary length $l_{TPB,th}$ of 1 m. The geometric characteristics of Ni/YSZ pattern anode are summarized in Table 7.3.

Table 7.3: Geometry characteristics of Ni/YSZ pattern anode developed by Utz et al. [33]

Parameter	Symbol	Value
Thickness of electrolyte	d_{elyt}	200 µm
Thickness of nickel	d_{elect}	0.8 µm
Width of free YSZ area	d_{YSZ}	160 µm
Width of Ni stripe	d_{Ni}	25 µm
Length of TPB	l_{TPB}	1.3 m/cm^2
Cell area	A_{cell}	1 cm^2

As the counter electrode, a screen-printed Ni/YSZ cermet anode was used. The preparation of the counter electrode was described by Sonn et al. [126] and was applied to the substrate prior to Ni anode patterning. Electrochemical impedance spectra were recorded in $CO/CO_2/N_2$ gas atmospheres at open circuit over a frequency range of 1 Hz - 1 MHz with a voltage stimulus of 10 mV. The impedance spectra consist of a main process related to the pattern anode electrochemistry and two additional processes due to gas-phase diffusion in the contact mesh and due to the cermet counter electrode. The line-specific resistance (LSR) discussed here was calculated by taking into account the real TPB length (i.e., corrected for an increase in TPB length due to grain growth). In the framework of electrochemical characterization of Ni/YSZ pattern anode two restrictions were considered, for the choice of gas variation range: a) oxidation of Ni at elevated oxygen partial pressure and b) solid carbon formation at high concentration of CO, following the Boudouard reaction. The stability of the Ni patterned anodes was controlled by pre- and post-test SEM analysis.

For modeling the electrochemical measurements, we use the same chemical mechanism as described above (subchapter 7.2, Table 7.1and Table 7.2). However, CT mechanisms employed here, beside already described in Table 7.2 namely O1+O2, an additional O1+O6 was used. This second CT mechanism (O1+O6) predicts a step-by-step discharging of oxygen anion completely on electrolyte surface with electron transferring to Ni. The two CT mechanisms along with kinetics parameters are summarized in Table 7.4.

Table 7.4: Summary of the kinetic parameters for charge-transfer reactions. Ni and YSZ surface site densities are $6.1 \cdot 10^{-9}$ mol/cm^2 and $1.3 \cdot 10^{-9}$ mol/cm^2, respectively. Symmetry factors of the charge-transfer reaction are set to 0.5. The parameters are k^0 pre-exponential factor, E^{act} activation energy. The symbols $\square_{Ni}$ and $\square_{YSZ}$ denote a free surface site on Ni and YSZ, respectively. The units of rate constant follow from the formulation of the rate equations as given in Ref. [117]

Charge-transfer reactions		k^0 (mol/(cm s))	E^{act} (kJ/mol)	Ref.
O1+O2	$O^{2-}_{YSZ} \rightleftharpoons O^{1-}_{YSZ} + e^-_{Ni}$	$8.4 \cdot 10^2$	75	Fit to electrochemical data
	$O^{1-}_{YSZ} + \square_{Ni} \rightleftharpoons O_{Ni} + \square_{YSZ} + e^-_{Ni}$	3.5	135	
O1+O6	$O^{2-}_{YSZ} \rightleftharpoons O^{1-}_{YSZ} + e^-_{Ni}$	$8.4 \cdot 10^2$	75	Fit to electrochemical data
	$O^{1-}_{YSZ} \rightleftharpoons O_{YSZ} + e^-_{Ni}$	$1.4 \cdot 10^{-1}$	82	

The spillover pathways require direct contact of the two surfaces (O1+O2 CT mechanism), but when one of the surfaces is blocked the discharging of oxygen anion can occur only on one surface. In the present study, the later process, discharging of O^{2-}_{YSZ} on YSZ surface, performs in the case when Ni surface is blocked by oxygen atoms, which are produced by CO_2 dissociation reaction via an Eley-Rideal type reaction (reaction 3, Table 7.2). The schematic representation of such a process is shown in Fig. 7.7.

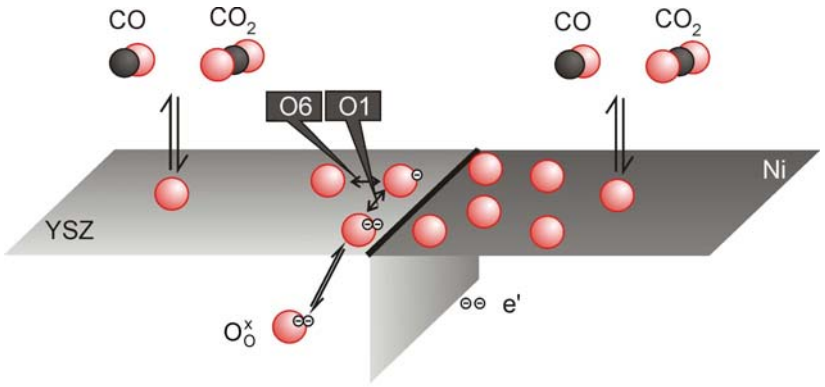

Figure 7.7: Schematic illustration of the reaction mechanism and charge-transfer pathway O1+O6 taking place at the YSZ surface.

The discharged oxygen atom produced in the O1+O6 reaction is reacting with a CO molecule via an ER mechanism. The CT mechanism denoted as O1+O6 takes place at low partial pressure of

CO and high partial pressure of CO_2. Since, at low partial pressure of CO, oxygen, produced as the reaction of CO_2 dissociations is accumulated on Ni surface, and the surface is blocked for direct contact with CO, so that reaction 4 (LH type of CO oxidation, see Table 7.2) becomes impossible. In this case, there is no source to remove oxygen atoms from the Ni surface and CT mechanism O1+O2 is blocked.
Fig. 7.8 shows the comparison of the results of the numerical simulations (solid lines) obtained for the CT reaction O1+O2 with corresponding experimental data (open symbols) for varying CO_2 partial pressure at constant CO partial pressure of $3.9 \cdot 10^4$ Pa.

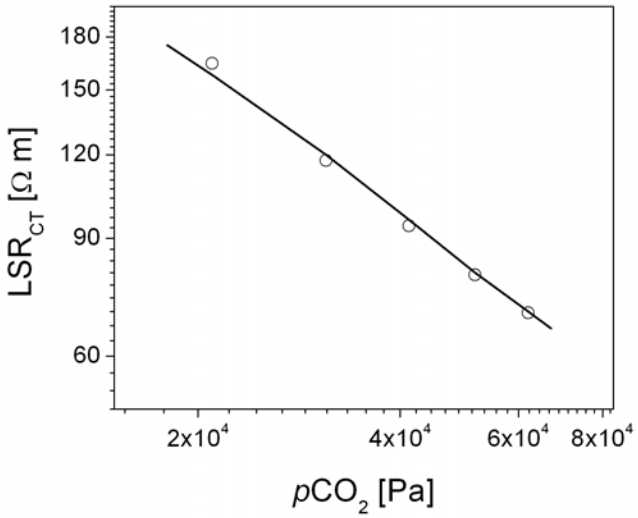

Figure 7.8: Experimental and simulated line-specific resistance (LSR) of a Ni/YSZ pattern anode as a function of CO_2 partial pressure for a CO partial pressure of $3.9 \cdot 10^4$ Pa (1073 K).

Using the same CT reaction (O1+O2) the numerical simulation results of LSR (solid line) for constant pCO = $1 \cdot 10^4$ Pa are compared to the experimentally obtained LSR in Fig. 7.9.

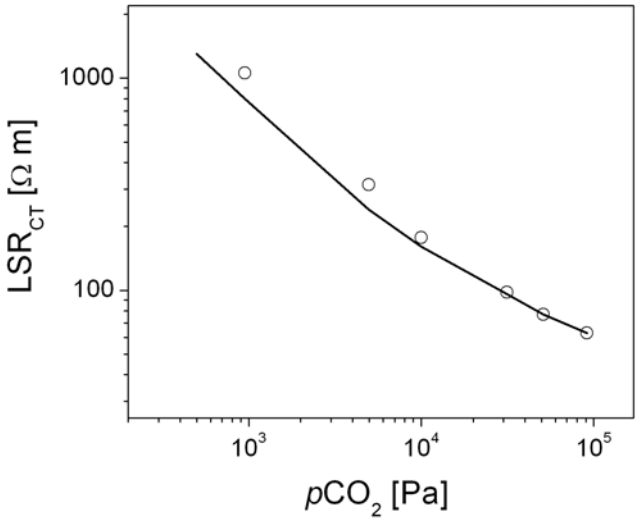

Figure 7.9: Experimental and simulated line-specific resistance (LSR) of a Ni/YSZ pattern anode as a function of CO_2 partial pressure for a CO partial pressure of $1 \cdot 10^4$ Pa (1073 K).

The simulation results shown in Fig. 7.8 and Fig. 7.9 are in very good agreement with experimental measurements. The small deviation at low partial pressure of CO in Fig. 7.9 can be attributed to diffusion of oxygen atoms on YSZ surface.
As can be observed in Fig. 7.10, the experimentally measured LSR changes slope at around 10^4 Pa. This fact along with observation of different activation energies for different gaseous CO/CO2 ratios reported by Utz et al. [33], has been interpreted as changing of CO electrochemical oxidation mechanism. In order to reproduce a positive slope (right part in Fig. 7.10), the CT mechanism O1+O2 was used. The results of these simulations (solid line) are compared to experimental data (open symbols) in Fig. 7.10. In addition, the influence of reaction 3, Table 7.2 (Eley-Rideal mechanism) on simulated curve is shown in this figure as dashed line. As can be observed, using reaction 3 the LSR increases in the region of small CO concentration. In order to reproduce the experimental results shown in the left part of Fig. 7.10, the other CT mechanism, namely O1+O6, was used this will be discussed below.

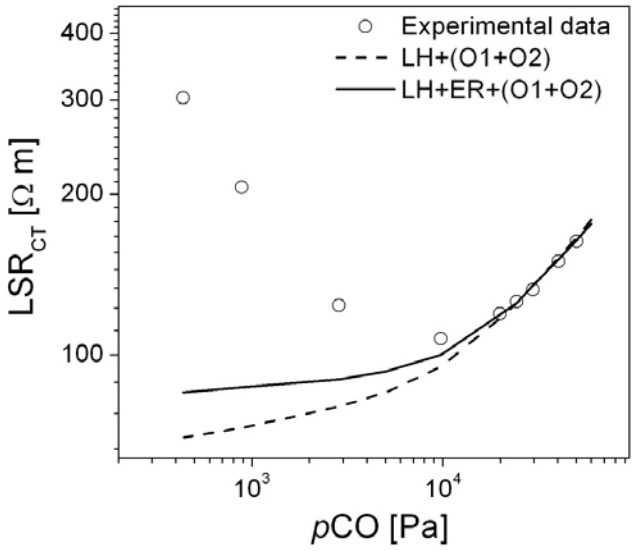

Figure 7.10: Experimental and simulated line-specific resistance (LSR) of a Ni/YSZ pattern anode as a function of CO partial pressure for a CO_2 partial pressure of $2 \cdot 10^4$ Pa (1073 K).

The temperature dependence of LSR was simulated at partial pressures of pCO = $3 \cdot 10^4$ Pa and pCO$_2$ = $2 \cdot 10^4$ Pa and is compared to experimentally measured in Fig. 7.11.

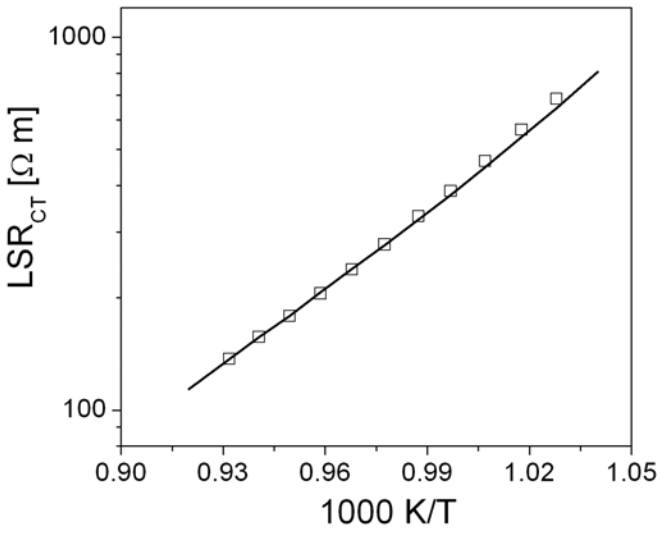

Figure 7.11: Experimental (open squares) and simulated (line) line-specific resistances versus inverse temperature at pCO = $3 \cdot 10^4$ Pa, pCO$_2$ = $2 \cdot 10^4$ Pa.

The magnitude and the slope of simulated curve shown in Fig. 7.11 are in excellent agreement with experimental data, showing the ability of the O1+O2 CT mechanism for high partial pressures of CO and CO_2. The coverages of species during simulations at pCO = $3 \cdot 10^4$ Pa and pCO$_2$ = $2 \cdot 10^4$ Pa, where temperature dependency of LSR was measured, is listed in Table 7.5.

Table 7.5: Coverages of Ni and YSZ surface species at pCO = $3 \cdot 10^4$ Pa and pCO$_2$ = $2 \cdot 10^4$ Pa

Species	Coverage
CO_{Ni}	$2.5 \cdot 10^{-7}$
O_{Ni}	$4.25 \cdot 10^{-3}$
$CO_{2,\,Ni}$	$4.1 \cdot 10^{-3}$
CO_{YSZ}	$3.0 \cdot 10^{-2}$
O_{YSZ}	$1.4 \cdot 10^{-5}$
O^{1-}_{YSZ}	$1.0 \cdot 10^{-2}$
O^{2-}_{YSZ}	0.9

From Table 7.5 it can be concluded that removing of oxygen from the Ni surface is relatively fast which leads to very small oxygen coverage. In order to interpret the experimental results in more details, a sensitivity analysis was performed for all parameters used in the simulation at pCO = $3 \cdot 10^4$ Pa, pCO$_2$ = $2 \cdot 10^4$ Pa. Results are shown in Fig. 7.12.

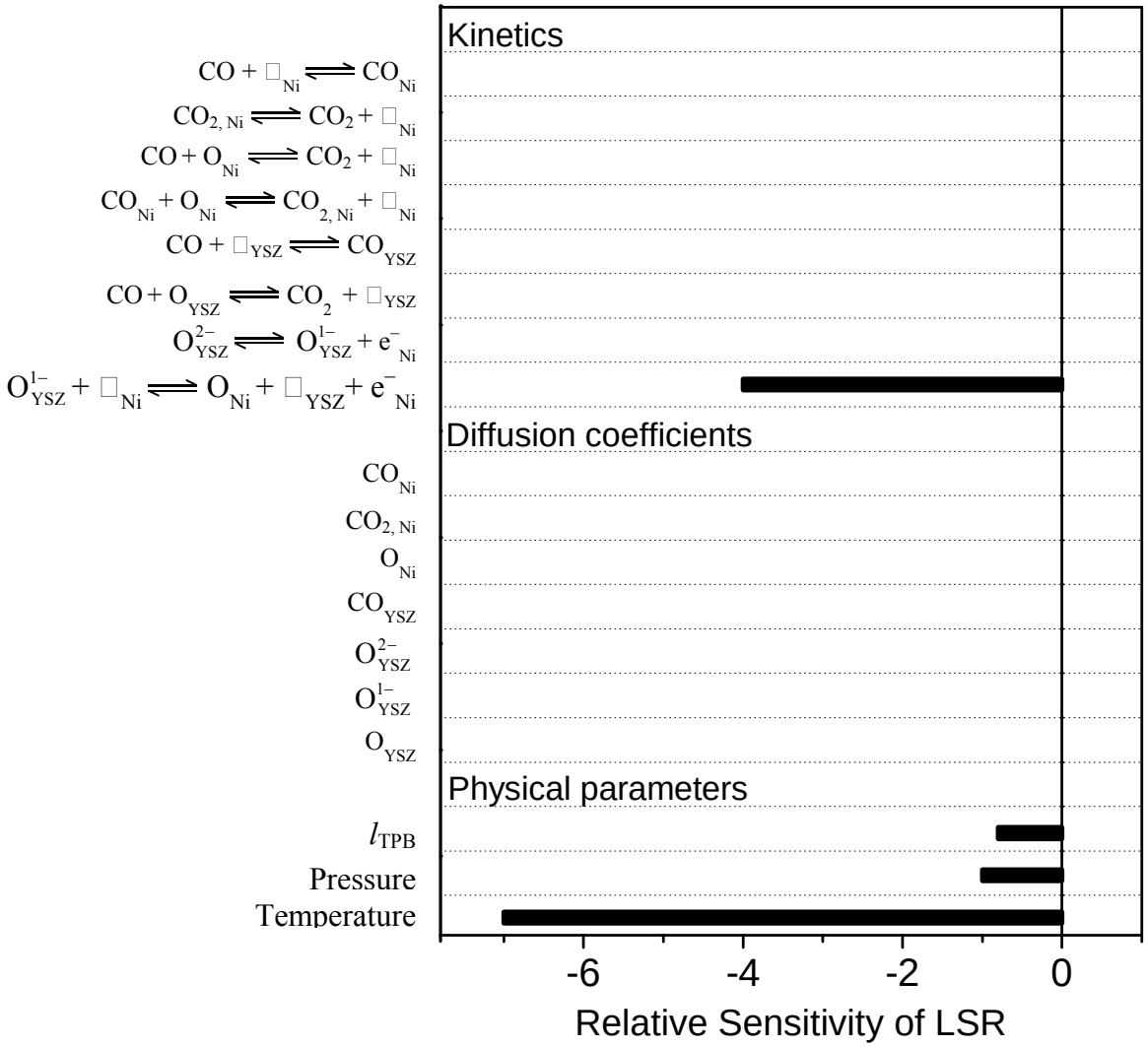

Figure 7.12: Sensitivity of the line specific resistance (LSR) on simulation parameters for temperature of 1073 K and $p\mathrm{CO} = 3 \cdot 10^4$ Pa, $p\mathrm{CO_2} = 2 \cdot 10^4$ Pa. Negative value for sensitivity means that an increase in parameters decreases the LSR.

In the sensitivity analysis, model parameters are individually varied by 10 %, and the impact on the LSR is quantified as dimensionless relative sensitivity. A sensitivity close to zero means that the physical process that is described by the parameter (e.g., diffusion coefficient, rate coefficient) does not influence the LSR and is, therefore, not rate-determining. The data in Fig. 7.12 are separated into kinetic parameters of all reactions (pre-exponential factors), transport parameters of all surface-adsorbed species (diffusion coefficients) and physical parameters (e.g., TPB length, pressure, temperature). In the sensitivity analysis concerning kinetics and diffusion, the only sensitive CT reaction is O2. Fig. 7.12 also shows that the LSR is strongly sensitive on temperature. An increase in absolute pressure also decreases the LSR. The TPB length shows a sensitivity of about –1, that is, increasing TPB length proportionally decreases the LSR, as expected.

As mentioned above, in the region of small CO pressure, LSR vs. CO changes slope to negative value (see Fig. 7.13). In order to reproduce such results, the CT mechanism, O1+O6 was applied. Fig. 7.13 shows the results of the numerical simulations (solid lines) obtained using the CT mechanism O1+O6, in comparison with experimentally measured LSR at constant CO_2 pressure ($2.0 \cdot 10^4$ Pa), varying partial pressure of CO.

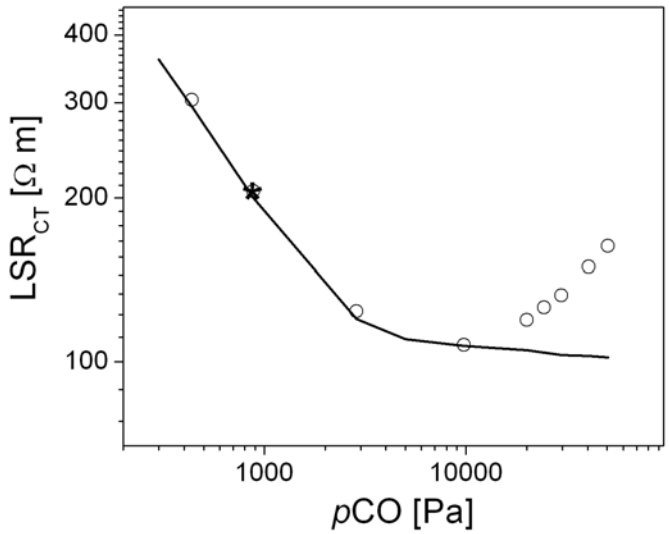

Figure 7.13: Experimental and simulated line-specific resistance (LSR) of a Ni/YSZ pattern anode as a function of CO partial pressure for a CO_2 partial pressure of $2.0 \cdot 10^4$ Pa (1073 K).

Using the same CT mechanism (O1+O6), the simulation results (solid line) for the case of higher CO_2 partial pressure ($5.1 \cdot 10^4$ Pa) are compared to experimental data in Fig. 7.14.

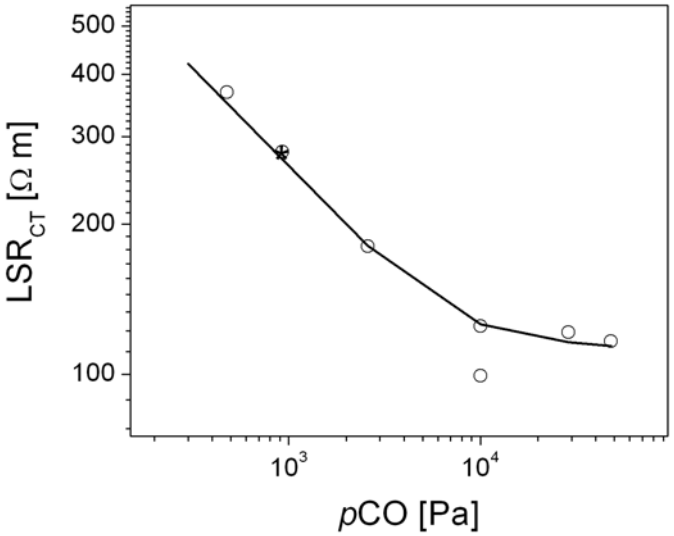

Figure 7.14: Experimental and simulated line-specific resistance (LSR) of a Ni/YSZ pattern anode as a function of CO partial pressure for a CO_2 partial pressure of $5.1 \cdot 10^4$ Pa (1073 K).

The theoretical model reproduces the experimental data well in the all ranges of CO/CO_2 partial pressures.
The temperature dependence of LSR was simulated at partial pressures of $pCO = 9.2 \cdot 10^2$ Pa and $pCO_2 = 2 \cdot 10^4$ Pa and is compared to experimentally measured in Fig. 7.15. The point in which temperature dependency of LSR was measured is shown by an asterisk in Fig. 7.13.

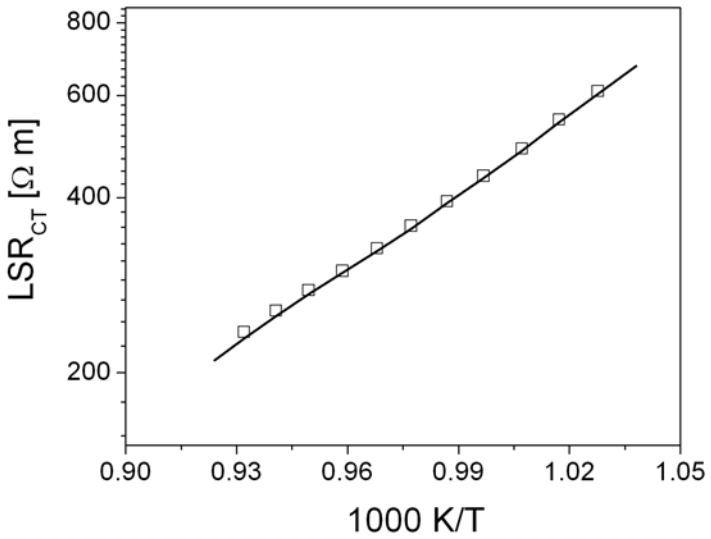

Figure 7.15: Experimental (open squares) and simulated (line) line-specific resistances versus inverse temperature at $pCO = 9.2 \cdot 10^2$ Pa, $pCO_2 = 2 \cdot 10^4$ Pa.

The simulation results in Fig. 7.15 reproduce very good the magnitude and slope of experimentally measured LSR dependency of temperature.
In order to estimate the possibility of blocking CT mechanism O1+O2, the surface species coverages for two different points, marked by an asterisk, in Fig. 7.13 and Fig. 7.14, are listed in Table 7.6, respectively.

Table 7.6: Coverages of Ni and YSZ surface species

Species	Coverage, $pCO = 9.2 \cdot 10^2$ Pa, $pCO_2 = 2 \cdot 10^4$ Pa	Coverage, $pCO = 9.2 \cdot 10^2$ Pa, $pCO_2 = 5.1 \cdot 10^4$ Pa
CO_{Ni}	$7 \cdot 10^{-12}$	$7 \cdot 10^{-12}$
O_{Ni}	0.2	0.45
$CO_{2,\,Ni}$	$3.6 \cdot 10^{-3}$	$8 \cdot 10^{-3}$
CO_{YSZ}	$1.2 \cdot 10^{-3}$	$1.5 \cdot 10^{-3}$
O_{YSZ}	$1.3 \cdot 10^{-2}$	$1.3 \cdot 10^{-2}$
O^{2-}_{YSZ}	0.9	0.9

As can be observed the oxygen coverage increases with increasing of CO_2 partial pressure, which may block the CT mechanism O1+O2.
A sensitivity analysis was performed for all parameters using the CT mechanism O1+O6 at pCO = $9.2 \cdot 10^2$ Pa, pCO$_2$ = $2 \cdot 10^4$ Pa. Results are shown in Fig. 7.16. At low CO partial pressure most sensitive parameters are the same as for high CO partial pressure. However, an additional contribution is appearing for oxygen diffusion on YSZ surface, which is not unexpected because CT mechanism (O1+O6) occurs completely on this surface. Also, it should be noted that the sensitivity of LSR on temperature becomes smaller.

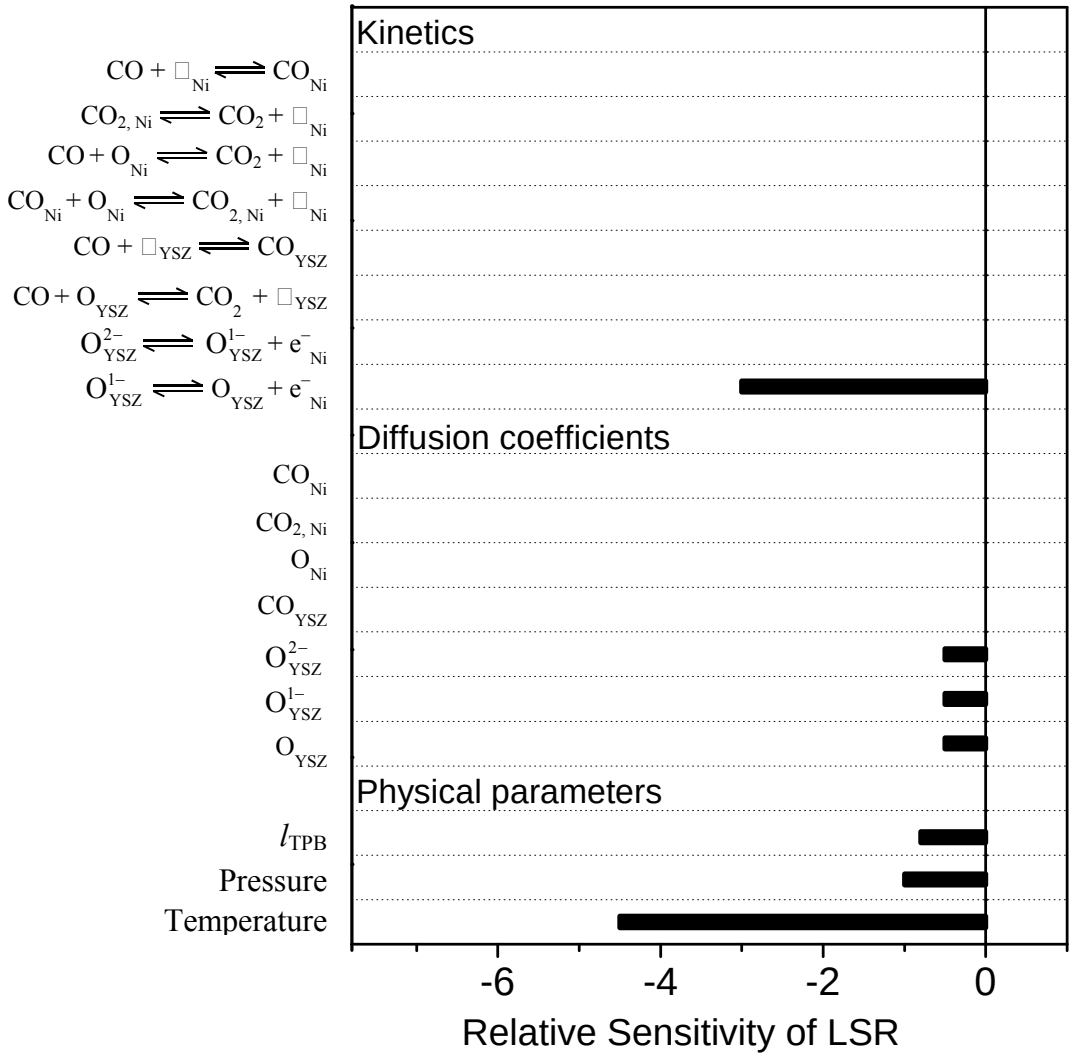

Figure 7.16: Sensitivity of the line specific resistance (LSR) on simulation parameters for temperature of 1073 K and pCO = $9.2 \cdot 10^2$ Pa, pCO$_2$ = $2 \cdot 10^4$ Pa. Negative value for sensitivity means that an increase in parameters decreases the LSR.

7.3 Recommendations for further studies

We have compiled here a complete set of model parameters for the Ni/YSZ system which can be readily used for further studies. However, the surface diffusion coefficients still are order-of-magnitude estimates, especially for the electrolyte surface. Possible degradation processes such as oxidation of Ni and formation of solid carbon were neglected. However, essentially these processes must be included in the model in order to understand in great detail the degradation of Ni/YSZ based SOFCs. Also, in situ analysis of potential impurity segregation and structural integrity should be considered. In this thesis we focused on CO/CO_2 system only, but in general the study should be extended to the more practically used fuel systems such as methane and syngas.

7.4 Conclusions

Carbon monoxide is a fuel for SOFCs, either as single component in laboratory studies, or as component of reformate gases, or after in-situ formation upon hydrocarbon operation. In order to understand the mechanistic details of CO oxidation in Ni/YSZ anodes, we have performed a modeling study elucidated by experiments available from literature.

Using temperature-programmed desorption (TPD) and reaction (TPR) experiments, an elementary kinetic mechanism of CO adsorption, desorption and reaction on the individual Ni and YSZ surfaces was developed and validated. Based on these results, four different charge-transfer mechanisms based on oxygen spillover at the three-phase boundary of Ni, YSZ and gas phase were investigated. Electrochemical simulations of steady-state polarization and impedance behavior were compared to experiments by Lauvstad et al.[28, 29] and Utz et al.[33]. The results show that a two-step oxygen spillover reaction mechanism (denoted as O1+O2 and O1+O6) can consistently reproduce both, the steady-state polarization curves and line specific resistance over a wide range of CO/CO_2 gas compositions.

8. Summary

Solid oxide fuel cell (SOFC) technology is expected to play a major role in future sustainable energy supply. SOFC power plants are expected to have an electrical efficiency of up to 70 %, which would significantly reduce green-house gas emission. Despite all the works that have been done towards understanding the CO electrochemical oxidation on Ni/YSZ anodes, the microscopic details of the electrochemical reaction mechanism, occurring at the TPB, are not yet fully resolved. The investigation of CO oxidation is interesting for because it is a major component of reformate gases and is formed in situ when using hydrocarbons, both of which are relevant fuels in technical SOFC systems. At the same time, reformate gases contain substantial amount of H_2 and H_2O. In such a mixture, it is still unclear whether CO oxidation proceeds directly or indirectly via water-gas shift reaction and H_2 electro-oxidation. In order to elucidate the mechanism and pathways of reformate gas oxidation, it is important to analyze the intrinsic reaction kinetics of CO and H_2 electro-oxidation alone.

In this thesis, a model for the prediction of SOFC performance on the cell level was developed and validated. The model is based on elementary physical and chemical processes without the assumption of a specific rate-determining step. We take into account the heterogeneous chemistry on the nickel and YSZ surfaces, their coupling via the spillover reactions at the three phase boundary, and the surface transport processes on both surfaces. In order to ensure thermodynamic consistency, we derived the forward-rate coefficients only with the corresponding reverse rate constants being calculated employing the available thermo-chemical data. The goal of this work is the identification of rate-limiting processes and the determination of the elementary pathway during charge transfer in Ni/YSZ SOFC anode. In order to achieve our goal, several steps were taken. The first step was to obtain thermodynamically consistent chemical mechanism of CO/CO_2 adsorption/desorption and CO oxidation on electrode (Ni) and electrolyte (YSZ) surfaces. This step was successfully fulfilled by using density functional theory (DFT) calculations and temperature programmed desorption, and reaction (TPD/TPR) experiments along with elementary kinetics simulations of TPD/TPR spectra. In the DFT part, the energetics of fuels (CO and H_2) oxidation was calculated for the YSZ surface. The experimentally proved possibility for a Eley-Rideal type of direct CO oxidation reaction on YSZ, along with the derived kinetics parameters is a new experimental finding, the inclusion of which might also play a more important role if more complex fuel such as reformate gas electro-oxidation is concerned. The next step was, by including results from DFT calculations, TPD/TPR experiments and simulations, to explain the CO oxidation in the simplest SOFC electrochemical system, namely Ni/YSZ point anode. Finally, the last step was comprised with the application of later results in order to explain the electrochemical CO oxidation in more advance pattern Ni/YSZ anodic SOFC system. The last step was successfully achieved that assist to understand the CO electrochemical oxidation in Ni/YSZ anodic SOFC system in great details. As the result, a full kinetic description of the interfacial processes was performed without a priori

assuming a rate-limiting process. The results showed that, indeed, the charge-transfer reaction is one of the rate limiting processes, putting the widely-spread assumption on a firm base.
After performing all of the goals listed above, several tools were developed:

a) A detailed chemical model of CO/CO_2 adsorption/desorption and CO oxidation on Ni and YSZ surfaces were developed. This model is capable to reproduce all data of TPD/TPR experiments.
b) A mechanism of H_2 oxidation over YSZ surface was derived.
c) An electrochemical model of CO oxidation in Ni/YSZ anodes was developed within a physical based modeling framework. The detailed reaction kinetics was applied for the surfaces of electrolyte and electrode resolve the tight coupling of the functional constituents of an SOFC. The generation of electrical current is based on the kinetic description of elementary charge-transfer reactions occurring at the interfaces of electrode and electrolyte.

The main focus of this work was to identify the elementary processes governing SOFC performance on a cell level. Based on the elementary kinetic study on model anodes, the detailed CO electrochemical oxidation mechanism was developed. This thesis provides the answers to important questions that needed resolution before finding the rest of the pieces of SOFC puzzle. These valuable findings will help to develop further ways to improve the efficiency of SOFC use in order to decrease the dependency on non renewable energy resources.

Appendix

A brief introduction to Kröger-Vink Defect Notation

A commonly used notation in the literature for denoting crystal defect chemistry is Kröger-Vink defect notation [11]. In this appendix, a brief introduction to Kröger-Vink notation is provided to aid the reader in interpreting a number of defect chemistry expressions in the main text of this document. Kröger-Vink notation express: a) the vacancies and interstitials as particles which occupy a defined site in a crystal and which may have a charge; b) sites in a crystal are the points where the atoms, the interstitials, or the vacancies can be. For a crystal composed of two kinds of atoms it is assumed "*A*-sites" and the "*B*-sites". An *A*-atom on an *A*-site is denoted by A_A, a vacancy on a *B*-site is a V_B; c) the interstitial atoms on their own place symbol is denoted as A_i or B_i for an *A*-atom or a *B*-atom, respectively; d) an interstitial site not occupied by an interstitial atom then, by definition, is occupied by a vacancy and symbolized as V_i.
In the present thesis Kröger-Vink notation is used to describe chemistry occurs in YSZ and is listed below:

Symbol	Description
Y'_{Zr}	indicates yttrium on the zirconium site with a formal charge of -1
Zr'_{Zr}	indicates the localized electron on a zirconium site
O_O^X	indicates normal oxygen on an oxygen site
$V_O^{\cdot\cdot}$	doubly ionized oxygen vacancy
V	vacancy
e'	free electron
$h^{\cdot}$	free hole
'	be a sign of single negative charge
X	shows that species is not charge
··	be a sign of doubly positive charge

List of Publications

Publications in peer-reviewed journals

1. V. Yurkiv, D. Starukhin, H.-R. Volpp, W. G. Bessler**,** Elementary reaction kinetics of the $CO/CO_2/Ni/YSZ$ electrode, J. Electrochem. Soc., in press
2. A. Gorski, V. Yurkiv, D. Starukhin, H.-R. Volpp, H_2O chemisorption and H_2 oxidation on YSZ: Density Functional Theory and Temperature-Programmed Desorption Studies, J. Power Sources, in press

Conference Proceedings

1. V. Yurkiv, H.-R. Volpp, W. G. Bessler, Heterogeneous chemistry and electrochemistry of carbon monoxide at a Ni/YSZ anode, /Proceedings of the 9th European Solid Oxide Fuel Cell Forum, Lucerne/Switzerland, Chapter 9, pp. 1-14, (2010).
2. A. Gorski, V. Yurkiv, D. Starukhin, H.-R. Volpp, Investigation of H_2O chemisorption and H_2 Oxidation on YSZ: Density Functional Theory Calculations and Temperature-Programmed Desorption Studies, /Proceedings of the 9th European Solid Oxide Fuel Cell Forum, Lucerne/Switzerland, Chapter 15, pp. 85-98, (2010).

Poster Presentations

1. V. Yurkiv, W.G. Bessler, H.-R. Volpp, Elementary kinetics numerical modeling of the Ni, $CO\text{-}CO_2|YSZ$ anodic SOFC system, 109, Bunsentagung, Bielefeld, Germany, p. 363, (2010).
2. W. G. Bessler, F. Leucht, M. Henke, V. Yurkiv, M. Vogler, Multi-scale modeling of solid oxide fuel cells: From patterned anodes to a hybrid power plant system, 109, Bunsentagung, Bielefeld, Germany, p. 234, (2010).
3. Utz A., Weber A., Ivers-Tiffée E., Störmer H., Gerthsen D., Starukhin D., Yurkiv V., Volpp H.-R., Vogler M., Bessler W.G., Mechanisms of the electrooxidation of hydrogen on Ni/YSZ patterned anodes. 108, Bunsentagung, Köln, Germany, p. 50, (2009).
4. Yurkiv V., Vogler M., Starukhin D., Volpp H.-R., Bessler W. G., Modeling study of surface reactions, diffusion and spillover at a Ni/YSZ patterned anode. 108, Bunsentagung, Köln, Germany, p. 359, (2009).
5. Gewies S., Willich C., Yurkiv V., Schiller G., Bessler W.G., Friedrich K.A., Spatially Resolved Electrochemical Performance in a Segmented Planar SOFC, 6th Symposium on Fuel Cell Modelling and Experimental Validation, Bad Herrenalb, Germany, (2009).
6. Yurkiv V., Gomilko V., Starukhin D., Volpp H.-R., Density functional theory investigation of CO adsorption and diffusion on Ni surfaces, 6th Symposium on Fuel Cell Modelling and Experimental Validation, Bad Herrenalb, Germany, (2009).

Bibliography

1. Baur E., Preis H., Über Brennstoff-Ketten mit Festleitern. Z. Elektrochem. , 1937. 43, p. 727-732.
2. Singhal S. C., Kendall K., High-temperature solid oxide fuel cells: Fundamentals, design and applications. Elsevier Science, Oxford, 2003.
3. Minh N. Q., Takahashi T., Science and technology of ceramic fuel cells. Elsevier, Amsterdam, 1995.
4. Kee R. J., Zhu H. Y., Sukeshini A. M., Jackson G. S., Solid oxide fuel cells: Operating principles, current challenges, and the role of syngas. Combustion Science and Technology, 2008. 180(6), p. 1207-1244.
5. Kee R. J., Zhu H. Y., Goodwin D. G., Solid-oxide fue cells with hydrocarbon fuels. Proceedings of the Combustion Institute, 2005. 30, p. 2379-2404.
6. Goodwin D. G., Zhu H. Y., Colclasure A. M., Kee R. J., Modeling Electrochemical Oxidation of Hydrogen on Ni-YSZ Pattern Anodes. J. Electrochem. Soc., 2009. 156(9), p. B1004-B1021.
7. Minh N.Q., Ceramic Fuel-Cells. J. Am. Ceram. Soc., 1993. 76(3), p. 563-588.
8. Ormerod R.M., Solid oxide fuel cells. Chem. Soc. Rev., 2003. 32(1), p. 17-28.
9. Mobius H.H., On the history of solid electrolyte fuel cells. J. Solid State Electrochem., 1997. 1(1), p. 2-16.
10. Cosack T., Kopperger B., Phases in plasma sprayed thermal barrier coatings from yttria partially stabilized zirconia. Materialwissenschaft Und Werkstofftechnik, 2001. 32(8): p. 678-680.
11. Kroger F. A., Vink H. J., Relations between the concentrations of imperfections in crystalline solids. Seitz F, Turnull D (Eds.), Solid State Physics - Advances in Research and Applications, Academic Press, New York, NY, 1956, p. 431-435.
12. Sasaki, K. and Maier J., Re-analysis of defect equilibria and transport parameters in Y_2O_3-stabilized ZrO_2 using EPR and optical relaxation. Solid State Ionics, 2000. 134(3-4), p. 303-321.
13. Hendriks M. G. H. M., ten Elshof J. E., Bouwmeester H. J. M., Verweij H., The defect structure of the double layer in yttria-stabilised zirconia. Solid State Ionics, 2002. 154, p. 467-472.
14. Spacil H.S., Electrical device including nickel-containing stabilized zirconia electrode. US Patent 3,558,360 1970.
15. Blomen L.J.M.J., Mugerwa M. N., Fuel Cell Systems. 1994.
16. Archer D.H., Elikan L., Zaradnik R.L., Hydrocarbon Fuel Cell Technology. B.S. Baker, Editor, Academic Press, New York, 1965, p. 51.
17. Binder H., Köhling A., Krupp H., Richter K., Sandstede G., Elektrochemische Oxidation von Kohlenwasserstoffen in Einer Festelektrolyt-brennstoffzelle bei Temperaturen von 900-1000 ^{0}C. Electrochim. Acta, 1963, 8, p. 781.

18. Karpachev S.V., Filyaev A.T., Pal'guev S.F., Polarization of Carbon MonoxideElectrodes On Platinum in a Solid Zirconia-Lime Electrolyte. Electrochim. Acta, 1964, 9, p. 1681.
19. Möbius H.-H., Rohland B., Method of producing fuel cells with solid electrolytes and ceramic oxide electrode layers, Rev. Energ. Primaire, 1966, 2, p. 27.
20. Etsell T.H., Flengas S.N., Overpotential Behavior of Stabilized Zirconia Solid Electrolyte Fuel Cells. J. Electrochem. Soc., 1971. 118, p. 1890.
21. Holtappels P., De Haart L. G. J., Stimming U., Vinke I. C., Mogensen M., Reaction of CO/CO_2 gas mixtures on Ni-YSZ cermet electrodes. J. Appl. Electrochem., 1999. 29(5), p. 561-568.
22. Mizusaki J., Tagawa H., Miyaki Y., Yamauchi S., Fueki K., Koshiro I., Hirano K., Kinetics of the Electrode-Reaction at the $CO-CO_2$, Porous Pt/Stabilized Zirconia Interface. Solid State Ionics, 1992. 53-6, p. 126-134.
23. Eguchi K., Setoguchi T., Okamoto K., Arai H., An Investigation of Anode Material and Anodic Reaction for Solid Oxide Fuel Cell. ECS Transactions,, 1993. 93-4, p. 494.
24. Aaberg R. J., Tunold R., Tjelle S., Odegard R., Oxidation of CO and H_2 on Ni / YSZ Cermet Electrodes. Proc. 17th Risoe International Symposium on Materials Science: High Temperature Electrochemistry: Ceramics and Metals, 1996, p. 511.
25. Matsuzaki Y., Yasuda I., Electrochemical oxidation of H-2 and CO in a $H_2-H_2O-CO-CO_2$ system at the interface of a Ni-YSZ cermet electrode and YSZ electrolyte. J. Electrochem. Soc., 2000. 147(5), p. 1630-1635.
26. Boulenouar F.Z., Yashiro K., Oishi M., Kaimai A., Nigara Y., Kawada T., Mizusaki J., Electrochemical Oxidation of CO in a $CO-CO_2$ System at the Interface of Ni Grid Electrode/YSZ Electrolyte. Electrochem. Soc. Series, 2001, p. 759.
27. Weber A., Sauer B., Muller A. C., Herbstritt, D., Ivers-Tiffee, E., Oxidation of H_2, CO and methane in SOFCs with Ni/YSZ-cermet anodes. Solid State Ionics, 2002. 152, p. 543-550.
28. Lauvstad, G.O., Tunold R., Sunde S., Electrochemical oxidation of CO on Pt and Ni point electrodes in contact with an yttria-stabilized zirconia electrolyte - I. Modeling of steady-state and impedance behavior. J. Electrochem. Soc., 2002. 149(12), p. E497-E505.
29. Lauvstad, G.O., Tunold R., Sunde S., Electrochemical oxidation of CO on Pt and Ni point electrodes in contact with an yttria-stabilized zirconia electrolyte - II. Steady-state and impedance measurements. J. Electrochem. Soc., 2002. 149(12), p. E506-E514.
30. Costa-Nunes O., Gorte R. J., Vohs J. M., Comparison of the performance of $Cu-CeO_2$-YSZ and Ni-YSZ composite SOFC anodes with H_2, CO, and syngas. J. Power Sources, 2005. 141(2), p. 241-249.
31. Sukeshini A.M., Habibzadeh B., Becker B. P., Stoltz C. A., Eichhorn B. W., Jackson G. S., Electrochemical oxidation of H_2, CO, and CO/H_2 mixtures on patterned Ni anodes on YSZ electrolytes. J. Electrochem. Soc., 2006. 153(4), p. A705-A715.
32. Leonide A., Hansmann S., Ivers-Tiffee E., Performance Simulation of C/V-characteristics for ASC by means of detailed impedance analysis. The 9th European Solid Oxide Fuel Cell Forum, Lucerne, Switzerland (2010), 2010, p. 6-1 - 6-7.

33. Utz A., Leonide A., Weber A., Ivers-Tiffee E., Studying the CO/CO_2 characteristics of SOFC anodes by means of Ni patterned anodes. The 9th European Solid Oxide Fuel Cell Forum, Lucerne, Switzerland (2010), 2010, p. 9-5 - 9-70.
34. Einstein A., Über die spezielle und allgemeine Relativitätstheorie. Springer, Berlin, 2001.
35. Schrödinger E., Planck M., Einstein A., Lorentz H. A., Briefe zur Wellenmechanik. Springer, Berlin, 1963.
36. Born M. Oppenheimer J. R., Zur Quantentheorie der Molekeln. Annalen der Physik, 1927. 84(457-484).
37. Segall M.D., Lindan P. J. D., Probert M. J., Pickard C. J., Hasnip P. J., Clark, S. J., Payne M. C., First-principles simulation: ideas, illustrations and the CASTEP code. J. Phys.-Condensed Matter, 2002. 14(11), p. 2717-2744.
38. Hohenberg P., Kohn W., Inhomogeneous electron gas. Phys. Rev., 1964. 136, p. 864–871.
39. Kohn W., Sham L. J., Self-consitent equations including exchange and correlation effects. Phys. Rev., 1965. 140, p. 1133-1139.
40. Lundqvist S., March N. H., Theory of the inhomogenous electron gas. Plenum Press, New York, 1983.
41. Perdew J. P., Chevary J. A., Vosko S. H., Jackson K. A., Pederson M. R., Singh D. J., Fiolhais C., Atoms, Molecules, Solids, and Surfaces - Applications of the Generalized Gradient Approximation for Exchange and Correlation. Phys, Rev, B, 1992. 46(11), p. 6671-6687.
42. Parr R., Yang W., Density-functional theory of atoms and molecules. Oxford, 1989.
43. Harle H., Mendel K., Metka U., Volpp H.-R., Willms L., Wolfrum J., Temperature dependence (90-440 K) of the vibrational spectra of CO adsorbed on platinum(111) studied by sum-frequency generation. Chem. Phys. Let., 1997. 279(5-6), p. 275-281.
44. Metka U., Untersuchung von Teilschritten der heterogenen Reaktion von CO mit NO an Platin mittels der Summenfrequenz-Spektroskopie. PhD Thesis, Heidelberg University, Heidelberg, Germany, 2000.
45. Adamson A. W., Gast A. P., Physical Chemistry of Surface. Wiley, New York, 1997.
46. Shen Y. R., The principles of Nonlinear optics. Wiley, New York, 1984.
47. Klunker C., Balden M., Lehwald S., Daum W., CO stretching vibrations on Pt(111) and Pt(110) studied by sum-frequency generation. Surface Science, 1996. 360(1-3), p. 104-111.
48. Miragliotta J., Polizotti R. S., Rabinowitz P., Cameron S. D., Hall R. B., Infrared-Visible Sum-Frequency Generation Spectra of Co on Ni(100). Applied Phys. Materials Science & Processing, 1990. 51(3), p. 221-225.
49. Superfine R., Guyotsionnest P., Hunt J. H., Kao C. T., Shen Y. R., Surface Vibrational Spectroscopy of Molecular Adsorbates on Metals and Semiconductors by Infrared Visible Sum-Frequency Generation. Surface Science, 1988. 200(1), p. L445-L450.
50. Harris A.L., Chidsey C. E. D., Levinos N. J., Loiacono D. N., Monolayer Vibrational Spectroscopy by Infrared-Visible Sum Generation at Metal and Semiconductor Surfaces. Chem. Phys. Let., 1987. 141(4), p. 350-356.

51. Apker L., Surface Phenomena Useful in Vacuum Technique, Ind. Eng. Chem., 1948. 40, p. 846.
52. Ehrlich G., Modern Methods in Surface Kinetics: Flash Desorption, Field Emission Microscopy, and Ultrahigh Vacuum Techniques, Advanced Catalysis, 1963. 14, p. 256-242.
53. Redhead P. A., Hobson J. P., Kornelsen E. V., The physical Basis of Ultrahigh Vacuum. Chapman and Hall, London, 1968.
54. Christmann K., Schober O., Ertl G., Adsorption of CO on a Ni(111) Surface. J. Chem. Phys., 1973. 60(12), p. 4719-4724.
55. Ertl G., Neumann M., Streit K. M., Chemisorption of CO on the Pt(111) Surface. Surface Science, 1977. 64: p. 393-410.
56. Chan C. M., Aris R., Weinberg W. H., Appl. Surf. Sci., 1978. 1, p. 360.
57. Habenschaden E. Küppers J., Evaluation of Flash Desorption Spectra, Surf. Sci. Let., 1984. 138, p. L147-L150.
58. Falconer J. L., Schwarz J. A., Temperature-Programmed Desorption and Reaction: Applications to Supported Catalysts, Cat. Rev. Sci. Eng., 1983. 25(2), p. 141.
59. King D. A., Thermal Desorption from Metal Surfaces: A Review. Surface Science, 1975. 47, p. 384-402.
60. Dejong A. M., Niemantsverdriet, J. W., Thermal-Desorption Analysis - Comparative Test of 10 Commonly Applied Procedures. Surface Science, 1990. 233(3), p. 355-365.
61. Vielstich W., Lamm A., Gasteiger H. A, Handbook of Fuel Cells. John Wiley & Sons, Inc., Chichester, 2003.
62. Bagotsky V. S., Fundamentals of Electrochemistry, second edition. Wiley-Interscience, 2006.
63. Bockris J. O., Amulya K., Reddy N., Gamboa-Aldeco M., Modern Electrochemistry - Fundamentals of Electrodics, Publishers, 2000. Volume 2A. Kluwer Academic/Plenum Publishers, 2000.
64. Atkins P., de Paula J., Physical Chemistry, Seventh Edition. W.H, Freeman and Company, New York, 2003.
65. Adler S. B., Bessler W. G., Elementary kinetic modeling of solid oxide fuel cell electrode reactions. in Handbook of Fuel Cells - Fundamentals, Technology and Applications. John Wiley and Sons, 2009.
66. Walters K.M., Dean A. M., Zhu H. Y., Kee R. J., Homogeneous kinetics and equilibrium predictions of coking propensity in the anode channels of direct oxidation solid-oxide fuel cells using dry natural gas. J. Power Sources, 2003. 123(2), p. 182-189.
67. Sheng, C.Y., Dean A.M., Importance of gas-phase kinetics within the anode channel of a solid-oxide fuel cell. J. Phys. Chem. A, 2004. 108(17), p. 3772-3783.
68. Atkinson A., Barnett S., Gorte R. J., Irvine J. T. S., Mcevoy A. J., Mogensen M., Singhal S. C., Vohs J., Advanced anodes for high-temperature fuel cells. Nature Materials, 2004. 3(1), p. 17-27.
69. Deutschmann O., Tischer S., Correa C., Chatterjee D., Kleditzsch S., Janardhanan V., DETCHEM Software Package, Version 2.0, http://www.detchem.com,. 2007.

70. Kee R. J., Coltrin M. E., Glarborg P., Chemically reacting flow. Theory and practice. (John Wiley & Sons). 2003.
71. Behrendt F., Deutschmann O., Ruf B., Schmidt R., Warnatz J., Simulation of Heterogeneous Reaction Systems. in Gas phase chemical reaction systems: experiment and models, 100 years after Max Bodenstein, J. Wolfrum, et al., Editors (Springer), 265-278, 1996.
72. Butler, J. A. V., Trans. faraday Soc., 1924. **19**: p. 729.
73. Bowden F. P., Rideal E. K., The Electrolytic Behaviour of Thin Films. Part I.-Hydrogen. Proc. Royal Society of London. Series A, Containing Papers of a Mathematical and Physical Character, Volume 120, Issue 784, pp. 59-79.
74. Bockris J. O., Nagy Z., Symmetry Factor and Transfer Coefficient. J. Chem. Educ., 1973. 50(12), p. 839-843.
75. Goodwin, D. G., A Patterned Anode Model with Detailed Chemistry, in Solid Oxide Fuel Cells IX, S. Singhal and J. Mizusaki, Editors, The Electrochemical Society Proceedings Series, Pennington, NJ, 2005. PV 2005-07, p. 699-707.
76. Zhu H. Y., Kee R. J., Janardhanan V. M., Deutschmann O., Goodwin D. G., Modeling elementary heterogeneous chemistry and electrochemistry in solid-oxide fuel cells. J. Electrochem. Soc., 2005. 152(12), p. A2427-A2440.
77. Bessler W. G., Gewies S., Vogler M., A new framework for physically based modeling of solid oxide fuel cells. Electrochim. Acta, 2007. 53(4), p. 1782-1800.
78. Marcus R. A., On the Theory of Oxidation-Reduction Reactions Involving Electron Transfer, J. Chem. Phys., 1956. 24, p. 966.
79. Marcus R. A., On the Theory of Electron-Transfer Reactions. VI. Unified Treatment for Homogeneous and Electrode Reactions, J. Chem. Phys., 1965. 43, p. 679.
80. Marcus R. A., Electron transfer at electrodes and in solution: Comparison of theory and experiment, Electrochim. Acta, 1968. 13, p. 995.
81. Bonnateree R., Gauquis G., L'equation de la courbe voltamperometrique en termes de la theorie de Marcus—application a lètude theorique de la variation du coefficient de transfert avec le potentiel, J. Electroanal. Chem., 1972. 35, p. 287.
82. Saveant J. M., Tesier D., Convolution potential sweep voltammetry V. Determination of charge transfer kinetics deviating from the Butler-Volmer behaviour, J. Electroanal. Chem., 1975. 65, p. 57-66.

83. Weaver M. J., Anson F. C., Potential dependence of the electrochemical transfer coefficient. Further studies of the reduction of chromium(III) at mercury electrodes, J. Phys. Chem., 1976. 80, p. 1861–1866.
84. Samec Z, Weber J., The effect of the double layer on the rate of the Fe^{3+}/Fe^{2+} reaction on a platinum electrode and the contemporary electron transfer theory, J. Electroanal. Chem., 1977. 77, p. 163-180.
85. Petersen R. A, Evans D. H., Heterogeneous electron transfer kinetics for a variety of organic electrode reactions at the mercury-acetonitrile interface using either tetraethylammonium perchlorate or tetraheptylammonium perchlorate electrolyte, J. Electroanal. Chem., 1987. 222, p. 129.
86. Bond A. M., Mahon P. J., Maxwell E. A., Oldham K. B., Zoski, C. G., A Statistical Study of the Potential Dependence of a Transfer-Coefficient Supports the Marcus Theory. J. Electroanal. Chem., 1994. 370(1-2), p. 1-15.
87. Benderskii V. A., Benderskii A. V., Laser electrochemistry of intermediates. CRC Press, 1995.
88. Bessler, W. G., Electrochemistry and Transport in Solid Oxide Fuel Cells. Habilitation, Heidelberg University, Heidelberg, Germany, 2007.
89. Vogler M., Elementary kinetic modelling applied to solid oxide fuel cell pattern anodes and a direct flame fuel cell system. PhD Thesis, Heidelberg University, Heidelberg, Germany, 2009.
90. Bessler W. G., et al., Model Anodes and Anode Models for understanding the Mechanism of Hydrogen Oxidation in Solid Oxide Fuel Cell. Phys. Chem. Chem. Phys., 12, 13888 (2010).
91. Deuflhard P., Hairer E., Zugck J., One-Step and Extrapolation Methods for Differential-Algebraic Systems. Numerische Mathematik, 1987. 51(5), p. 501-516.
92. Vanderbilt D., Soft Self-Consistent Pseudopotentials in a Generalized Eigenvalue Formalism. Phys. Rev. B, 1990. 41(11), p. 7892-7895.
93. Monkhorst H. J., Pack J. D, Special points for Brillouin-zone integrations. Phys. Rev. B, 1976. 13, p. 5188-5192.
94. Govind N., Petersen M., Fitzgerald G., King-Smith D., Andzelm J., A generalized synchronous transit method for transition state location. Computational Materials Science, 2003. 28(2), p. 250-258.
95. Shishkin M., Ziegler T., The Oxidation of H_2 and CH_4 on an Oxygen-Enriched Yttria-Stabilized Zirconia Surface: A Theoretical Study Based on Density Functional Theory. J. Phys. Chem. C, 2008. 112(49), p. 19662-19669.
96. Stapper G., Bernasconi M., Nicoloso N., Parrinello M., Ab initio study of structural and electronic properties of yttria-stabilized cubic zirconia. Phys. Rev. B, 1999. 59(2), p. 797-810.
97. Xia X., Oldman R, Catlow R., Computational Modeling Study of Bulk and Surface of Yttria-Stabilized Cubic Zirconia. Chem. Materials, 2009. 21(15), p. 3576-3585.

98. Davis R., Woodruff D. P., Hofmann P., Schaff O., Fernandez V., Schindler K. M., Fritzsche V., Bradshaw A. M., Local structure determination for low-coverage CO on Ni(111). J. Phys.-Condensed Matter, 1996. 8(10), p. 1367-1379.
99. Kevan S. D., Davis R. F., Rosenblatt D. H., Tobin J. G., Mason M. G., Shirley D. A., Structural Determination of Molecular Overlayer System with Normal Photoelectron Diffraction: c(2x2) CO-NO(001) and (3x3) R30^0 CO-Ni(111). Phys. Rev. Lett., 1981. 46, p. 1629.
100. Held G., Schuler J., Sklarek V., Steinruck H. P., Determination of adsorption sites of pure and coadsorbed CO on Ni(111) by high resolution X-ray photoelectron spectroscopy. Surface Science, 1998. 398(1-2), p. 154-171.
101. Davila M. E., Asensio M. C., Woodruff D. P., Schindler K. M., Hofmann P., Weiss K. U., Dippel R., Gardner P., Fritzsche V., Bradshaw A. M., Conesa J. C., Gonzalezelipe A. R., Structure Determination of Ni(111)C(4x2)-CO and Its Implications for the Interpretation of Vibrational Spectroscopic Data. Surface Science, 1994. 311(3), p. 337-348.
102. Sprunger P. T., Besenbacher F., Stensgaard I., STM Investigation of the Ni(111)-CO(4x2) Structure. Chem. Phys. Let., 1995. 243(5-6), p. 439-444.
103. Becker L., Aminpirooz S., Hillert B., Pedio M., Haase J., Adams D. L., Threefold-Coordinated Hollow Adsorption Site for Ni(111)-CO(4x2) - a Surface-Extended X-Ray-Absorption Fine-Structure Study. Phys. Rev. B, 1993. 47(15), p. 9710-9714.
104. Mapledoram L. D., Bessent M. P., Wander A., King D. A., An Automated Tensor Leed Analysis of the Ni(111)-CO(4x2) Structure. Chem. Phys. Let., 1994. 228(6), p. 527-532.
105. Edmonds T, Pitkethly R.C., The Adsorption of Carbon Monoxide and Carbon Dioxide at the (111) Face of Nickel observed by LEED. Surface Science, 1969. 15, p. 137-163.
106. Christmann K., Schober O, Ertl G., Adsorption of CO on a Ni(111) surface. J. Chem. Phys., 1974. Vol. 60(12), p. 4719-4724.
107. Janardhanan V. M, Deutschmann O., CFD analysis of a solid oxide fuel cell with internal reforming: Coupled interactions of transport, heterogeneous catalysis and electrochemical processes. J. Power Sources, 2006. 162, p. 1192-1202.
108. Stuckless J. T., Alsarraf N., Wartnaby C., King D. A., Calorimetric Heats of Adsorption for Co on Nickel Single-Crystal Surfaces. J. Chem. Phys., 1993. 99(3), p. 2202-2212.
109. Eichler A., CO adsorption on Ni(111) - a density functional theory study. Surface Science, 2003. 526(3), p. 332-340.
110. Ertl G., Neumann M., Streit K. M., Chemisorption of CO on the Pt(111) Surface. Surface Science, 1977. 64: p. 393-410.
111. Mangan M. A., Lindsay B. G., Stebbings R. F., Absolute partial cross sections for electron-impact ionization of CO from threshold to 1000 eV. J. Phys. B-Atomic Molecular and Optical Physics, 2000. 33(17), p. 3225-3234.
112. Straub H. C., Lindsay B. G., Smith, K. A., Stebbings, R. F., Absolute partial cross sections for electron-impact ionization of H_2O and D_2O from threshold to 1000 eV. J. Chem. Phys., 1998. 108(1), p. 109-116.

113. Wagner C., Die Löslichkeit von Wassedampf in ZrO_2-Y_2O_3-Mischkristallen. Berichte der Bunsengesellschaft, 1968. 72, (7), p. 778-781.
114. Atkinson A., Barnett S., Gorte R. J., Irvine J. T. S., Mcevoy A. J., Mogensen M., Singhal S. C., Vohs J., Advanced anodes for high-temperature fuel cells. Nature Materials, 2004. 3(1), p. 17-27.
115. Adler S. B., Bessler W. G., Elementary kinetic modeling of solid oxide fuel cell electrode reactions. in Handbook of Fuel Cells - Fundamentals, Technology and Applications. John Wiley and Sons, 2009.
116. Chase M. W., Davies C. A., Downey J. R., Frurip D. J., McDonald R. A., Syverud A. N., Thermochemical Tables Third Edition. J. Phys. Chem. Ref., 1985. 14, p. 35-50.
117. Vogler M., Bieberle-Hutter A., Gauckler L., Warnatz J., Bessler W. G., Modelling Study of Surface Reactions, Diffusion, and Spillover at a Ni/YSZ Patterned Anode, J. Electrochem. Soc.. 2009, p. B663-B672.
118. Bessler W.G., Warnatz J., Goodwin D. G., The influence of equilibrium potential on the hydrogen oxidation kinetics of SOFC anodes. Solid State Ionics, 2007. 177(39-40), p. 3371-3383.
119. Manning, P.S., Sirman J. D., DeSouza R. A., Kilner J. A., The kinetics of oxygen transport in 9.5 mol % single crystal yttria stabilised zirconia. Solid State Ionics, 1997. 100(1-2), p. 1-10.
120. Etsell T.H., Flengas S.N., Overpotential Behavior of Stabilized Zirconia Solid Electrolyte Fuel Cells. J. Electrochem. Soc., 1971. 118, p. 1890.
121. Zhu X. D., Rasing T., Shen Y. R., Surface-Diffusion of CO on Ni(111) Studied by Diffraction of Optical Second-Harmonic Generation Off a Monolayer Grating. Phys. Rev. Let., 1988. 61(25), p. 2883-2885.
122. Inderwildi O.R., Lebiedz D., Deutschmann O., Warnatz J., Coverage dependence of oxygen decomposition and surface diffusion on rhodium (111): A DFT study. J. Chem. Phys., 2005. 122(3), p. 34710.
123. Galdikas A., Descorme C., Duprez D., Surface diffusion upon oxygen isotopic exchange on oxide-supported metal nanoclusters. Solid State Ionics, 2004. 166(1-2), p. 147-155.
124. Gewies S., Bessler W. G., Physically based impedance modeling of Ni/YSZ cermet anodes. J. Electrochem. Soc., 2008. 155, p. B937-B952.
125. Utz A., Stormer H., Leonide A., Weber A.,Ivers-Tiffee E., Degradation and relaxation effects of Ni patterned anodes in H_2/H_2O atmosphere. J. Electrochem. Soc., 2010. 157, p. B920-B930.
126. Sonn V., Leonide A., Ivers-Tiffee E., Towards Understanding the Impedance Response of Ni/YSZ Anodes. ECS Trans., 2007. 7(1), p. 1363.

Eidesstattliche Erklärung

Ich erkläre hiermit eidessattlich, dass ich

1. diese Arbeit ohne fremde Hilfe angefertigt habe,

2. die Verwendung von Gedanken und Forschungsergebnissen Dritter innerhalb dieser Arbeit gekennzeichnet habe.

Heidelberg, den 4. November 2010

Vitaliy Yurkiv